國立交通大學

物理研究所

博士論文

在一簡單流體內瞬間正則模之局域至非局域轉變

Localization-Delocalization Transition of the Instantaneous Normal Modes in a Simple Fluid

研究生 ：黃邦杰
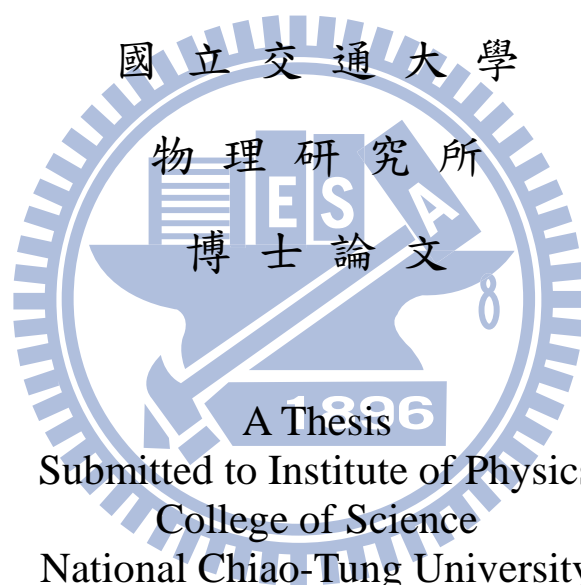
指導教授: 吳天鳴 教授

中華民國九十九年六月

在一簡單流體內瞬間正則模之局域至非局域轉變

Localization-Delocalization Transition of the Instantaneous Normal Modes in a Simple Fluid

研 究 生 ： 黃邦杰　　　　　Student : Ban-Chiech Huang

指導教授 ： 吳天鳴 教授　　　Adviser : Ten-Ming Wu

國 立 交 通 大 學

物 理 研 究 所

博 士 論 文

A Thesis
Submitted to Institute of Physics
College of Science
National Chiao-Tung University
in Partial Fulfillment of the Requirements
for the Degree of
Doctor of Philosophy
In

Physics

June 2010

Hsinchu, Taiwan

中華民國九十九年六月

在一簡單流體內瞬間正則模之局域至非局域轉變

學生:黃邦杰　　　　　　　　　指導教授: 吳天鳴

國立交通大學物理研究所

摘　　要

在本文中，我們探討在一簡單短距交互作用流體內瞬間正則模之局域至非局域轉變。此液體模型提供拓樸性無序系統的原形。在瞬間正則模頻譜中，分別在正數與負數瞬間正則模頻譜上發現轉變點。我們使用有限尺度標度法定出轉變點，並且計算關聯長度的臨界指數。在數值誤差範圍內，所估計的臨界指數與安德森模型是一致的。此結果驗證了三維的安德森模型與拓樸性無序系統的短距簡單流體屬於同樣的統計普適性分類。

我們也對瞬間正則模做了多重碎形的分析。在局域與非局域轉變的轉變點附近，瞬間正則模表現出多重碎形的特性。用廣義碎形維度與波分量強度頻譜可以觀測到在轉變點上隨著系統尺度的不變性。我們精確計算了波分量強度頻譜，在轉變點上，我們的結果與安德森模型有高度的一致性，證明了波分量強度頻譜也是一個具有普適性的量。

Localization-Delocalization Transition of the Instantaneous Normal Modes in a Simple Fluid

Student : Ban-Chiech Huang   Adviser : Ten-Ming Wu

Institute of Physics
National Chiao-Tung University

Abstract

In this thesis, we have investigated the localization-delocalization transitions (LDTs) of the instantaneous normal modes (INMs) in a simple fluid with short-ranged interactions. The model fluid is a prototype of topologically disordered systems. Two LDTs in the INM spectrum are found, and the locations are termed as the mobility edges (MEs) with one in the positive-eigenvalue branch and the other in the negative-eigenvalue one. The MEs and the critical exponents of the two LDTs are estimated by the finite-size scaling (FSS) for the second moments of the nearest-neighbor level-spacing (LS) distributions. Within numerical errors, the two estimated critical exponents are almost coincident with each other and close to that of the Anderson model (AM) in three dimensions. The nearest-neighbor LS distribution at each ME is examined to be in a good agreement with that of the AM at the critical disorder. We conclude that the LDTs in the Hessian matrices of topologically disordered systems exhibit the critical behaviors of orthogonal universality class.

We also investigate the analysis of level-number variance (LNV) and level compressibility (LCP), which characterizes the nature of the correlation of energy levels beyond the mean LS. Furthermore, in terms of the multifractal analysis, the INM eigenvectors exhibit a multifractal nature with the same generalized fractal dimensions and the sigularity spectrum. Our results indicate that the singularity spectrum of the multifractal INMs agrees with that of the AM at the critical disorder. This good agreement provides a numerical evidence for the universality of the multifractal at the localization-delocalization transition. With the multifractal INMs, we calculate the probability density function and the spatial correlation function of the squared vibrational amplitudes. With the multifractal INMs, the relation between the probability density function and the singularity spectrum is examined, so are the relations between the critical exponents of the spatial correlation function and the generalized fractal dimensions.

致　　謝

　　感謝 神，帶領我走過在交大物理所博士班的考驗。謝謝吳天鳴教授，引導我進入軟物質與複雜系統的領域，讓我經歷到在學術上嚴謹要求的震撼，並且親自成為榜樣。一路上經歷許多高山、低谷，謝謝吳老師以 神的恩慈，包容我在個性上的無知與輕率，還有許多的不尊重，忍受我因為個人因素，在研究上的不積極。
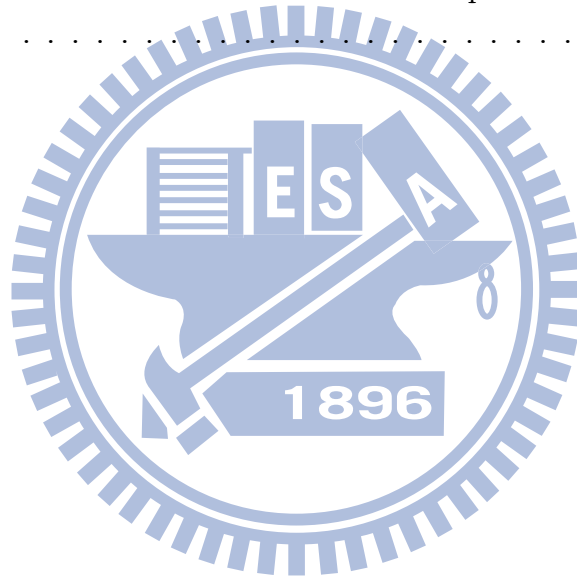
　　謝謝張世良學長，他為這個工作立下了重要基礎，無論是演算法或理論上。博士班的同學，昆憲、宗哲、葛老大是一同走過許多戰役的戰友。感謝平翰、德明、柏翰、在許多問題上的討論，以及一同打籃球的時光。感謝文絢學姐許多的幫忙與鼓勵，謝謝張正宏老師提供的討論。謝謝我的妻子瑩真，辛苦的維持一個家與兩個小孩，謝謝岳父母在許多地方及時伸出援手，我的弟妹，邦浩、詩婷一路上的支持。

　　最後謝謝我的父母，謹將本文獻給他們。

Contents

List of Figures

List of Tables

List of Abbreviations

AH	Anderson Hamiltonian
AM	Anderson model
CWI	Cullum-Willoughby implementation
DOS	Density of states
FSS	Finite-size scaling
GOE	Gaussian orthogonal ensemble
GA	Gaussian Approximation
INM	Instantaneous normal mode
IPR	Inverse participation ratio
JADAMILU	Jacobi-Davidson method with efficient multilevel incomplete LU preconditioning
LCP	Level compressibility
LDT	Localization-delocalization transition
LNV	Level-number variance
LPD	Local probability density
LS	Level-spacing
ME	Moblility edge
MFA	Multifractal analysis
PA	Parabolic Approximation
PDF	Probability density function
PES	Potential energy surface
RG	Renormalization group
RMT	Random Matrix theory
SSP	Singularity spectrum
TLJ	Truncated Lennard-Jones potential

Chapter 1

Introduction

In solid state physics, the electronic band structures, which well predict the nature of crystalline materials such as: metal, insulator or semiconductor, have been well discribed by the Bloch theory since the periodicity structure of materials. However, in amorphous materials, the topological disorders affect the mediating waves strongly [1]. Due to the lack of periodicity and the multiple scattering, the electronic or vibrational waves lose phase coherence in the short wave limit, the vavevector is no longer a good quntum number, and a well defined energy band is absent. Instead of the energy band, another comprehensive view for such waves are the density of states (DOS). The transport property such as the electronic conductivity and thermoconductivity closely relate to the spatial distribution of mediating waves. Generally, in amorphous materials the tailing states of the DOS which can not contribute to transport are termd as the localized states.

In 1958, P.W. Anderson introduced the concept of *localization* for the non-interacting electronic system at $T = 0 \ K$ [2][3]. For systems expected to be a metal by the Bloch theory, there is no energy gap near the Fermi level. But *the localization* forces the materials with strong disorder to actually behave like an insulator, due to the trap of electrons by quantum wave interference in a finite region [4]. Consequently, in 1968, Mott proposed the connection of localization with the transport properties of amorphous semiconductors and the concept of *the mobility edge* **(ME),** which separetes the localized states from the extended states energetically, as shown in Fig.1.1 [5][6][7].

One central theme of the localization properties is the scaling behavior. In 1979,
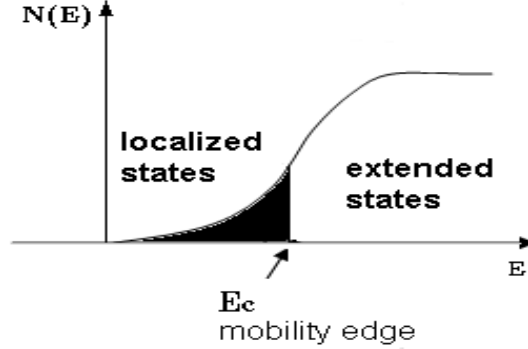
Figure 1.1: The conduction band in a non-crystalline material; E_c indicate the mobility edge and energies for which states are localized are shaded.

Abraham et. al. formulated *the one-parameter scaling theory of localization* [8]. For a hypercube of volume L^d, a generalized dimensionless conductance is defined as

$$g(L) = \frac{2\hbar}{e^2} G(L) = \frac{\Delta E(L)}{dE(L)/dN},$$

where $G(L)$ is the average DC conductance of the hypercube of size L, $dE(L)/dN$ is the mean spacing of its energy levels, and $\Delta E(L)$ is a quantity relating to the fluctuation of energy levels caused by boundary conditions. The dimensionless conductance itself is an explicit description of the system, and provides a relevant scaling variable to describe the critical behavior of the DC conductivity and localization length. Its logarithmic derivative β is introduced as

$$\beta(g(L)) = \frac{d \ln g(L)}{d \ln L}.$$

Fig. 1.2 shows the $\beta(g(L))$ with respect to $\ln g(L)$. For $\beta > 0$, the conductance increases with the size of the sample, reflecting metallic behavior. On the other hand, if $\beta < 0$, $g(L)$ decreases with L, eventually terminating in the localized regime. $\beta = 0$ corresponds to a disorder-induced *metal-insulator transition*(MIT). One of the essential results predicted by the one-parameter scaling theory is that such a MIT can only exist in systems in three dimensions.

According to the theory of phase transitions and critical phenomena, a phase transition can be classified into *the first-order phase transition* and *the continuous phase*

2
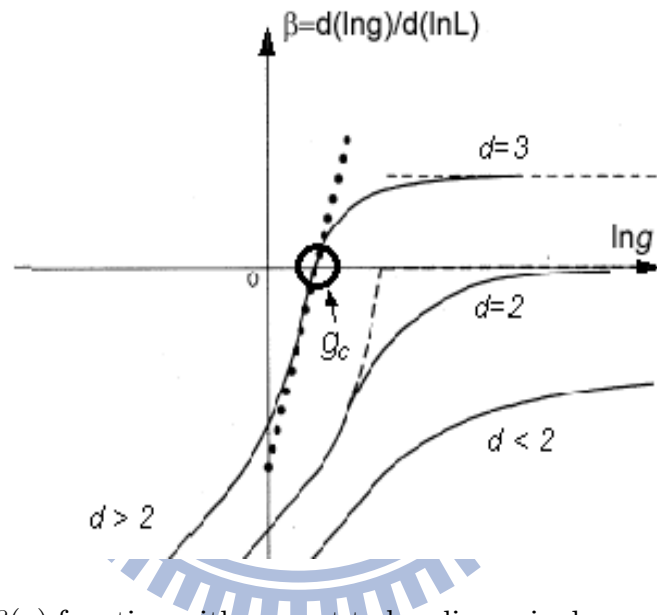
Figure 1.2: The $\beta(g)$ function with respect to log dimensionless conductance. The abscissa indicate log dimensionless conductance. Different lines are specified by spatial dimension, and the crossing point g_c of the line for $d = 3$ indicate the metal-insulator transition.

transition [9] . The main difference of the two classes is whether or not the latent heat, which is proportional to the second derivative of free energy, exist. The first order phase transiton is charaterized by the existance of the latend heat, while the continuous phase transition is not. For the continuous phase transitions, a main character is the divergence of *the correlation length* ξ which describes the spatial extent of fluctuations in a physical quantity about the average of that quantity. Generally, the correlation length of a first-order phase transtion is finite [10].

Another concept related to critical phenomena is *the universality.* Close to a critical point, the correlation length exhibits power-law dependence on the parameters specifying the distance away from the critical point. The powers are specified by the *critical exponents* which only depend on the universality class of the system. The fact that two apparently different physical systems share precisely the same sets of critical exponents is known as the universality, such as the liquid-gas critical point of a simple material and the Curie temperature in a ferromagnet. In general, the universality is classified into categories, which depend on the symmetry group of the Hamiltonian, the dimensionality and whether or not the interactions are short-ranged [11]. According to *the Random Matrix theory* (RMT) developed by Wigner and Dyson [12], Hamiltonians can be classified into three generic ensembles: unitary, orthogonal, and symplectic, which depend on whether or not the time reversal symmetry and the spin-rotation symmetry hold. If the time reversal symmetry is broken, the Hamiltonians are arbitrary Hermitian matrices, $H = H^\dagger$, which is invariant with respect to the unitary transformation; hence is classified as "unitary ensemble". If both the time reversal symmetry and the spin-rotation symmetry are preserved, the Hamiltonians are real symmetric matrices, $H = H^T = H^*$, which is classified as "orthogonal ensemble". If the time reversal symmetry is preserved but the spin-rotation symmetry is broken, the corresponding symmetry class is "sympletic ensemble" [13][14].

The Anderson Hamiltonian (AH) for electron transport in disordered lattices is a well-known model to study its universal properties of *the localization-delocalization transition* (LDT). Due to the spinless feature, the AH belongs to the orthogonal ensemble. In the three-dimensional case, the LDT of the AH is induced by disorder.

Under the tight-binding approximation, the AH is written as

$$H = \sum_{i=1} \varepsilon_i \left| i \right\rangle \left\langle i \right| + \sum_{(i,j)} \left| i \right\rangle \left\langle j \right|,$$

where i and j are nearest-lattice sites. The site energy ε_i of site i is measured in unit of the overlap integral between adjacent site, and ε_i are distributed around zero within the interval $-W/2 \leq \varepsilon_i \leq W/2$, where W denotes the strength of the disorder. If the amount of disorder W is smaller than the critical value, the states in the two ends of the energy spectrum are localized in space, but those in the central region of the spectrum still delocalized. A sharp boundary between the regions of the localized and delocalized states is the ME. If we increase the amount of disorder W to the critical disorder W_c, all states in the energy spectrum are localized in space. In 3D isotropic Anderson model, it is generally accepted that $W_c = 16.5$. Many numerical works in recent decade devoted to calculate the correlation-length exponent ν [15][16] and, so far, it is accepted that the most precise result is $\nu = 1.57 \pm 0.02$ [17].

On the other side, a new thinking way emerged in the liquid theory in 1989. Stratt and Xu proposed a tight-binding model in a liquid to get the band structure in a liquid [18]. Furthermore, to solve dynamical problem from the static point of view, from the fundamental aims of nonequilibrium statistical mechanics, Seeley and Keyes proposed the normal-mode analysis of liquids [19], which is the so-called instantaneous normal mode (INM) analysis. Consequently, rigorous analytical works for the INM theory are carried out by solving the master equation [20] (or renormalized mean-field theory) and the diagram method [21]. Generally, the INM theory provides a comprehensive description for supercooled liquid dynamics in the short-time scale and the optical experiments related to Raman and IR spectra [22][23].

The localization of INMs has been purposed to explain the glass transitions and thermal conductivities of amorphous materials. When a liquid is cooled rapidly, the nucleation of the crystal does not occur and the system becomes a supercooled liquid and then undergoes a transition to a glass at temperature T_g which is characterized by large shear viscosity up to 10^{13} poise [24]. By the INM analysis, some works predicted that the glass transition is associated with a transition temperature below which all unstable INMs become localized [25][26][27]. Another long-standing issue in glasses materials is the physical mechanism for the universal feature of thermal

conductivity, which shows a plateau beteween $10 - 50K$ and further rises [28]. One of the theories explains that the existance of mobility edge in the phonon spectrum causes the plateau [29].

Recently, the fractal concept in condensed matter physics is widely applied. Although the fractal dimension provides a measurement to describe complex objects, it is not enough for a single exponent to characterize the strong fluctuations of the wave amplitudes at a transition point. A suitable approach was lack until the multifractal concept, which was originally introduced by Mandelbrot to describe the distribution of energy dissipation in turbulent flows, is proposed [30][31]. Consequently, the concept of multifractals was applied in many fields such as attractor [32][33], the fully developed turbulence [34][35], the diffusion-limited aggregation (DLA) [36][37][38][39][40] and human physiology [41]. It has been suggested that the critical states show multifractal structures, which also reveal the universality of the critical phenomena [42].

Traditionally, for a normalized eigenvector $\sum_i |\psi_i|^2 = 1$, where i is the index of particle, the mobility edge is often determined by the inverse participation ratio (IPR), which is defined as a sum over fourth-moment of the eigenvector amplitude

$$IPR = \sum_i |\psi_i|^4 .$$

Basically, the IPR approaches to one for a localized state and proportional to $1/N$ for a uniform extended state. However, due to the finite-size effect and the lack of clear distinguishing criteria, the location of the ME can not be precisely identified. In this thesis, inspired by the metal-insulator transition of disordered systems, we focus on the LDT of the INMs in a simple atomic fluid. The main questions that I try to answer in this thesis are: How can we precisely determine the MEs in the INM spectrum, and whether or not the LDT of the INMs and that of the AM belong to the same universal class. To clearly understand the strong fluctuations of waves near the ME, we directly study the eigenvectors of the INMs. By multifractal analysis, the universality is verified again.

The thesis is organized as following: the INM theory of a simple fluid and the numerical method are introduced in chapter two. In chapter three, the critical exponent of the correlation length is predicted by the nearest-neighbor level-spacing statistics and the finite-size scaling analysis, and the critical level-spacing distribution at LDT

of the INM spectrum is determined carefully. In the level statistics, the level-number variance is present in the chapter four. The multifractal analysis is given in chapter five. Finally, I give conclusions in chapter six.
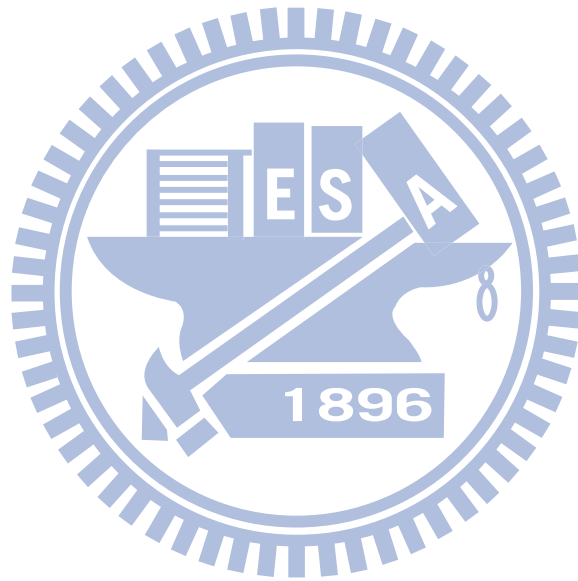
Chapter 2

Instantaneous Normal Mode Theory and Numerical Method

2.1 Instantaneous normal modes of a simple fluid

We consider a fluid of N equal-mass particles whose total potential energy $V(R)$ in configuration $\mathbf{R}$ is a sum of the pair potential $\phi(r)$ for all particle pair,

$$V(R) = \sum_{i=1}^{N-1} \sum_{j<i}^{N} \phi(r_{ij}).$$

Through the entire thesis, we investigate the truncated Lennard-Jones (TLJ) fluid, which the TLJ potential $\phi_{TLJ}(r)$ is obtained by truncating the Lennard-Jones (LJ) potential $\phi_{LJ}(r)$ at the minimum $r_c = 2^{1/6}\sigma$ and then lifting up in energy by ϵ,

$$\phi_{LJ}(r) = 4\epsilon \left[\left(\frac{\sigma}{r}\right)^{12} - \left(\frac{\sigma}{r}\right)^{6} \right],$$

$$\phi_{TLJ}(r) = \begin{cases} \phi_{LJ}(r) + \epsilon, \ r < r_c \\ 0 \qquad\qquad , \ r > r_c \end{cases}$$

where σ and ϵ are the length and energy parameters of the LJ potential. So, the TLJ potential is purely repulsive. We choose the thermodynamic state of the TLJ fluid at reduced density $\rho^* = 0.972$ and reduced temperature $T^* = 0.836$ in the units of the two LJ parameters. With N particles confned in a cube of length $L = (\frac{N}{\rho^*})^{1/3}$ and using the periodic boundary condistions, the fluid configurations are generated by Monte Carlo simulation for six system sized from $N = 3000$ to 96000.

In a short-time scale, a harmonic approximation can be applied for $V(R)$[20], and by expanding $V(R)$ to the second order of particle dispalcements about $\mathbf{R}_0$

$$V(\mathbf{R}) = V(\mathbf{R}_0) - F(\mathbf{R}_0) \cdot (\mathbf{R} - \mathbf{R}_0) + \frac{1}{2}(\mathbf{R} - \mathbf{R}_0) \cdot \mathbf{K}(\mathbf{R}_0) \cdot (\mathbf{R} - \mathbf{R}_0), \qquad (2.1)$$

where $\mathbf{R}$ and $F(\mathbf{R}_0)$ denote $3N$-dimensional vectors of position and force. Since $\mathbf{R}_0$ may not be a configuration at local minimum, $F(\mathbf{R}_0)$ is generally non-zero. $\mathbf{K}(\mathbf{R}_0)$ is the $3N$-dimensional Hessian matrix composed of 3×3 blocks, which are functions of relative displacements of particle pairs. Let $\mathbf{U} = \mathbf{R} - \mathbf{R}_0$, the displacement from $\mathbf{R}_0$. For the harmonic potential in Eq.(2.1), the equations of motion are

$$\ddot{U} = F(\mathbf{R}_0) - \mathbf{K}(\mathbf{R}_0) \cdot \mathbf{U}.$$

By defining a shifted coordinate Q,

$$Q = U - K^{-1} \cdot F,$$

this leads to the equation of motion

$$\ddot{Q} = -\mathbf{K}(\mathbf{R}_0) \cdot Q.$$

The configuration of interacting particles can be specified as a point in the high-dimensional *potential energy surface(PES)*. The dynamics of the system can be described as moving from point to point through the PES, which is composed of many mountains, valleys and saddle points. The eigenvalues of the Hessian matrix are the curvatures of the PES, where a positive eigenvalue corresponds a valley of a degree of freedom, while a negative one could be the curvature at a mountain top or a saddle point of another degree of freedom. The square roots of the eigenvalues characterize the frequencies of the system. It was also proposed that the negative eigenvalues specified as "true unstable modes" contribute to the self-diffusion coefficient[54].

For a pairwise-sum total potential, the elements of Hessian matrix $\mathbf{K}(\mathbf{R}_0)$ which are the second derivatives of $V(R)$ with respect to particle index i, j and coordinate

index μ, ν, are expressed as

$$
\begin{aligned}
\mathbf{K}_{i,j;\mu,\nu} &= \frac{\partial^2}{\partial r_{i\mu} \partial r_{j\nu}} V(R)|_{R=R_0}, \\
&= \begin{cases} -\mathbf{t}(r_{ij}), & i \neq j, \\ \sum_{i \neq j} \mathbf{t}(r_{ij}), & i = j, \end{cases} \\
\mathbf{t}(r) &= \frac{\phi'(r)}{r}\mathbf{I} + [\phi''(r) - \frac{\phi'(r)}{r}]\widehat{r}\widehat{r},
\end{aligned}
$$

where $\mathbf{I}$ is the 3-dimensional unit matrix, $\phi'(r)$ and $\phi''(r)$ denote the first and second derivatives of $\phi(r)$ with respect to r, $\widehat{r}$ is the unit vector along $\overrightarrow{r}$, and $\mathbf{t}(r)$ is a 3×3 matrix. Owing to the short-range nature of the TLJ potential, the Hessian matrices are sparse. The ratio, f_{opp}, of the nonzero off-diagonal blocks in a Hessian matrix is estimated to be N_c/N, where N_c is the average number of neighbors around a particle within r_c. Evaluated by the radial distribution function of the TLJ fluid, N_c is about 6 and independent of N. Thus, f_{opp} is inversely proportional to N, with a value about 0.05% for $N = 12000$. For each Hessian matrix, the trace of the off-diagonal block associated with particless i and j at distance r_{ij} is given by the negative of $k_{ij} = \phi''_{TLJ}(r_{ij}) + 2\phi'_{TLJ}(r_{ij})/r_{ij}$, where $\phi''_{TLJ}(r_{ij})$ and $\phi'_{TLJ}(r_{ij})/r_{ij}$ are, respectively, the force constants of the vibrational and rotational binary motions of the two particles[55]. The trace of the diagonal block associated with particle i, expressed as $\sum_{j \neq i} k_{ij}$, is the sum of all force constants connected to this particle. For the TLJ fluid, the traces of the diagonal and off-diagonal blocks are positive and negative values, respectively, and their averages, denoted as $\overline{k_{tot}}$ and $-\overline{k}$, are related via the equation $\overline{k_{tot}} = N_c\overline{k}$.

The elements of each Hessian matrix are subject to constraints[45] , which are classified into three categories: First, the off-diagonal matrix elements represent the force constant between pairs of atoms and diagonal ones represent the force on a given atom from all of the other atoms. The balance of these two kinds of force cause *momentum conservation of the system*, and subsequently, sum rules between the diagonal and off-diagonal blocks which makes the diagonal blocks determined by the off-diagonal ones as follow;

$$
\sum_{i=1}^{N}\mathbf{K}_{i,j;\mu,\nu} = \sum_{j=1}^{N}\mathbf{K}_{i,j;\mu,\nu} = 0.
$$

The Second is the triangle rule for the relative positions of any three particles[46] , which makes only $N-1$ off-diagonal blocks independent, with N being the particle number of the system. The Third is the internal constraints of each off-diagonal block, which reduce the degrees of freedom of an off-diagonal block to the three components of relative displacement of the related particle pair. None of these constraints appear in the AM. The triangle-rule constraints are not considered in those vibrational models with a lattice reference frame[49][50] . The third constraints are ignored in the scalar-vibration models[51]. The Hessian matrix can be recognized as a generalized version of the Euclidean random matrices[48], with randomness originated from the disorder of particle positions.

The randomness of the elements in the Hessian matrices can be described by four distributions: two for characterizing the traces and the off-diagonal elements of the diagonal blocks and the other two for the corresponding quantites of the off-diagonal blocks[56]. The four distributions of the TLJ fluid are shown in Fig. 2.1. Some features of the four distributions are given in the following: first, the distributions of the traces are asymmetric about their averages. Depending on the pair potential in the fluid, the distribution for the off-diagonal blocks has a sharp cusp, which is a result of the short-range nature of the TLJ potential[56]. Second, the distributions of the off-diagonal elements are symmetric about their averages, which are zero. The distribution for the off-diagonal blocks can be fit with a Lorentzian, reflecting the complete independence of the off-diagonal elements in the associated blocks. However, the distribution for the diagonal blocks can only be fit with a pseudo-Voigt function, which is a wighted linear combination of a Lorentzian and a Gaussian; the weighted factors of the Lorentzian and the Gaussian are about 40% and 60%, respectively. The reason why the pseudo-Voigt function is used is reulted from that the distribution is caused by a summation of the off-diagonal independent elements in the off-diagonal blocks and the number of the independent elements in the summation is about N_c, which is only a few in our model.
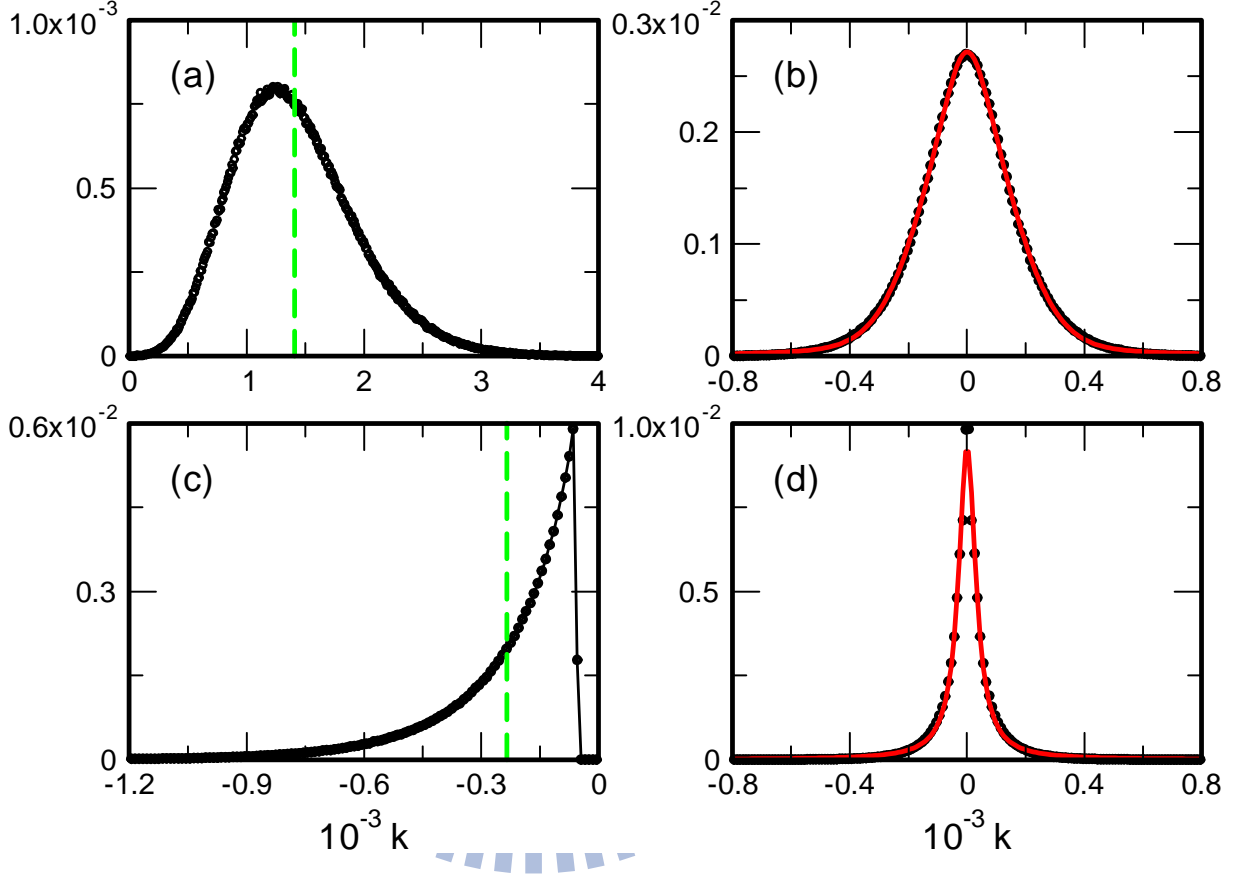
Figure 2.1: Normalized distributions of the elements in Hessian matrics of the TLJ fluid at $\rho^* = 0.972$ and $T^* = 0.836$: (a) for the traces of the diagonal blocks; (b) for the off-diagonal elements in the diagonal blocks; (c) for the traces of the off-diagonal blocks; and (d) for the off-diagonal elements in the off-diagonal blocks. In all figures, the abscissas are force constants in the units of ϵ/σ^2 and the symbols are the numerical data. The dashed lines in (a) and (c) indicate the averages of the distributions, which are $\overline{k_{tot}}$ and $-\overline{k}$, respectively. The solid line in (b) is the fit result with a pseudo-Voigt function, and the line in (d) is that with a Lorentzian.

2.2 Numerical method

There are two main parts in our numerical works, one is to generate configurations at a thermodynamic state and the other is to diagonalize the Hessian matrice. We wil brief review the algorithm of the Monte Carlo method in section 2.2.1. Moreover, the time-comsuming part is to solve the eigenvalues problem. The sparse nature of the Hessian matrices in our problem can be solved by many efficient algorithms. Two different stratege are used: first, for the level-statistics problem in chapter three and four, no eigenvectors are needed and the eigenvalues are solved by the Cullum-Willoughby implementation(CWI) Lanczos method[82]. Second, the multifractal problem in which a few eigenvectors in a selected region are required, so the JADAMILU package which is a combination of the Jacobi-Davidson (JD) method and the efficient multilevel incomplete LU (ILU) preconditioning, is usedl[81][83]. In the JADAMILU package, modest memories are required and robust convergence to accurate solutions. We introduce briefly the two algorithms in section 2.2.2 and 2.2.3. The numerical fitting process is summaried in last section 2.2.4.

2.2.1 The Monte Carlo method

The monte carlo method follows the canonical ensemble and is widely used in numerical simulations [84]. Here we briefly introduce the algorithm.

Define an initial configuration $\mathbf{R}_0$ and a trial moving $\mathbf{R}_0 + \Delta \overrightarrow{r_1}$ where a particle move randomly to nearby region with a distance d away from original position. The energy difference of the two configurations is $\Delta V = V(\mathbf{R}_0 + \Delta \overrightarrow{r_1}) - V(\mathbf{R}_0)$. The system follows the Boltzmann distribution, and define the probability of a state $\rho(\mathbf{R}_0)$

$$\rho(\mathbf{R}_0) = \frac{e^{-V(\mathbf{R}_0)/k_B T}}{Z},$$

where $Z = \sum e^{-V/k_B T}$ is the partition funciton. The probability of acceptance for the trial moving is the transition probability

$$\frac{\rho(\mathbf{R}_0 + \Delta \overrightarrow{r_1})}{\rho(\mathbf{R}_0)} = \frac{Z^{-1} \cdot e^{-V(\mathbf{R}_0 + \Delta \overrightarrow{r_1})/k_B T}}{Z^{-1} \cdot e^{-V(\mathbf{R}_0)/k_B T}} = \frac{e^{-V(\mathbf{R}_0)/k_B T} \cdot e^{-\Delta V/k_B T}}{e^{-V(\mathbf{R}_0)/k_B T}} = e^{-\Delta V/k_B T}.$$

If $\Delta V < 0$, the transition probability $e^{-\Delta V/k_B T} > 1$, the moving is accepted. If $\Delta V > 0$, a random nuber s will be generated. If $e^{-\Delta V/k_B T} > s$, the trial moving is

accepted. Otherwiese, if $e^{-\Delta V/k_B T} < s$ the trial moving is rejected. Consequently, the trial moving of particle two is performed. A complete monte carlo step is defined as that every single particle of $\mathbf{R}_0$ is purturbed.

In a monte carlo step, the trail moving of some particles are accepted while others are not. The accepted rate of total trial moving in a monte carlo step depends on the choosing of d and is related with the speed for a system reaching equilibrium. In our algorithm, about 40000 monte carlo steps system are used to reach the equilibrium.

2.2.2   The CWI Lanczos method

The Lanczos precedure works by generating a Krylov sequence, projecting the original matrix onto this subspace, producing a tridiagonal matrix, and then finding the eigenvalues of this resulting tridiagonal matrix. These eigenvalues converge on those of the originl matrix with increasing size of the Krylov space. The basic single-vector Lanczos recursion as follow:

Let A be a $n \times n$ real symmetric matrix and generate a unit starting vector v_1 randomly. Define corresponding Lanczos matrices T_k for $k = 1, 2, ..., m$ using the following recursion. Define $\beta_1 = 0$, and $v_0 = 0$. Then for $i = 1, 2, ..., m$, the Lanczos vectors v_i and scalars α_i and β_{i+1} are

$$\begin{aligned}
\beta_{i+1} v_{i+1} &= Av_i - \alpha_i v_i - \beta_i v_{i-1}, \\
v_i^T A v_i &= \alpha_i \text{ and } \beta_{i+1} = v_{i+1}^T A v_i.
\end{aligned} \tag{2.2}$$

Rewriting Eq.(2.2) in matrix form, for each k we obtain the matrix equation

$$AV_k = V_k T_k + \beta_{k+1} v_{k+1} e_k^T,$$

where $V_k \equiv \{v_0, v_1, ..., v_k\}$ is the $n \times k$ matrix whose i-th column is the i-th Lanczos vector, and e_k is the coordinate vector whose k-th component is one and whose other components are zero. The transfomation is written as $V_k^T A V_k = T_k$, and T_k is the

$k \times k$ tridiagonal matrix.

$$T_k \equiv \begin{bmatrix} \alpha_1 & \beta_1 & & & \\ \beta_1 & \alpha_2 & \ddots & & \\ & \ddots & \ddots & \ddots & \\ & & \ddots & \ddots & \beta_j \\ & & & \beta_j & \alpha_j \end{bmatrix}$$

In principle, the v_i are all orthogonal to each other; however, in practice, as the iteration is continued the arithmetic carried out by the computer causes the finite precision. Therefore, the orthogonality among the vectors v_i is gradually lost. The loss of orthogonality results in the appearance of spurious 'ghost' eigenvalues, and also the repetition of real eigenvalues.

The CWI implementation identifies the ghost eigenvalues by comparing the eigenvalues of T_k and T'_k, where T'_k is the matrix T_k with its first row and column removed. If an eigenvalue appears in both, it is discarded as being a spurious eigenvalue. The CWI algorithm also gives error estimates for the eigenvalues, and thus the number of iterations required can be tuned such that all the interesting eigenvalues are converged to within some tolerance.

2.2.3   The JADAMILU method

The underlying algorithm of JADAMILU combines the Jacobi-Davidson (JD) method with efficient multilevel incomplete LU (ILU) preconditioning which has been used to solve many problem sucessively[81][85]. The detail of JD method is refered to the original paper[83] and reference therein. The main features of JADAMILU are modest memory requirements and robust convergence to accurate solutions.

The preconditioning plays a key role in the speed of execution. For a given matrix C, a good preconditioner is a matrix P that is cheap to contstruct and invert, while still being a good approximation of the original matrix. This means $P^{-1}C$ is close to the indentity matrix, whereas cheap to invert means that solving a system $Px = y$ should not cost more than a few multiplications by C.

The algorithm can calculate a single eigenvalue and the corresponding eigenvector close to desired value σ. When more eigenvectors are sought, the code uses a simple

deflation process: the algorithm is restarted but restricted to the subspace orthogonal to converged eigenvectors. Experiments show that the later eigenvectors can be computed with similar accuracy. In practice, if several eigenvalues are desired, some eigenvalues close to the boundary of the interval could be missed.

2.2.4   The numerical fitting

The analysis of experimental data often connects with the fitting process. Scientist should proposed a theoretical model to explain the experimental data. Whether the model is good should be justified by statistical analysis carefully. The conventional error function χ^2 is defined as

$$\chi^2 = \sum_{i=1}^{N} \left[\frac{y_i - y(x_i; a_1, ..., a_M)}{\sigma_i} \right]^2,$$

where the number of data and parameters correspond to N and M, y_i is experiment data, σ_i is the error bar of each point and the model $y(x_i; a_1, ..., a_M)$ depend on fitting parameters a_j. Furthermore, it is necessary to have a good algorithm to minimize the χ^2 function, a general fitting process. What we use is the *amebsa method* from *Numerical recipes[47]*. Basically, the amebsa method is a simulated annealing method, which tries to quench the error function in parameter space down to the global minimum. The core of amebsa method is the downhill simplex method that requires only function evaluations, not derivatives. It is a good strategy to avoid falling local minimum that model the fitting process as the system quenching with appropriate initial temperature and quench rate.

Beside good algorithm, to estimate the goodness-of-fit of the data to the model, the chi-square probability Q is used in statistics books frequently. Defining $D = N - M$ as the number of degrees of freedom, the quantity Q is

$$Q = gammaq \left(\frac{D}{2}, \frac{\chi^2}{2} \right),$$

where *gammaq* returns the value $Q(a, x) = 1 - P(a, x)$, and $P(a, x)$ denotes imcomplete gamma function

$$P(a, x) \equiv \frac{\gamma(a, x)}{\Gamma(a)} \equiv \frac{1}{\Gamma(a)} \int_0^x e^{-t} t^{a-1} dt \quad (a > 0).$$

It is an important point that the chi-square probability Q assumes that the measurement errors are normally distributed. It is quite common, and usually not to wrong, to assume that the chi-square distribution holds even for models that are not strictly linear in the a's.

The Q value gives a quantitative measure for the goodness-of-fit of the model, generally a acceptable fitting for $1 < Q < 0.01$. If Q is a very small for some particular data set, then the apparent discrepancies could be due to following reasons: (i) the model is wrong: can be statistically rejected, or (ii) the measurement errors σ_i are really larger than announcement. (iii) the measurement errors may not be normally distributed. The possibility (iii) is fairly common, therefore, reasonable experimenters are often rather tolerant of low probabilites $Q > 0.001$. On the other side, if Q is too near to one, that might be due to overestimated measurement errors.

Furthermore, it is important in statistics to estimate error bar of parameters, such as commonly used the 95 confident interval. Our strategy is to generate a set of synthetic data within the error bar of original data by the random number. The distribution of fitting parameters can be extracted by fitting those synthetic data. For the normal distribution of parameters, the 95 confident interval refers to 1.96 times standard deviation of the distribution of parameters.

Chapter 3

The Nearest-Neighbor Level-Spacing Statistics

Hessian matrices of topologically disordered systems fall into *the orthogonal universality class* from the viewpoint of the random matrices theory (RMT)[12]. One significant measurement of the RMT is the nearest-neighbor level-spacing (LS) distribution $P(s)$, where s is the difference between the nearest-neighbor energy levels. For the Gaussian orthogonal ensemble (GOE) [12], the strong correlation of two adjacent fully extened eigenstates shows strong level replusion. The LS distribution of the extended eigenstates is described by the Wigner surmise,

$$P_w(s) = \frac{\pi s}{2} \exp(-\frac{\pi s^2}{2}).$$

On the other hand, for completely localized states, the corresponding levels are independent and completely uncorrelated, and the LS distribution follows the Poisson distribution,

$$P_p(s) = \exp(-s).$$

For weak disorders systems, the eigenstates are expected to be delocalized near the band center and localized near the band tails. The variation of the LS distributions from the band center to the tail is continuous from the Wigner surmise to the Poisson distribution.

Some questions rise here: What is the critical LS distribution $P_c(s)$ at the mobility edge? Numerical works suggest that $P_c(s)$ at large s is the Poisson-type with a decay

rate above unity[62][15]; however, some analytical theory predicts other asymptotic behavior[63]. At small s, the behavior of $P_c(s)$ is accepted to be linear with a slope larger than that of the Wigner surmise and depend on the choice of the boundary conditions in the AM[61]. Generally, it is accepted that $P_c(s)$ is invariant of sytem size at the LDT in AM[15][61]. Based on the scale invariance feature of $P_c(s)$, we can determine the mobility edge, and further compare the $P_c(s)$ in INMs and in AM.

3.1 Density of State and Unfolding Process

The Hessian matrices of the TLJ fluid are diagonalized with Lanczos method[82]. Presented in Fig. 3.1 is the normalized INM-eigenvalue spectrum $D(\lambda)$, which is an average for the realizations generated for each system size. Quite asymmetric with respect to the maximum at zero eigenvalue, the spectrum $D(\lambda)$ consists of two branches, one with positive eigenvalues and the other with negative eigenvalues. One ME is expected to occur in each branch. With the LS analysis given below for systems of smaller sizes from $N = 375$ to $N = 1500$, the MEs in $D(\lambda)$ are found within the range $\lambda = 1150 - 1230$ and $\lambda = -95 \sim -80$, which are the two shaded regions in Fig. 3.1.

The INM density of states in the shaded region in the positive branch is about four times smaller than that in the shaded region in the negative branch. For equal statistical samples in both branches in each system size, the number of diagonalized matrices for the positive branch is four times of that for the negative branch; this makes the calculations for the positive branch much more difficult.

To do the LS analysis for eigenvalues from λ_1 to λ_2, the conventional unfolding process is applied in our system

$$z_i = \frac{1}{D_0} \int_{\lambda_1}^{\lambda_i} D(\lambda) d\lambda, \tag{3.1}$$

where $D_0 = \int_{\lambda_1}^{\lambda_2} D(\lambda) d\lambda$ is the percentage of the eigenvlues within the integral range. Shown in the insets of Fig.3.1 are the unfolding procedures for the eigenvalues within the two shaded regions, with the unfolded eigenvalues z_p and z_n for the positive and negative branches, respectively. The unfolded eigenvalues spectrum has been checked to be unifromly one.

19
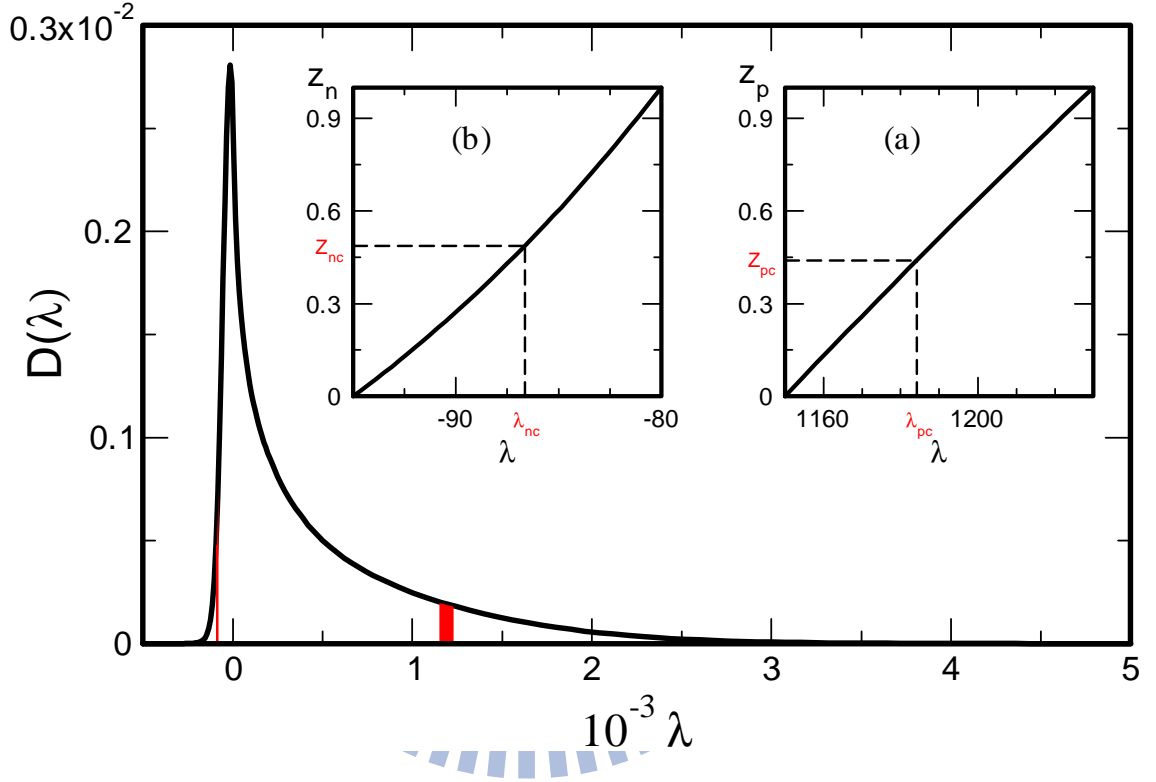
Figure 3.1: Normalized INM-eigenvalue spectrum of the TLJ fluid at $\rho^* = 0.972$ and $T^* = 0.836$. λ is in unit of $\varepsilon/m\sigma^2$, where m is the particle mass. The two insets show the unfolding procedures for the eigenvalues within the two shaded red regions in the main figure: (a) for λ between 1150 and 1230 and (b) for λ between -95 and -80. λ_{pc} and λ_{nc} are the locations of the MEs in the positive and negative branches, respectively.

N	L	λ from 1150 to 1230			λ from -95 to -80		
		M	$N_s \times 10^{-6}$	$\triangle \times 10^3$	M	$N_s \times 10^{-6}$	$\triangle \times 10^3$
3000	14.56	128000	17.65	7.2	32000	3.020	10.5
6000	18.38	64000	17.65	3.6	16000	3.035	5.2
12000	23.12	32000	17.65	1.8	8000	3.042	2.6
24000	29.12	16000	17.65	0.9	4000	3.037	1.3
48000	36.69				2000	3.052	0.65

Table 3.1: Numerical data of the LS statistics for the eigenvalues in the indicated ranges. N: number of particles; L: length of the simulated box in the LJ unit; M: number of samples; N_s: total number of LS; $\triangle$: mean LS; $\triangle = (3ND_0)^{-1}$, where D_0, the percentage of the eigenmodes in the range, equals to 1.54×10^{-2} and 1.06×10^{-2} for the positive and negative eigenvalues, respectively.

For each branch, we select the unfolded eigenvalues in different sections, which have a width $\Delta z = 0.125$ and are centered at $M\Delta z/2$ with M an integer from 1 to 15. For the unfolded eigenvalues z_i in a section, the nearest-neighbor LS is defined as $s_i = (z_{i+1} - z_i)/\Delta'$, where Δ' is the mean LS of the unfolded eigenvalues z_i in this section. The LS data for the two shaded regions in Fig.3.1 are summarized in Table 3.1. For each section, we calculate the nearest-neighbor LS distribution $P(s)$, which is normalized and has a mean of unity. The LS number of each section in the positive branch is about 2.2×10^6, and that of each section in the negative branch is about 3.8×10^5.

Figure 3.2 shows $P(s)$ of $N = 48,000$ for several unfolded-eigenvalue regions, where the unfolding eigenvalues $z = 0$ to 1 correspond to $\lambda = -95$ to -80 in the negative branch. $P(s)$ of small z, which is near the localized regime, is closer to the Poisson distribution. On the other side, $P(s)$ of large z is closer to the Wigner one, corresponding to the delocalized regime.

With the numerical $P(s)$ distribution of each section, we defines a physical measurement, the second moment I_N of $P(s)$,

$$I_N = \int_0^\infty s^2 P(s)ds.$$

The data of I_N, including statistical errors, for the four system sizes in the positive
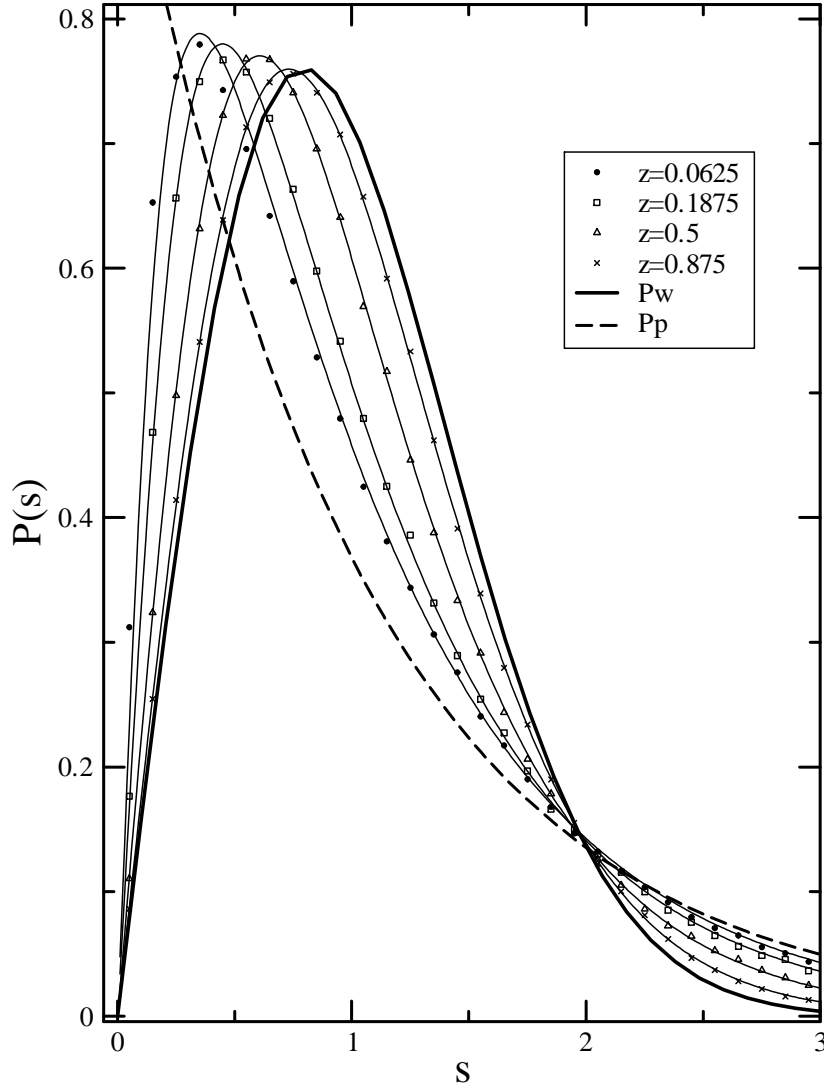
Figure 3.2: The LS distribution of $N = 48,000$ of unfolded eigenvalues z within the negative branch. The unfolding eigenvalues $z = 0$ to 1 correspond to $\lambda = -95$ to -80, respectively. The symbols denote numerical data and the solid line is the fitting by eq.(3.4). The dash and thick solid lines denote Possion and Wigner distributions, respectively.

branch and five system sizes in the negative branch are shown in Fig. 3.3. In principle, the values of I_N fall in a range between $4/\pi$ and 2, which are the second moments of the Wigner surmise and the Poisson distribution, respectively. For each system size, as the selected sectin moves from the delocalized to the localized region, the value of I_N increases monotonically. For each branch, the calculated I_N as a function of the unfolded eigenvalue z generally depends on system size and follows the scaling behavior: I_N increases with N in the localized region but decreases with N in the delocalized region. At some unfolded eigenvalue z_c, I_N is expected to be invariant with N and, therefore, z_c is the location of the ME in the branch.

3.2 The Finite-Size Scaling

According to one-parameter scaling hyperthesis $X = f(N/\xi)$ [8], physical measurement is scaled by the characterized length ξ. Furthermore, we introduce the method of finite-size scaling (FSS) to extract the critical exponent of correlation length and to determine the ME. The FSS method has been used widely to solve the critical phenomena in solid state physics for a long time [52][53] and the fundamental physics of the FSS theory is clearly explained in the framework of RG[11]. In 1999, a correction of the FSS at the Anderson transition was purposed by considering nonlinear effect and the irrelevant variable [17], which gives the correlation length exponent of the AM precisely. Following reference [17], X is expanded as a series up to order n_i

$$
\begin{aligned}
X &= f(\chi_r L^{1/\nu}, \chi_i L^y) \\
&= \sum_{n=0}^{n_i} \chi_i^n L^{ny} \widetilde{f}_n \left(\chi_r L^{1/\nu} \right),
\end{aligned}
\tag{3.2}
$$

where χ_r is relevant variable and χ_i is irrelevant variable. Each $\widetilde{f}_n$ is then expanded as

$$
\begin{aligned}
\widetilde{f}_n \left(\chi_r L^{1/\nu} \right) &= \sum_{i=0}^{n_r} a_{ni} \chi_r^i L^{i/\nu} \\
\chi_r &= \sum_{n=1}^{m_r} b_n Z^n, \qquad \chi_i = \sum_{n=0}^{m_i} C_n Z^n,
\end{aligned}
\tag{3.3}
$$

where $Z = (1 - z/z_c)$ and $b_1 = C_0 = 1$. Each fitting function can be specified by a set of four indices (n_i, m_i, n_r, m_r) and the fitting parameters include those expansion coeffcients, z_c, ν and y.

We fit the I_N data within different intervals of z with the scaling functions given in Eqs.(3.2)-(3.3) for the four system sizes in the positive branch and five system sizes in the negative branch. In a fit for N_d data points with a scalng function of N_p parameters, we use the downhill simplex method to minimize the χ^2 statistics of the data points, while the goodness of fit is measured by the Q factor, which is determined by the best-fit value of χ^2 and $N_d - N_p$, the number of degrees of freedom in the fitting[47]. The detail of the fitting process is described in chapter 2. In order to obtain the confidence intervals of fit parameters, 10^4 synthetic data sets are generated by uniformly sampling each new data within the error bar of the data[16]. The error bars of fit parameters are estimated by those within 95% confidence intervals of its original fit. The acceptance of a fit is determined by two criteria. First, the Q value of an acceptable fit should be larger than 0.01[47]. Second, since the value of ν is determined by the universality class of the random matrices, a large error of ν would make the fitting meaningless. So, we set the error bar of parameter ν for an acceptable fit to be less than 0.2. To keep the number of fit parameters as few as possible, we set $m_i = 0$ for all fits and limit n_r and m_r no more than three. Also, verified by the results given below, no clear shift of the crossing points of the data curves in Fig. 3.3(b) is found so that, for the negative branch, the irrelevant scaling variable is not necessary and n_i is , therefore, set to be zero.

With the criterions given above, only several models are accepted for each branch, and the results are listed in Tables 3.2 and 3.3. The distribution of the ν_p and ν_n values of the accepted models is shown in Fig. 3.4. The average of these models leads us to $\nu_n = 1.60 \pm 0.03$ and $z_{nc} = 0.464 \pm 0.003$, which corresponds to $\lambda_{nc} = -86.98 \pm 0.08$. However, the accepted models for the positive branch are somewhat diversified. The two with ν_p larger than 1.7 have larger χ^2 values than others, causing their Q values less than 0.1. The rest four models without the irrelevant scaling variable have Q values generally more than 0.2 and their ν_p and z_{pc} are close to one another. For the two models in which the irrelevant scaling variable is introduced, the goodness of fit substantially increases and the value of ν_p is relatively lowered; however, the

24
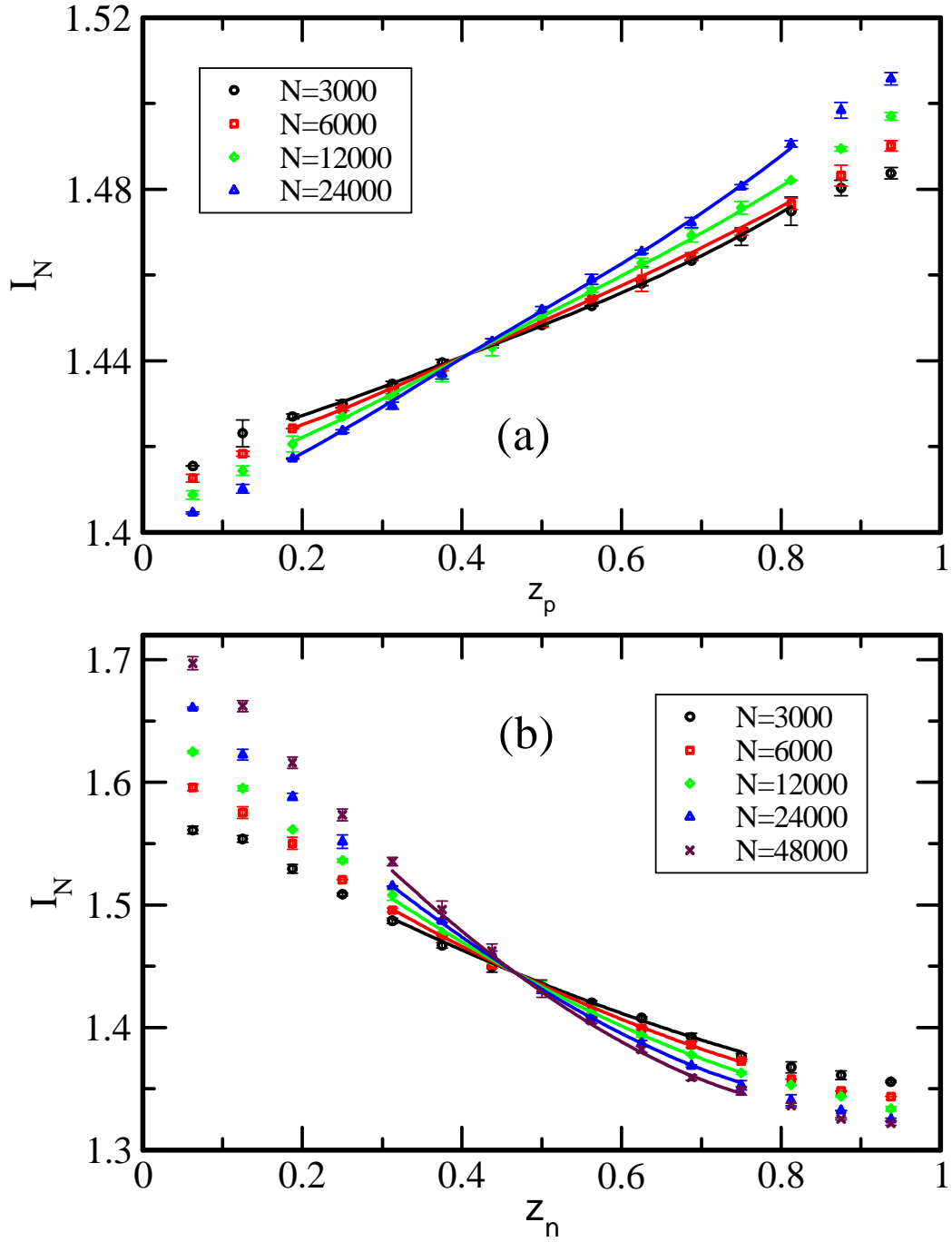
Figure 3.3: The second moment I_N of $P(s)$ as a function of unfolded eigenvalue: (a) for the positive branch and (b) for the negative branch. N is the number of particles in a system. The symbols are the results of the numerical eigenvalues obtained by diagonalization. The lines in (a) are the fitting functions of the model $(1, 0, 3, 3)$ for z_p within $[0.1875, 0.8125]$; the lines in (b) are those of the model $(0, 0, 3, 1)$ for z_n within $[0.3125, 0.75]$.

25

					Positive branch					
$[z_{\min}, z_{\max}]$	N_d	N_p	n_i	n_r	m_r	χ^2	Q	z_{cp}	ν_p	y_p
$[0.25, 0.75]$	36	6	0	2	2	34.98	0.2	0.433(8)	1.59(8)	0
$[0.25, 0.75]$	36	7	0	2	3	35.43	0.19	0.434(8)	1.60(9)	0
$[0.25, 0.75]$	36	7	0	3	2	33.85	0.24	0.428(8)	1.60(9)	0
$[0.25, 0.75]$	36	8	0	3	3	31.69	0.29	0.422(10)	1.52(10)	0
$[0.25, 0.75]$	36	6	0	1	3	41.40	0.08	0.435(9)	1.74(7)	0
$[0.25, 0.75]$	36	6	0	3	1	49.29	0.01	0.438(9)	1.79(10)	0
$[0.1875, 0.8125]$	44	11	1	3	1	30.39	0.60	0.431(14)	1.45(9)	-7.72 ± 5.32
$[0.1875, 0.8125]$	44	11	1	3	3	25.92	0.72	0.409(17)	1.54(10)	-6.00 ± 3.48

Table 3.2: Fit parameters and estimates for z_c, ν and irrelevant exponent y_p for the positive branch. The quoted errors correspond to 95% confidence interval. $z_{\min}$ and $z_{\max}$ give the fit interval of z. N_d is the number of data points in the interval. N_p is the number of fitting parameters. The value of χ^2 is for the best fit. Q is the goodness of fit. In each model $m_i = 0$.

value of irrelevant exponent y is large and its error is roughly the same order of y, By averaging the results of the six models with Q generally larger than 0.2, we have $\nu_n = 1.55 \pm 0.09$ and $z_{pc} = 0.426 \pm 0.011$, which gives $\lambda_{pc} = 1183.8 \pm 0.8$.

In principle, ν_p and ν_n should coincide with each other, for the two MEs in the INM-eigenvalue spectrum belong to the same random matrices. On the other hand, due to the same universality class, the values of ν_p and ν_n should be equal to the critical exponent of the AM in $d = 3$[89][88]. Obtained by accurate numerical studies, the critical exponent of the AM in $d = 3$ is reported to be 1.57 ± 0.02[17]; however, other numerical studies give smaller values[16]. Within numerical errors, our results are generally satisfied with these requirements for ν_p and ν_n.

The correlation length $\xi(z)$ of each ME can be given as $|\chi_r(Z)|^{-\nu}$, where ν is the estimated value of ν_p or ν_n, and the correlation lengths of the two MEs are plotted in Fig.(3.6). The assymetry of the correlation length show that the divergent properties from the two sides of the transition point are different.

One should notice that the I_N data shown in Fig.(3.5a) have been corrected by the equation

$$I_N^{corr} = I_N - L^y \widetilde{f_1}(\chi_r L^{1/\nu}).$$

							Negative branch	
$[z_{\min}, z_{\max}]$	N_d	N_p	n_r	m_r	χ^2	Q	z_{cn}	ν_n
$[0.3125, 0.6875]$	35	6	2	2	41.23	0.066	0.466 ± 0.004	1.61 ± 0.06
$[0.3125, 0.6875]$	35	6	3	1	41.20	0.066	0.466 ± 0.003	1.57 ± 0.04
$[0.3125, 0.6875]$	35	7	2	3	40.22	0.063	0.468 ± 0.004	1.60 ± 0.04
$[0.3125, 0.6875]$	35	7	3	2	40.46	0.060	0.462 ± 0.008	1.59 ± 0.04
$[0.25, 0.6875]$	40	6	2	2	47.24	0.065	0.464 ± 0.003	1.62 ± 0.02
$[0.25, 0.6875]$	40	6	3	1	46.64	0.073	0.461 ± 0.003	1.62 ± 0.03
$[0.25, 0.6875]$	40	6	2	3	47.21	0.052	0.463 ± 0.004	1.60 ± 0.03
$[0.25, 0.6875]$	40	6	3	2	46.60	0.059	0.461 ± 0.003	1.63 ± 0.02
$[0.3125, 0.75]$	40	6	2	2	45.68	0.087	0.464 ± 0.002	1.56 ± 0.03
$[0.3125, 0.75]$	40	6	3	1	45.37	0.092	0.466 ± 0.003	1.57 ± 0.04
$[0.3125, 0.75]$	40	7	2	3	45.06	0.079	0.466 ± 0.003	1.59 ± 0.04
$[0.3125, 0.75]$	40	7	3	2	45.34	0.075	0.466 ± 0.005	1.58 ± 0.03
$[0.25, 0.75]$	45	6	2	2	52.37	0.075	0.463 ± 0.002	1.62 ± 0.02
$[0.25, 0.75]$	45	6	3	1	52.27	0.076	0.462 ± 0.003	1.62 ± 0.02
$[0.25, 0.75]$	45	7	2	3	52.17	0.063	0.462 ± 0.003	1.60 ± 0.03
$[0.25, 0.75]$	45	7	3	2	52.28	0.061	0.461 ± 0.003	1.62 ± 0.02
average:							0.464 ± 0.003	1.60 ± 0.03

Table 3.3: Fit parameters and estimates for z_c, ν for the negative branch. The error corresponds to 95% confidence intervals. $z_{\min}$ and $z_{\max}$ give the fit interval of z. N_d is the number of data points in the interval. N_p is the number of fitting parameters. The value of χ^2 is for the best fit. Q is the goodness of fit. In each model $n_i = m_i = 0$. There is no irrelevant exponent in the negative branch.
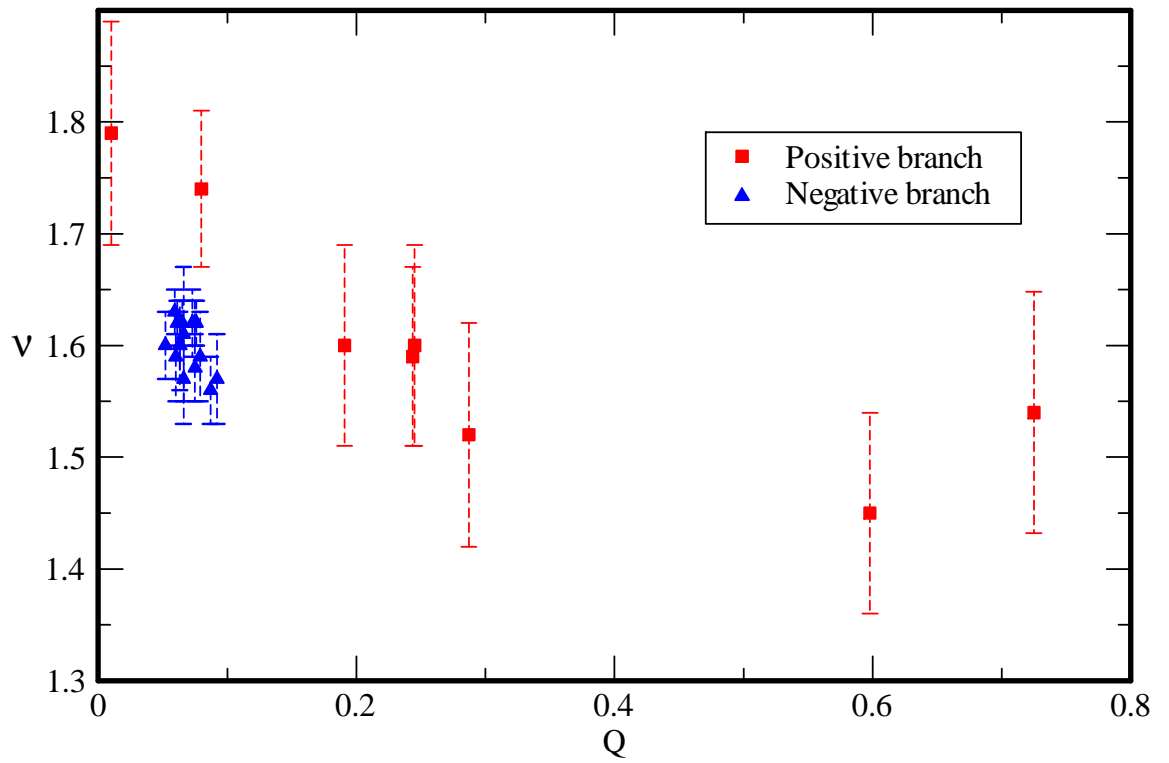
Figure 3.4: Fit values of the critical exponents with 95% confidence intervals as a function of Q. The red squares and black circles are for the models listed in Tables 3.2 and 3.3 for the positive and negative branches, respectively.
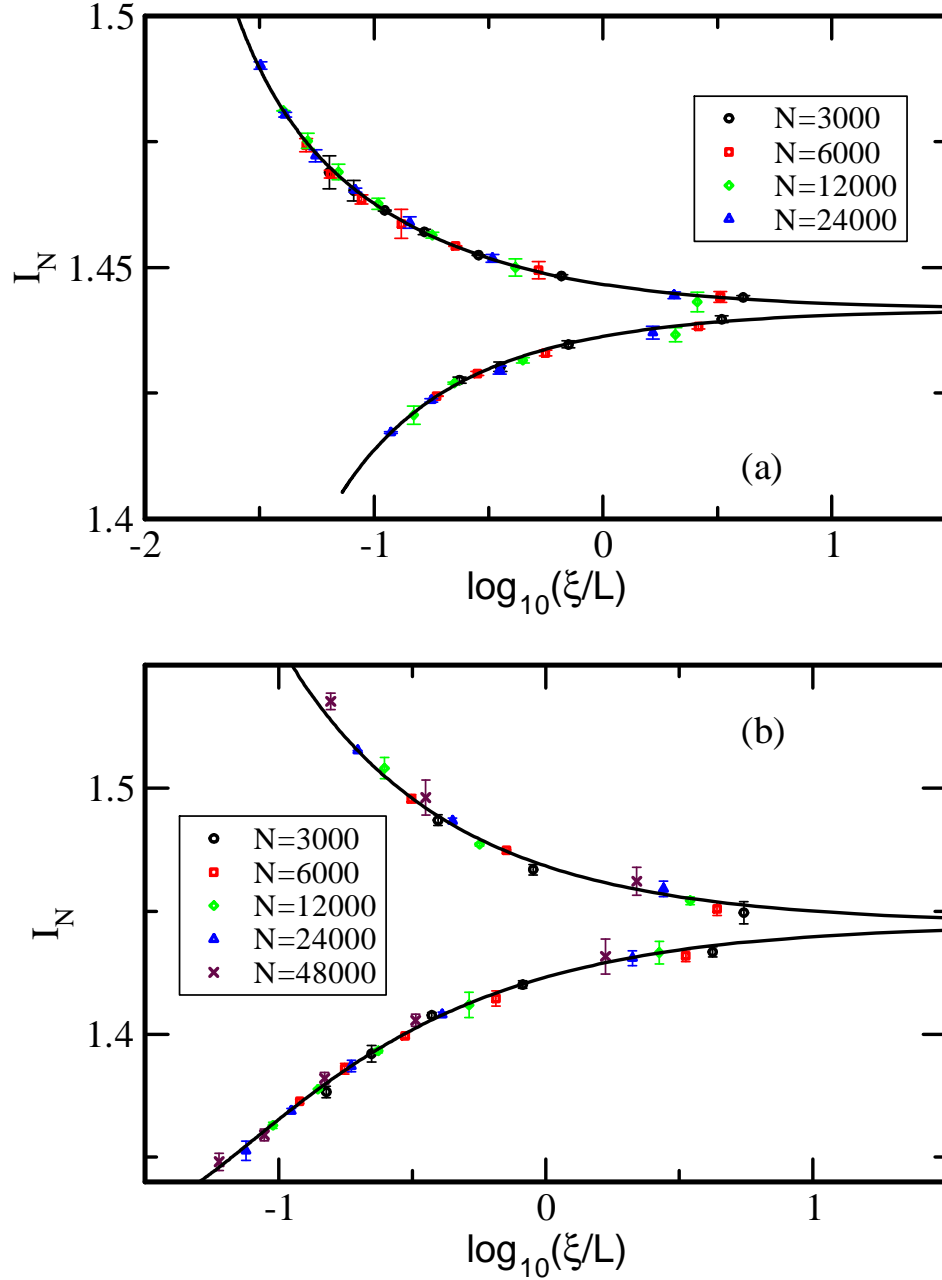
Figure 3.5: Scaling functions of the model (1,0,3,3) for the positive branch (a) and the model (0,0,2,2) for the negative branch (b). The symbols are the numerical data.
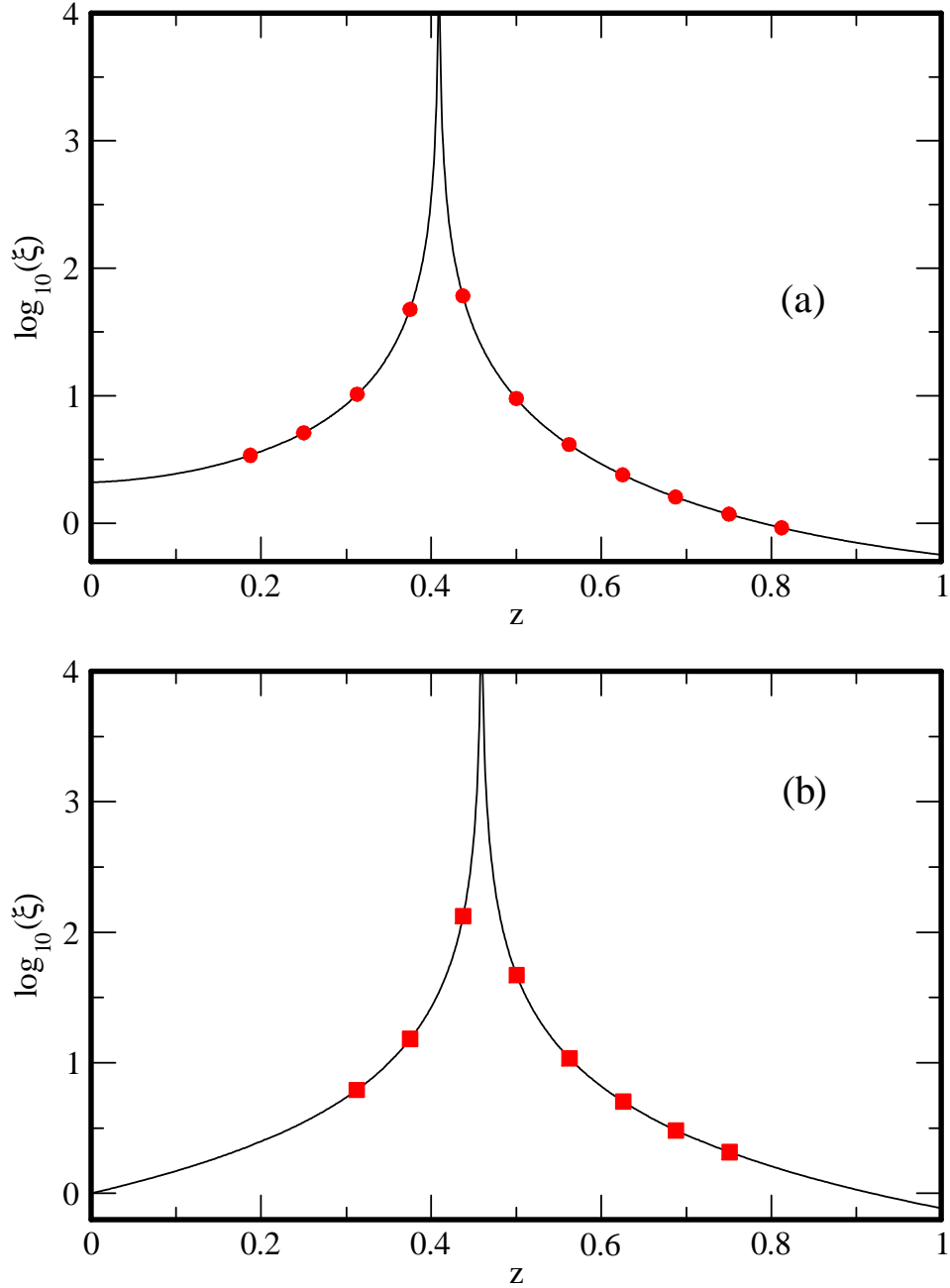
Figure 3.6: Correlation length from the $|\chi_r(z)|^{-\nu}$ of the model (1,0,3,3) for positive branch (a) and the model (0,0,3,1) for the negative branch (b). The symbols indicate the corresponding z value of original numerical data.

The upper and lower curves of the scaling function correspond to the localized and extended INMs, respectively. Thus, we have confirmed the scaling hypothesis for the INMs near each ME and suggest that the MEs in the INM-eigenvalue spectrum should follow the universality for the orthogonal random matrices.

3.3 $P(s)$ at each ME

To examine the critical behavior at the two MEs, we select two narrow intervals $\lambda = 1181.8 - 1185.8$ and $\lambda = -88.1 - -86.1$, which contain the MEs in the positive and negative branches, respectively. For the realizations of each system size, the LSs within the interval in the positive branch is about 8.9×10^5 and that within the interval in the negative branch is 4.1×10^5. Calculated for the four system sizes, the numerical data of the $P(s)$ distributuion within each interval are presented by symbols with error bars in Fig.3.7. Since the widths of the two selected intervals are small enough, the two $P(s)$ distributions, within numerical errors, are generally independent of system size N. We fit the $P(s)$ data of the four system sizes for s less than three by the critical LS distribution of the AM [15],

$$P_c(s) = \frac{A_c^2 s}{\sqrt{\mu^2 + (A_c s)^2}} \exp[\mu - \sqrt{\mu^2 + (A_c s)^2}], \tag{3.4}$$

where A_c and μ are two fitting parameters. The normalized distribution in Eq. (3.4) has a linear behavior at small s with slope $P_c'(0) = A_c^2/\mu$ but changes to a Poisson-type form at large s with a decay rate A_c. Also, the second moment I_c of the distribution is given as $2(\mu + 1)/A_c^2$.

Our results give $A_c = 1.89 \pm 0.02$ and $\mu = 1.565 \pm 0.015$ with the goodness of fit $Q = 0.69$ for the positive branch and $A_c = 1.9 \pm 0.02$ and $\mu = 1.568 \pm 0.020$ with Q close to one for the negative branch, where the errors of the fit parameters are estimated within 95% confidence interval. The numerical results and the fit for large s are shown in the insets of Fig. 3.7. Indicated by the fit data, the $P(s)$ within the two selected intervals almost coincide with each other and the two values of A_c are almost the same as that of the AM[60]. Calculated with the values of A_c and μ, the slope $P_c'(0)$ at $s = 0$ has a value about 2.29, which is comparable with that of the AM with the periodic boundary conditions [61]. Similarly, the second moments I_c

of the two fit distributions are close to 1.43, which is once again very close to the corresponding value of the AM. Thus, we have verified that, within numerical errors, the nearest-neighbor LS distribution near any ME in the INM spectrum of the TLJ fluid agrees the critical $P_c(s)$ distribution obtained from the AM, which supports the universality of the critical nearest-neighbor LS distribution.

3.4 Summary

In this chapter, we have performed the LS analysis for Hessian marices of the TLJ fluid at a thermodynamic state to investigate the properties of the LDT in topologically disordered systems, which have no reference frame of lattice. The Hessian matrices evaluated at the fluid configuations are an ensemble of Euclidean random matrices with elements subject to several constrants, and the matrices are sparse due to the short-range nature of the TLJ potential. By referring the eigenmodes of the matrices as the INMs, the eigenvalue spectrum of the INMs is composed of two branches corresponding to the positive and negative eigenvalues.

Calculated for several system sizes of the TLJ fluid and averaged for very large amounts of fluid configurations, the second moments of the nearest-neighbor LS distributions of the INMs within some small intervals in each branch are found to follow the scaling behavior near a LDT. In terms of the size invarince of the second moments, two LDTs, refered as the MEs, are confirmed to exist in the INM-eigenvalue spectrum, with one in the positive branch and the other in the negative branch. We have used the finite-size scaling to estimate the locations and the critical exponents of the two MEs. In the models to fit the data of the second moments, the nonlinear dependence of the scaling variable on the eigenvalue has been condisdered and an irrelevant scaling variable due to the finite-size effect is introduced in some models for the positive branch. In principle, the critical exponents of the two MEs should coincide in value; through the fitting, their values are found to be 1.55 ± 0.09 and 1.60 ± 0.03 for the positive and negative branches, respectively. Within numerical errors, the estimated values of the two critical exponents are almost coincident with each other and compatible with that of the AM in three dimensions [17]. The nearest-neighbor LS distributions at the two MEs are examined to be almost the same as the

Figure 3.7: The nearest-neihbor LS distribution near the ME in the positive branch (a) or in the negative branch (b).

critical LS distribution obtained from the AM. Thus, we conclude that the MEs in the eigenvalue spectra of Hessian matrices of topologically disordered systems follow the universality for the othogonal universality class and have nothing to do with the topological nature of the disorder in the systems and the constraints imposed on the Hessian matrices due to structural considerations.

Chapter 4

The Analysis of Level-Number Variance

In the previous chapter, we have presented the details of the nearest-neighbor LS analysis, which characterizes the correlation of the nearest-neighbor energy levels. In addition to the nearest-neighbor LS distribution, another related quantity called *the level-number variance* (LNV), which characterizes the correlation beyond the nearest-neighbor energy levels, is also widely studied. The LNV is defined as

$$\langle (\delta n(\Delta E))^2 \rangle = \langle [n(\Delta E) - \langle n(\Delta E) \rangle]^2 \rangle, \tag{4.1}$$

where $n(\Delta E)$ is the number of energy levels within an selected energy interval ΔE and $\langle ... \rangle$ denotes the ensemble average over the INMs. In the localization regime, the correlation of levels is absent, therefore, the LNV is of the order $\langle n \rangle$. On the other hand, Dyson proposed that the LNV for the GOE, in which eigenvectors behave fully extended nature, follows a logarithmic behavior [58]

$$\langle (\delta n)^2 \rangle = \frac{2}{\pi^2} [\ln \langle n \rangle + C], \quad 1 \ll \langle n \rangle \ll \hbar D / L^2, \tag{4.2}$$

where D is diffusion constant, and the constant $C \approx 2.8$. As a one-dimensional gas, the levels are compressible in the localized regime but are almost imcompressible in the delocalized rigime. To quantify such concept, an important parameter is defined as *the level compressibility* (LCP)

$$\chi = \lim_{\langle n \rangle \to \infty} \lim_{N \to \infty} \frac{d \langle (\delta n)^2 \rangle}{d \langle n \rangle}, \tag{4.3}$$

where the value of χ is between 0 and 1, corresponding to the fully extended and the completely localized regimes, respectively [67]. The LCP characterizes the correlation of energy levels at the LDT on scales much larger than the mean level spacing[65]. At the LDT of the AM, it is purposed that *the LCP* is an universal quantity [60][61] and strongly depends on the dimensionality of the system [64] The value $\chi \approx 0.27$ was reported for the AM of system size up to $L = 32$ [60]. For different boundary conditions, at the large $\langle n \rangle$ limit, $\langle n \rangle \sim 10^3$, the same value $\chi \approx 0.27 \pm 0.02$ for the AM was estimated [61]. For anisotropic AM with only 10% coupling constant in z axis, by the FFS of the LNV, the value $\chi = 0.28 \pm 0.06$ was reported [67].

On the other hand, a scaling relation is purposed for the multifractal waves

$$\chi = \frac{(d - D_2)}{2d}, \tag{4.4}$$

where χ is the LCP and $d - D_2$ is the multifractal exponent[65]. The multifractality has been observed in many ciritcal systems and will be discussed in the next chapter.

Simliar to the second moment of the nearest-neighbor LS distribution, the integrated LNV for a disorder region was proposed

$$\eta(N, W) = \frac{1}{L_0} \int_0^{L_0} (\delta n)^2 dL,$$

where $L = \langle n \rangle$, L_0 is some cut-off value of $\langle n \rangle$ and W is the disorder of the anisotropic AM [67]. According to the FFS of the integrated LNV, the location of the ME and the critical exponent of correlation length was determined.

In this chapter, we calculate the LNV for different eigenvalue regions near in INM spectrum. Due to the nature of LCP beyond the correlation of nearest-neighbor energy levels, the calculation of the LCP requires a large amount of levles within a selected region in the INM spectrum. For a system of finite size, the number of levels within a selected energy reigon depends on system size. Therefore, the required number of calculating levels is much larger than that in the analysis of LS statistics and our calculation is strongly restricted by the computer power. The restriction does not appear in the AM, because that the states at the critical have the same multifractal nature close to the band center. Furthermore, the FFS for the integrated LNV provides an alternative to locate the ME and to extract the value of correlation length exponent in INM spectrum. We are going to verify whether the relation of Eq.(4.4) is valid in the INM spectrum in this chapter.

4.1 Level compressibility

Similar to the LS analysis, in order to perform the LNV analysis and extract the value of LCP, the unfolded eigenvalues are divided to several regions, which characterize different degrees of localization. Each region should not be too small, which reduces $\langle n \rangle$ in a finite system; yet it should not be too large, which cause the mixing of different degrees of localization. All of the data sets used in this LNV analysis is the same as those in the chapter three, which list in the table 3.1 for $\lambda = 1150 \sim 1180$ and $\lambda = -95 \sim -80$.

Four sections of unfolded eigenvalues $z = 0.2$, 0.4, 0.6 and 0.8 with $\Delta z = 0.2$ are selected, and the LNV in each section are calculated up to $\langle n \rangle_{cut} = 18$. Fig. 4.1 shows $\langle (\delta n)^2 \rangle / \langle n \rangle$ with respect to $\langle n \rangle$, and different symbols, black circle, red square, green diamond and blue triangle, correspond to $z = 0.2 \pm 0.1$ to 0.8 ± 0.1. The dash line indicates the Dyson's result of Eq.(4.2). The symbol size denotes the system size: the largest ones in (a) and in (b) are $N = 24000$ for the positive branch and $N = 48000$ for the negative branch, respectively, while the smallest ones in both (a) and (b) is $N = 3000$. Near the extended regime, for $z = 0.2$ and $z = 0.8$ in the Fig. 4.1(a) and (b), respectively, the larger the system size, the closer to the Dyson's results the data show. On the other hand, near the localized regime for Fig. 4.1(a) $z = 0.8 \pm 0.1$ and (b) $z = 0.2 \pm 0.1$, the data of the larger size are close to the Possion behavior $\langle (\delta n)^2 \rangle / \langle n \rangle \to 1$. It can be seen that between $z = 0.4 \pm 0.1$ and 0.6 ± 0.1 the dependence of $\langle (\delta n)^2 \rangle / \langle n \rangle$ with the system size flips. Therefore, there should be a system-size invariance between $z = 0.4 \pm 0.1$ and 0.6 ± 0.1.

It has been shown that $\langle (\delta n)^2 \rangle / \langle n \rangle$ at the LDT in AM depends on boundary conditions at small $\langle n \rangle$[61], and in the limit of $\langle n \rangle \to \infty$, the LCP is an universal quantity[60][61]. Fig. 4.2 shows the comparison between three kinds of models at the ME: isotropic AM, anisotropic AM with only 10% coupling constant in z axis[67] and INMs in a fluid with short-range interactions. According to the FSS of the nearest-neighbor LS statistics, the mobility edge of unfolded eigenvalues were selected within $z = 0.425 \pm 0.05$ in the positve branch and $z = 0.462 \pm 0.08$ in the negative branch of the INM spectrum. In our calculation, the largest system size $N = 48000$ gives $\chi \approx 0.35 \pm 0.08$. However, due to the maximum $\langle n \rangle$ of our data is still far away from
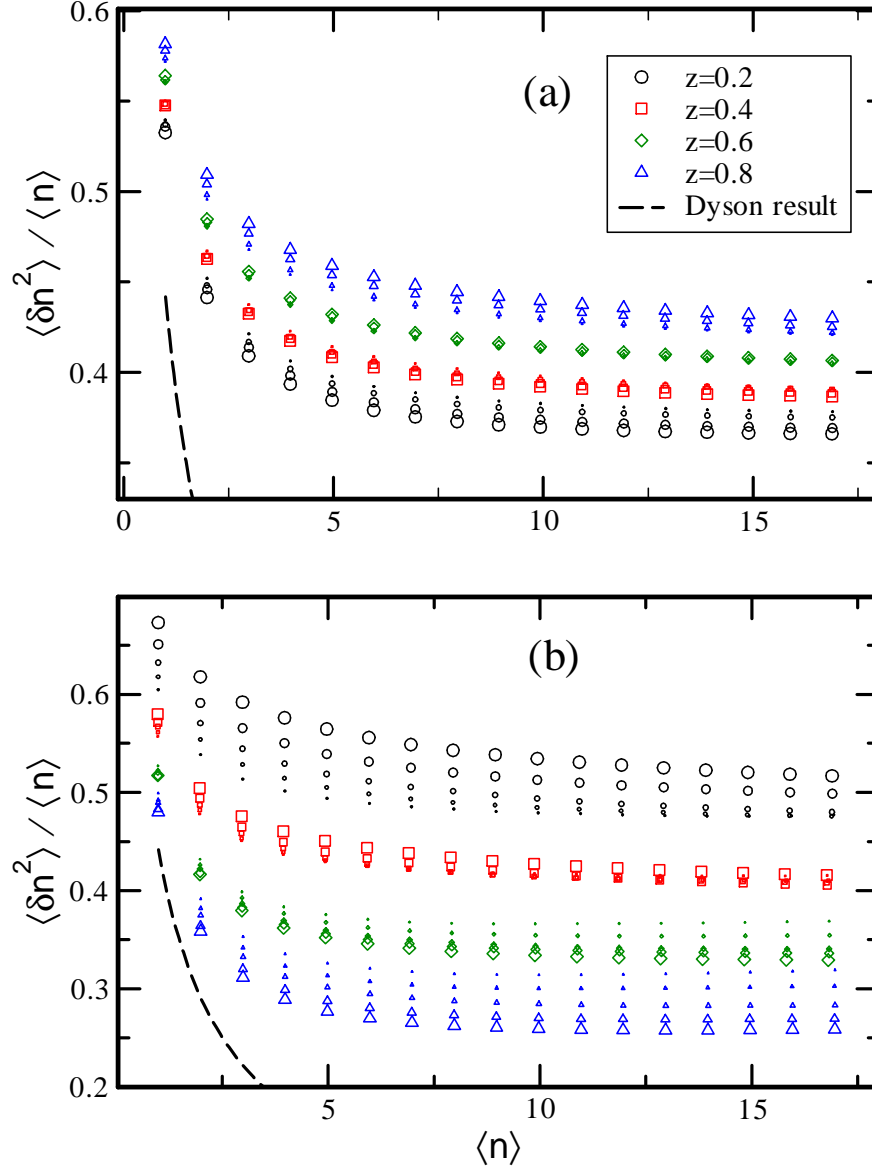
Figure 4.1: The variation of $\langle (\delta n)^2 \rangle / \langle n \rangle$ with respect to $\langle n \rangle$ for several eigenvalue regions. The data of $z = 0.2$, 0.4, 0.6 and 0.8 are denoted by black circles, red squares, green diamonds and blue triangles, respectively. The dash line indicates Dyson's result. The symbols with sizes from small to large denote the system sizes from $N = 3,000$ to $24,000$(a) or $48,000$(b). The upper and lower figures indicate the results for the postive and negative branches in the INM spectrum, respectively.
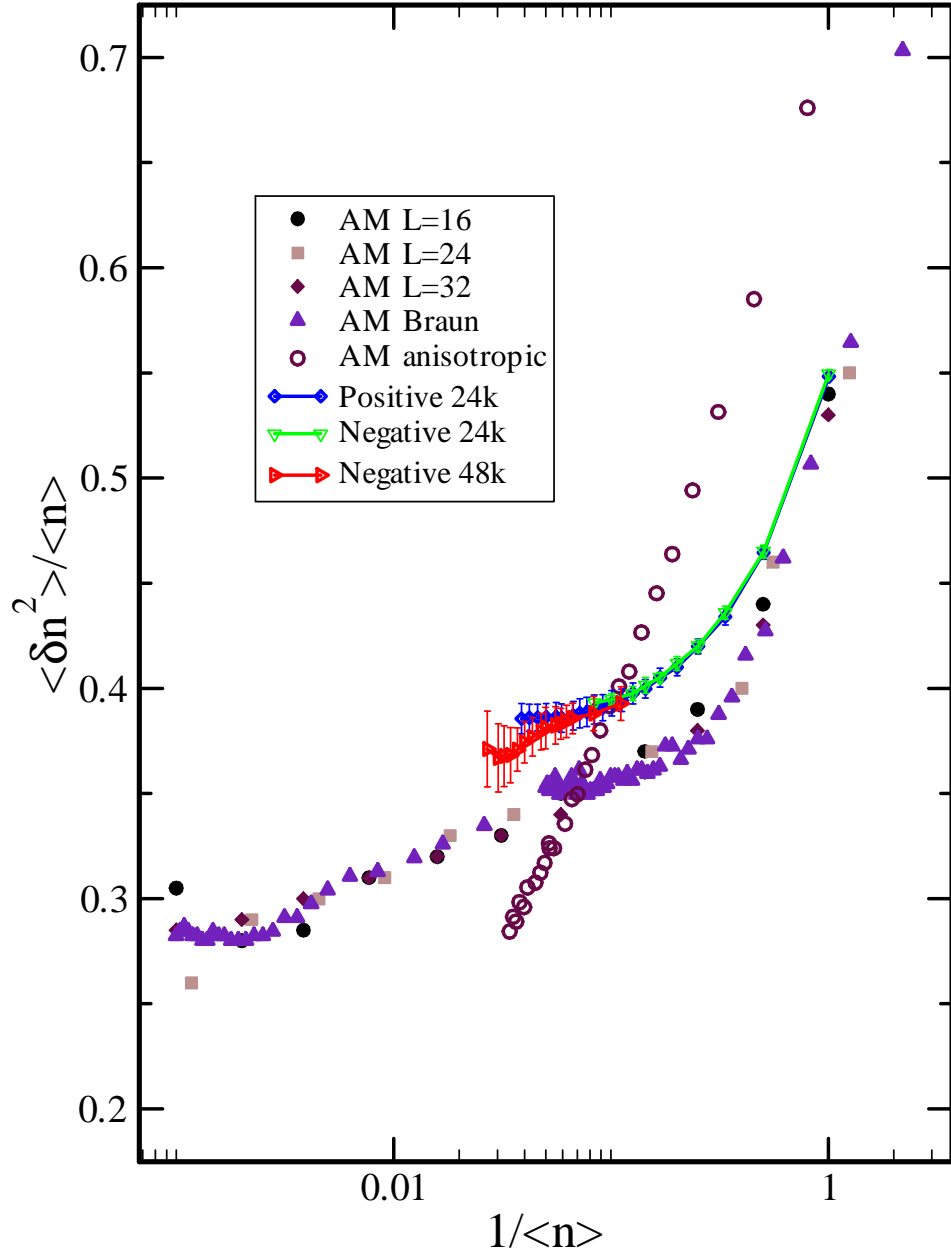
Figure 4.2: Comparison of $\langle(\delta n)^2\rangle/\langle n\rangle$ among different models. The first four sets of data with solid symbols denote results of the isotropic AM[60] and the solid triangles are from Braun and coworkers[61]. The open circles denote the results of the anisotropic AM[67]. The blue dimonds, green triangles down, red triangles right with error bars, denote the data of our model at the LDT for $N = 24,000$ in the positive branch, and $N = 24,000$ and $N = 48,000$ in the negative branch, respectively.

$\langle n \rangle \to \infty$ and the large error bars cause the accurate estimation for the trendency of $\langle (\delta n)^2 \rangle / \langle n \rangle$ more difficult. From the decreasing tendency of $\langle (\delta n)^2 \rangle / \langle n \rangle$, the concluson for the value χ at the ME of the INM spectrum should be lower than 0.35 ± 0.08.

4.2 FSS for integrated LNV

The size dependence of the LNV also servers a condition to locate the ME and to determine the critical exponent ν by the FSS. We follow reference [67] to define *the integrated LNV*

$$\eta(N, z) = \frac{1}{L_0} \int_0^{L_0} (\delta n)^2 dL, \tag{4.5}$$

where $L = \langle n \rangle$. The maximum $\langle n \rangle$ is chosen to be $L_0 = 3$, and all unfolded eigenvalues are divided to nine regions from $z = 0.05$ to 0.85 with $\Delta z = 1.0$. Fig 4.3 shows that the integrated LNV with respect to z in both positive and negative branches of the INM spectrum.

In addition to previous chapter, the data of system size $N = 1,500$ is included, which shows strongly the finite size effect. It can be seen that the cross points shift systematically with the system size and, therefore, the irrelevant variable is necessary in our FSS analysis. As shown in table 4.1, for the positive branch the ME is at $z_c = 0.44 \pm 0.07$ and the critical exponent is $\nu_p = 1.43 \pm 0.21$. On the other hand, for the negative branch the ME is at $z_c = 0.54 \pm 0.03$ and $\nu_n = 1.48 \pm 0.17$. Comparing with the LS results [79], the ME z_c determined by η is slightly higher. Due to the small system sizes and the irrelevant scaling variable, the critical exponent ν is smaller than the LS results yet within acceptable errors. The FSS gives the irrelevant variable $y = -2.39 \pm 1.67$ for the positive branch and $y = -2.45 \pm 0.58$ for the negative branch that agrees with the suggestion that the irrelevant variable y should be an universal variable[17]. As the previous chapter, we can rescale the horizontal axis of Fig 4.3 by diveding $\xi(z)$ and subtracting the corrections due to the irrelevant scaling variable. The rescaling function is corrected as

$$\eta_{corr} = \eta - L^y \cdot \widetilde{f}_1 \left(\chi_r L^{1/\nu} \right). \tag{4.6}$$

Fig 4.4 reveals that the data collapse onto a single scaling function η_{corr}.

4.3　Summary

Because the number of discrete levels within a selected eigenvalue range is finite, the maximum $\langle n \rangle$ in our system is the order of 10, which is still far away from ∞. The realistic situation suppresses the accuracy for the estimation of χ. If we extend the selected eigenvalue range to get more discrete levels, the data suffers the mixing of different nature of energy levels and we get ambiguous results. The only way to solve the problem is to calculate with large system sizes as large as possible. For the Anderson model, at critical disorder $W = 16.5$, the examination can be done much easily by getting more levels up to the number of 10^3, since the eigenfunctions have the same critical properties.

We have calculated the LNV for eigenvalues near the LDT with respect to different system sizes. Quantitatively, the LCP should be lower than $\chi \approx 0.35 \pm 0.08$. Suffering from not enough levels in the selected regime and the mixing of eigenstates with different natures, it is difficult to determine the LCP and verify the scaling relation of Eq.(4.4) by our model. On the other hand, the FSS gives the positions of the MEs and the correlation length exponents $\nu_p = 1.43 \pm 0.21$ and $\nu_n = 1.48 \pm 0.17$, which generally agree with the previous results.

Table 4.1: The fitting results of η with the integral range up to $L_0 = 3$. For all models, the irrelevant variable is included. N_d is the number of data points, N_p is number of parameters, and Q is the goodness of fitting. The estimated errors in the parentheses correspond to 95 confident interval.

$[z_{\min}, z_{\max}]$	N_d	N_p	n_r	m_r	z_c	ν_p	y_s	Q
Positive branch								
$[0.15,0.75]$	35	9	1	3	0.44(7)	1.43(14)	-2.39(1.46)	0.13
$[0.05,0.85]$	45	9	1	3	0.44(5)	1.43(32)	-2.39(1.83)	0.56
$[0.05,0.85]$	45	10	2	2	0.45(4)	1.42(20)	-2.55(1.66)	0.39
$[0.05,0.85]$	45	11	2	3	0.43(4)	1.36(13)	-1.84(1.77)	0.38
$[0.05,0.85]$	45	11	3	1	0.45(6)	1.48(27)	-2.68(1.63)	0.38
average					0.44(5)	1.43(21)	-2.37(1.67)	
Negative branch						ν_n		
$[0.25,0.65]$	30	11	3	1	0.53(7)	1.48(37)	-2.42(1.00)	0.02
$[0.25,0.65]$	30	13	3	3	0.54(2)	1.53(16)	-2.26(66)	0.02
$[0.25,0.65]$	30	12	3	2	0.55(2)	1.46(25)	-2.25(98)	0.02
$[0.05,0.85]$	54	12	3	2	0.54(1)	1.47(5)	-2.70(53)	0.04
$[0.05,0.85]$	54	13	3	3	0.53(1)	1.47(4)	-2.64(70)	0.03
average:					0.54(3)	1.48(17)	-2.45(58)	
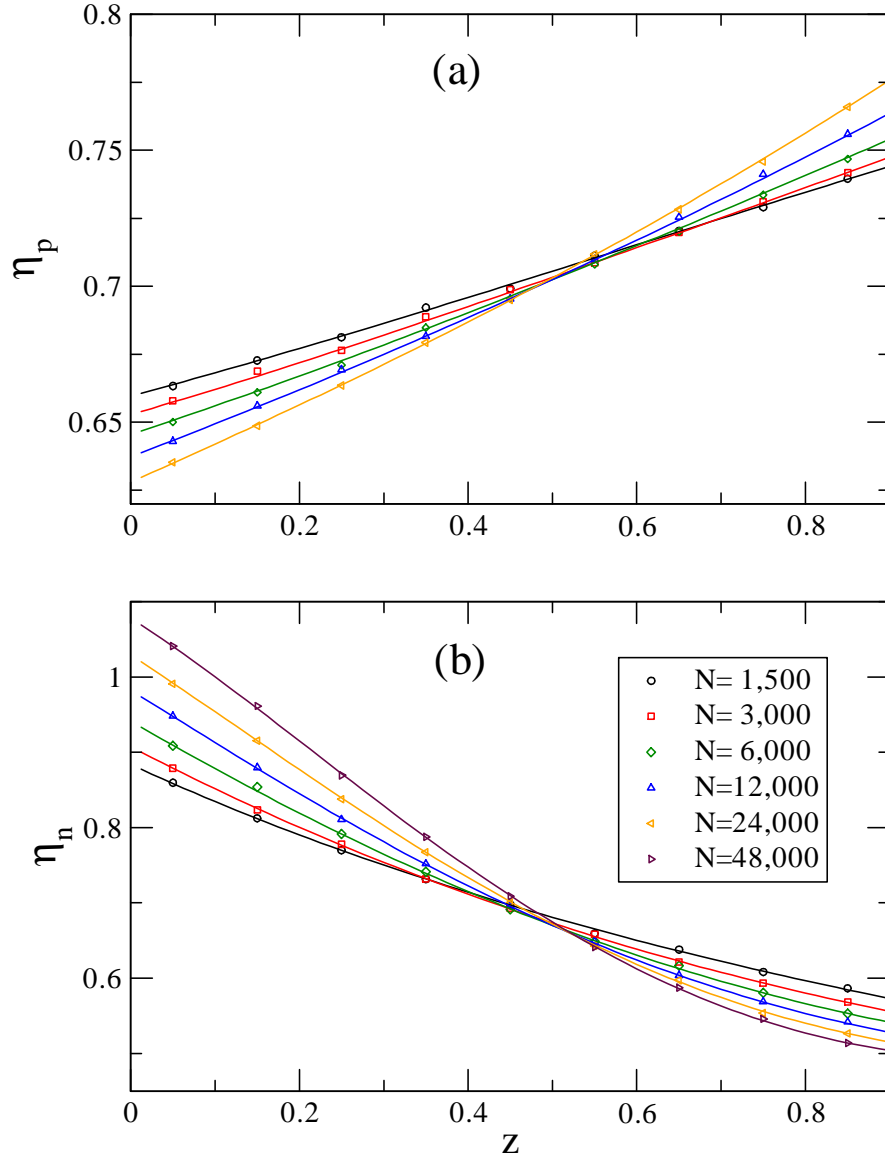
Figure 4.3: Integrated level-number variance of postive branch λ from 1150 to 1230 (a) and negative branch λ from -95 to -80 (b). The abscissas axis denote unfolded eigenvalue z. The symbols are numerical data and the solid lines are the fitting of function with (1,0,3,1) model in the positive branch and (1,0,3,2) model in the negative branch.
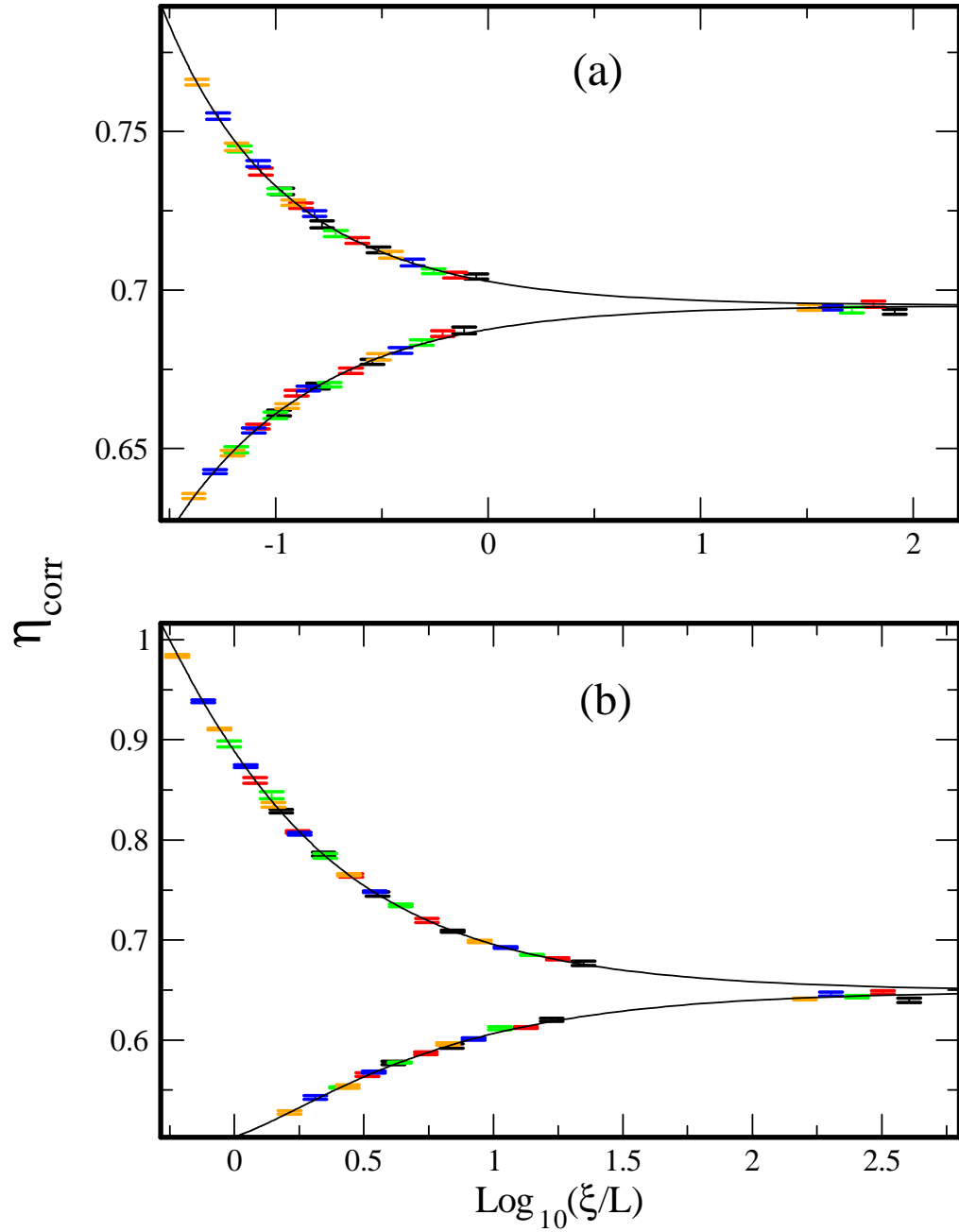
Figure 4.4: The rescaling function η for the positive branch (a) and the negative branch (b). The data have been corrected according to Eq.(4.6).

Chapter 5

The Multifractal Analysis

One of the representations of the multifractal analysis (MFA) reveal as a set of *general dimensions* D_q, which describe the scaling relation between the summation of the q-th moment squared vibrational amplitudes $|\psi_i|^2$ with the size of system (or the size of measuring box). Beyond a single fractal dimension, such general fractal dimensions show non-linear behavior with respect to q which characterize different orders of the squared vibrational amplitudes. Moreover, it was purposed that the general dimensions are related with a hierarchy of exponents α by a Legendre transform[36][37][38].

Focus on the exponents α, supposing that the squared vibrational amplitudes $|\psi_i|^2$ scale with system size as

$$|\psi_i|^2 \sim L^{-\alpha}. \tag{5.1}$$

Define the singularity strength $\alpha = -\ln |\psi_i|^2 / \ln L$, which characterizes the magnitudes of squared vibrational amplitudes. The number of particles belong to $[\alpha, \alpha + d\alpha]$ is ΔN_α, which scales as

$$\Delta N_\alpha \sim L^{f(\alpha)}, \tag{5.2}$$

where $f(\alpha)$ denotes the fractal dimensions of the set of points belonging to $[\alpha, \alpha + d\alpha]$. The function $f(\alpha)$ is called *the singularity spectrum* (SSP). Generally, $f(\alpha)$ is a convex function with the maximum at $\alpha = \alpha_0$ equal to the space dimension of the system and the values of SSP depends on system size and the magnitude of disorder (or frequencies). Another feature point in $f(\alpha)$ is the one where $f(\alpha_1) = \alpha_1$, so that the slope of $f(\alpha)$ at α_1 is one[95]. Near the completely localized region, because that

the eigenvector is characterized by a few compoents of the zero order of L and all other compoents of the order of $L^{-\infty}$, the SSP approaches $f(0) = 0$ and $f(\infty) = 3$. On the other hand, near the fully extended region, the uniform eigenvectors with $|\psi_i|^2 = L^{-3}$ reveal that the spectrum reaches $f(3) = 3$. Due to the finite-size effect, for extended region the larger size rsults in a narrower $f(\alpha)$ curve, while a widening one for localized state[96]. The SSP at ME turns out to be invariant with respect to system size in 3D Anderson model[42][96]. Suppose that this is also true in 3D vibrational system, then this property can be used to determine the mobility edge.

Since 1991, the SSP has been used to characterize the MIT in the Anderson model [69]. Using different disorder distribution, the SSP at ME is invarint for system size, therefore, it was argued that the critical SSP is universal and not dependent on energy or disorder [42]. This property serves as a condition to locate the LDT in the AM [96] and vibraional systems [95]. Despite the results support that the universality of SSP exist, there are still some problems: First, to claim the universality of the SSP, the precision of previous numerical work is not convincing. Second, the fluctuation of waves near the ME is strong, how to deal with the fluctuations between different waves? Recently, the roles of typical average and ensemble average were carefully compared by Römer and coworkers[86][87], and accompany with easier access computer power and more efficient algorithm, the precision of the SSP at the LDT of the AM was highly improved. Building on these milestons, we try to locate the LDT in the INMs by the MFA, and further verify the universality of the SSP at LDT in the INMs and in the AM.

By mean of the LS statistics, the ME were determined in both branches of the INM spectrum, where the eigenvalue interval is $\lambda_{pc} = 1183.8 \pm 0.8$ for the positive branch. By the multifractal analysis given later, the MEs in the negative branch is found at $\lambda_{nc} = -86.6 \pm 0.5$, which, within numerical errors, almost agrees with that obtained by the LS statistics[79][80]. Near these regions, the INMs have been calculated by diagonalizing Hessian matrices with the JADAMILU package. Generally, the geometric structure of an INM eigenvector can be represented by the spatial distribution of the vibrational amplitudes. Figure 5.1(a) and (b) shows a 3-D visulization of the vibrational amplitudes of two INMs at the ME for $N = 96000$, and only the components for $|\psi_i|^2 > N^{-1/2}$ (corresponding to $\alpha < 3$) are shown.
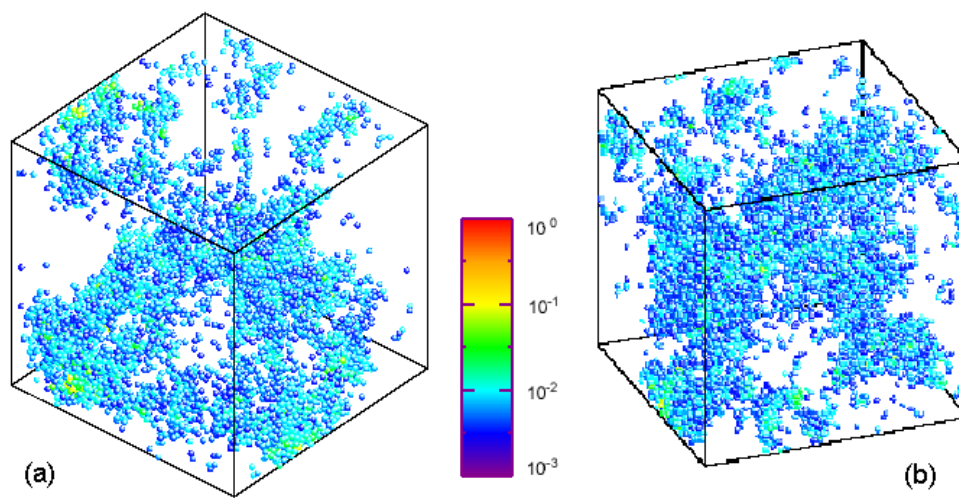
Figure 5.1: Geometric structures of the INMs with $\lambda = 1183.25$ (a) and -86.78 (b) for the TLJ fluid of 96000 particles in a box of length $L = 46.22$. In each panel, particles with vibrational amplitudes $|\psi_i|$ larger than the average value $N^{-1/2}$ are shown by spheres with diameter of one and centered at the particle position. The color of each sphere specifies the $|\psi_i|$ value of the corresponding particle in the INM. The total numbers of spheres shown in (a) and (b) are about 5700 and 7000, respectively.

5.1 Fractal Dimension and Singularity Spectrum

Here we introduce the general dimensions of the multifractal structure. Suppose there are N particles and the corresponding components $|\psi_i\rangle$ of a INM $|\psi\rangle$ in a system with box size L, is denoted as

$$|\psi\rangle = \sum_{i=1}^{N} |\psi_i\rangle = \sum_{i=1}^{N} \left[\sum_{\nu=1}^{3} |e_{i\nu}\rangle \right],$$

where i and ν are the index of particle and the Cartesian coordinate, respectively, $|\psi_i\rangle$ is the vibrational amplitude on the particles i of a INM and the vector $|\psi_i\rangle$ consists of three basis vector $|e_{i\nu}\rangle$ along the Cartesian coordinate. The fluctuations of eigenvectors can be characterized by a set of *inverse participation ratio (IPR)* defined as sum over the q-th moment of squared vibrational amplitudes $|\psi_i|^2$,

$$P_q = \sum_{i=1}^{N} \left[|\psi_i|^2 \right]^q = \sum_{i=1}^{N} \left[\sum_{\nu=1}^{3} \langle e_{i\nu} | e_{i\nu} \rangle \right]^q. \tag{5.3}$$

Underlying the assumption of multifractality, which, in principle, has no relevant length scale, P_q is assumed to follow the power-law behavior

$$P_q \propto L^{-\tau_q}, \tag{5.4}$$

where the mass exponent τ_q is a quantity characterizing the nature of the INMs under investigation. Furthermore, one should carefully distinguish the q-th moment dependence from τ_q. Provided that measures are uniformly distributed with space dimenison d, the q-th moment of $|\psi_i|^2$ should distribute with dimension d independent of q. Using the normalization condition $\sum_{i=1}^{N} |\psi_i|^2 = 1$, we have $|\psi_i|^2 = L^{-d}$ and the $\sum_{i=1}^{N} \sim L^d$. Therefore,

$$\begin{aligned} P_q &\propto L^d \cdot \left[L^{-d} \right]^q \\ &= L^{-d(q-1)}. \end{aligned}$$

The mass exponent τ_q is $d(q-1)$ for the fully delocalized INMs, and τ_q equals to zero for the completely localized INMs. From this argument, the appropriate definition

of the fractal dimension of the q-th moment of the squared vibrational amplitudes should be

$$D_q = \frac{\tau_q}{q - 1},$$

where D_q is so-called generalized fractal dimensions[31]. The value of D_q is less or larger than d for positive or negative q, respectively. Also, D_q depends only on the universality class so that D_q should be the same for the two MEs in INM spectrum.

There are two scenarios to extract the mass exponent τ_q and corresponding fractal dimensions D_q: the system-size scaling and the box-size scaling. For the system-size scaling, it needs to calculate the q-th moment of squared vibrational amplitudes for different system size, and the calculations are more expansive. For the box-size scaling, it is a coarse-grain procedure intrinsicly. Here we consider the box-size scaling by *the box-counting method*. All $|\psi_i\rangle$ are divided into N_η small boxes with size l, where $N_\eta = (\frac{L}{l})^3 = (\frac{1}{\eta})^3$ with $\eta \equiv \frac{l}{L}$. The coarse-gained squared vibrational amplitudes are defined as *the local probability density μ_k* (LPD), which is the sum over all components $|\psi_i|^2$ within box k,

$$\mu_k = \sum_{i \in box\ k} |\psi_i|^2. \tag{5.5}$$

Consequently, we define *the general Inverse Participation Ratio (gIPR) P_q* as summation over the q-th moment of LPD μ_k,

$$P_q(\eta) = \sum_{k=1}^{N_\eta} (\mu_k)^q. \tag{5.6}$$

Because the strongly fluctuation of individual INM at ME, a proper average for the scaling-law of gIPR must be taken[86][87]. Generally, there are two kinds of the average of $P_q(\eta)$: the ensemble average and the typical average, which are defined as

$$\langle P_q(\eta) \rangle_\lambda \quad \propto \quad \eta^{\tau_q^{ens}}, \tag{5.7}$$

$$e^{<\ln P_q(\eta)>_\lambda} \quad \propto \quad \eta^{\tau_q^{typ}}, \tag{5.8}$$

where $\langle ... \rangle_\lambda$ denotes the arithmetic average over all the INMs with eigenvalues within a small window of width $\Delta\lambda$ and centered at λ, and τ_q^{ens} and τ_q^{typ} denote the mass exponents with ensemble average and typical average, respectively. For a very broad distribution, the typical average of $P_q(\eta)$, which is the geometric mean, provides more

intrinsic information about the distribution than the arithmetic mean. Here, we take the typical average, from the scaling relation of Eq.(5.8), the mass exponents τ_q^{typ} is given as

$$\tau_q^{typ} = \lim_{\eta \to 0} \frac{\langle \ln P_q(\eta) \rangle_\lambda}{\ln \eta}. \tag{5.9}$$

Another representation of the multifractality is the singularity spectrum $f(\alpha)$. Generally, there are two methods to calculate the SSP. First, the SSP can be obtained from the mass exponents τ_q via a Legendre transformation [33][38],

$$f_q = f(\alpha_q) = \alpha_q q - \tau_q, \tag{5.10}$$

where

$$\alpha_q = \frac{d\tau_q}{dq} \quad \text{and} \quad q = \frac{df(\alpha)}{d\alpha} \tag{5.11}$$

The underline physics of the Legendre tranform can be understood by the probality density function of singularity strength α, and the detail derivation can be seen in Appendix A.2. Second, the SSP can be directly obtaind from the probability density funciton (PDF) of singularity strength α, which will be discussed in the Sec. 5.3.

Now we take the first approach. Because the decrete numerical points of q introduce numerical errors for the derivative of τ_q with respect to q. To avoid such numerical errors, the Legendre transformation is translated into the scaling form. Substitute Eq.(5.9) to Eq.(5.11-5.10), after carefully derivative on q, we have

$$\alpha_q^{typ} = \lim_{\eta \to 0} \frac{1}{\ln \eta} \left\langle \sum_{k=1}^{N_\eta} \delta_k(q, \eta) \ln \delta_k(1, \eta) \right\rangle_\lambda = \lim_{\eta \to 0} \frac{\ln A_q(\lambda, \eta)}{\ln \eta}, \tag{5.12}$$

$$f_q^{typ} = \lim_{\eta \to 0} \frac{1}{\ln \eta} \left\langle \sum_{k=1}^{N_\eta} \delta_k(q, \eta) \ln \delta_k(q, \eta) \right\rangle_\lambda = \lim_{\eta \to 0} \frac{\ln F_q(\lambda, \eta)}{\ln \eta}, \tag{5.13}$$

where $\delta_k(q, \eta) \equiv \mu_k^q(\eta)/P_q(\eta)$. With the Eq.(5.12) and (5.13), the α_q and f_q of certain q can be calculated directly through the scaling formula without introducing numerical errors from decrete q points. The brackets in the right hand side of Eq.(5.12) and (5.13) are defined for the $\ln A_q(\lambda, \eta)$ and $\ln F_q(\lambda, \eta)$.

The thermodynamic limit in Eq.(5.9) is achieved by either $L \to \infty$ or $l \to 0$ but, practically, these two limits can not be obtained in the numerical method. Instead of

taking the limit, the value of τ_q^{typ} is the slope of a linear fit of $\langle \ln P_q(\eta) \rangle_\lambda$ versus $\ln \eta$ within a finite interval of η. Similarly, the values of α_q and f_q in Eqs.(5.12) and (5.13) are obtained by the slope of a linear fit for the $\ln A_q(\lambda, \eta)$ and $\ln F_q(\lambda, \eta)$ versus $\ln \eta$, respectively.

Because the scaling behavior will breakdown for small box l near lattice constant a, the choice of small box size should be $l \gg a$. By averaging 5×10^3 INM eigenvectors of $N = 96000$ at the ME in the negative branch and taking the ratio $L/l = 1/\eta$ in the box-counting method as an integer varied from 2 to 10, we have calculated $\langle \ln P_q(\eta) \rangle_\lambda$, the $\ln A_q(\lambda, \eta)$ and $\ln F(\lambda, \eta)$ for q between -5 and 5. The numerical results of integer q are presented in Fig. 5.2, including the linear fit for the data of each q. Generally, the linear fit is good for the three sets of $\langle \ln P_q(\eta) \rangle_\lambda$, the $\ln A_q(\lambda, \eta)$ and $\ln F_q(\lambda, \eta)$ data. We have performed the same calculations at the positive-eigenvalue ME and the results are almost the same as those shown in Fig. 5.2.

The mass exponent τ_q and the generalized fractal dimension $D_q = \tau_q/(q-1)$ at two MEs are plotted in Fig. 5.3 for $-5 \le q \le 5$. The data in Fig. 5.3 are accurate enough to indicate that τ_q and D_q at the two MEs are identical. At $q = 0$, $\tau_q = -d$ and $D_q = 0$ as expectation. For $q = 2$, D_2 is the correlation dimension of the inverse participation ratio P_2 [46] and our results give $D_2 = 1.38 \pm 0.05$, which is generally consistent with the D_2 value of the AM estimated with several different methods[70][71][73][74]. In principle, as q varies from $-\infty$ to ∞, τ_q is a monotonically increase function, but the slope of the function, which gives the value of α_q, decreases from the limiting value α_+ to α_-. The two limiting values, α_+ and α_-, confine the range of the singularity spectrum $f(\alpha)$ under the typical average[86]. Estimated by our data at $|q| = 5$ in Fig. (5.3a), our calculated $f(\alpha)$ is within the range of α from 0.87 to 6.7.

Presented in the insets of Fig.(5.4) are the values of α_q and f_q generated from the slope of the linear fit for the $\ln A_q(\lambda, \eta)$ and $\ln F_q(\lambda, \eta)$ versus $\ln \eta$ for $-5 \le q \le 5$, respectively. With the data sets of α_q and f_q, the singularity spectra $f(\alpha)$ at two MEs are shown in Fig.(5.4). Within numerical errors, the singularity spectra at the two MEs are generally identical and also agree with the one of the AM[86]. This agreement of $f(\alpha)$ gives another confirmation for the locations of the two MEs in the INM specrum. Obtained by our results, the maximun of $f(\alpha)$ is found at

$\alpha_0 = 4.034 \pm 0.006$ for the positivel branch and $\alpha_0 = 4.049 \pm 0.016$ for the negative branch; within their errors, the two values of α_0 agree with each other.

Around the maximum at α_0, where $f(\alpha_0) = d$, the singularity spectrum can be described by the Wegner's parabolic approximation (PA) [92]

$$f^{PA}(\alpha) = d - \frac{(\alpha - \alpha_0)^2}{4(\alpha_0 - d)}, \tag{5.14}$$

which is ensured to go through the maximum of $f(\alpha)$ and to be tangential to the line $f(\alpha) = \alpha$. As shown in Fig.(5.4), $f(\alpha)$ deviates from the PA as α is close to either α_+ or α_-, and overall shape of $f(\alpha)$ becomes asymmetric about the maximum of $f(\alpha)$.

By substituting $f(\alpha)$ in Eqs. (5.10) and (5.11) with $f^{PA}(\alpha)$, τ_q and D_q under the PA are given as

$$\tau_q^{PA} = -(\alpha_0 - d)q^2 + q\alpha_0 - d, \tag{5.15}$$

$$D_q^{PA} = \frac{\tau_q^{PA}}{q - 1} = -((\alpha_0 - d)q - d), \tag{5.16}$$

where α_0 is the only parameter. By setting $\alpha_0 = 4.04$, τ_q^{PA} and D_q^{PA}, shown in Fig.(5.3), are good for small q.

Relative to the delocalized states, the anomalous dimension of the multifractals is defined as $\Delta_q \equiv \tau_q - d(q - 1)$. Recently, a further step goes in the multifractal theory. Based on the nonlinear σ model [76], an exact-symmetric relation of anomalous exponent is proposed as

$$\Delta_q = \Delta_{1-q}. \tag{5.17}$$

With the symmetric relation of Δ_q, it can be proved that the $f(\alpha)$ value for $\alpha < d$ and that for $\alpha > d$ are transformed with each other via the relation [76]

$$f(2d - \alpha) = f(\alpha) + d - \alpha, \tag{5.18}$$

where α is only defined between 0 and $2d$. The symmetric relation of Δ_q has been confirmed numerically by the power-law random banded matrix model in 1D [76], the symplectic Anderson model in 2D [77] and the orthogonal Anderson model in 3D [86][87], and evidenced experimentally by the ultrasound waves in 2D [98].

We show in Fig.(5.4) the singularity spectrum generated via the symmetric relation in Eq.(5.18). Similar as the AM, $f(\alpha)$ obtained by the INMs is generally satisfied
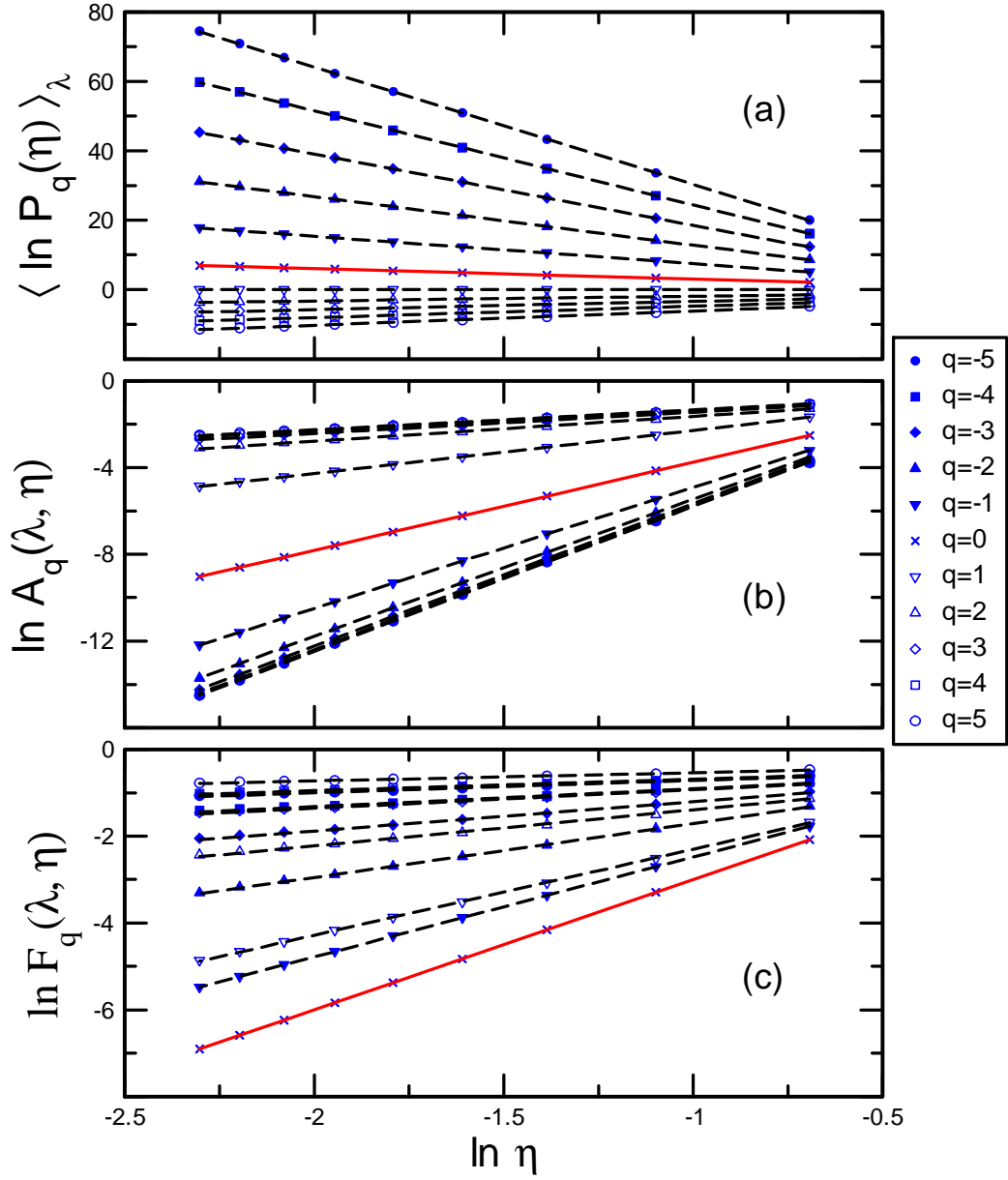
Figure 5.2: Scaling of $\langle \ln P_q(\eta) \rangle_\lambda$ (a), $\ln A_q(\lambda, \eta)$ (b), $\ln F_q(\lambda, \eta)$ (c) versus $\ln \eta$ for the INMs with $\lambda = -86.6 \pm 0.5$. The system size is $N = 96000$ and the values of $1/\eta$ are intergers from 2 to 10. The symbols are the numerical results, with the filled noe for negative q, the open ones for positive q and the crosses for $q = 0$. The errors of the data are smaller than the symbol size. The linear fits for the numerical data of each q are indicated by either the black-dashed lines for $q \neq 0$ or the red-solid line for $q = 0$.
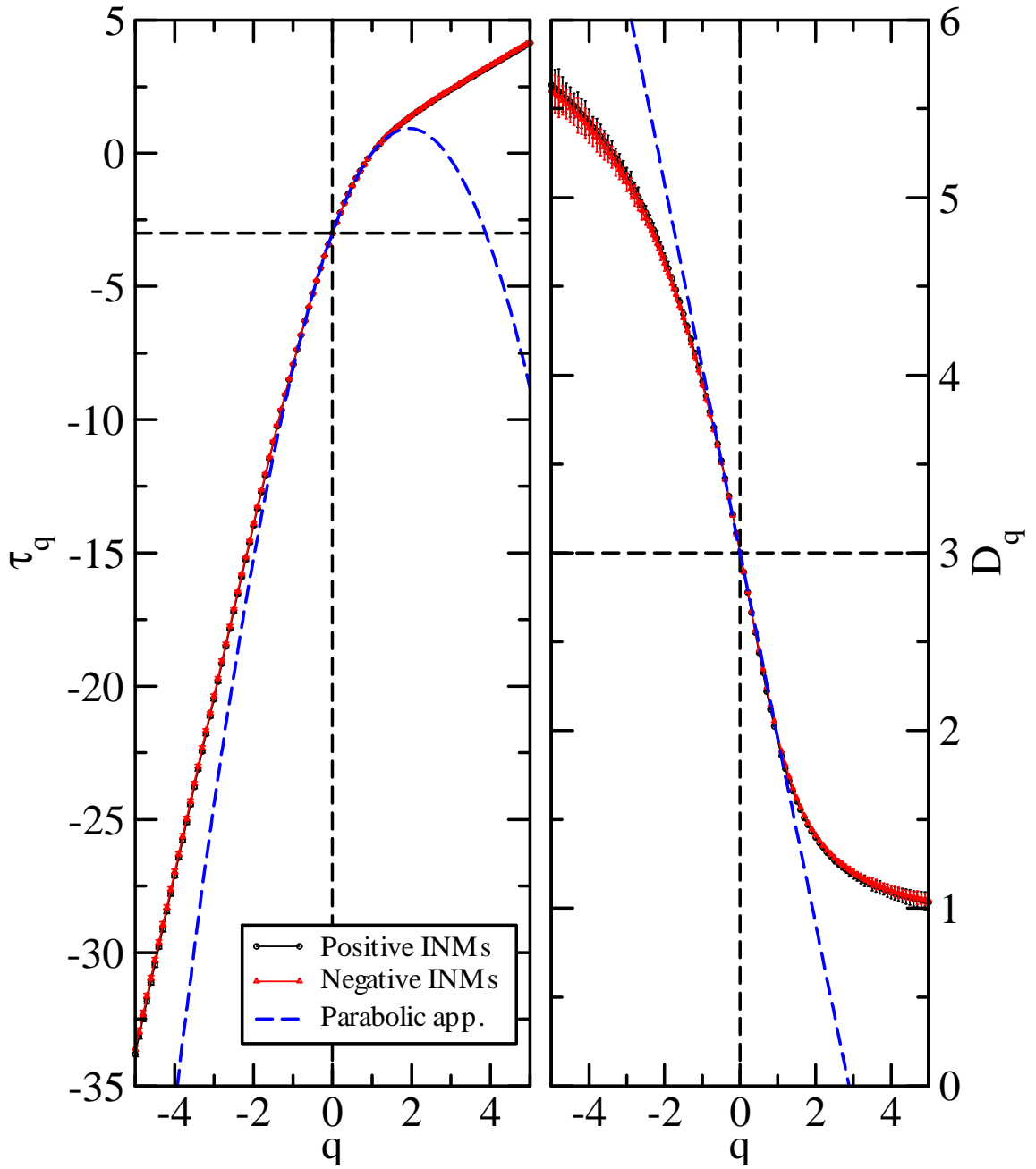
Figure 5.3: The scaling exponent τ_q and the corresponding fractal dimension D_q in both branches. The black and red lines are for the postive and negative branches, respectively. The blue dash lines denote the parabolic approximation given in eq.(5.15) and (5.16).
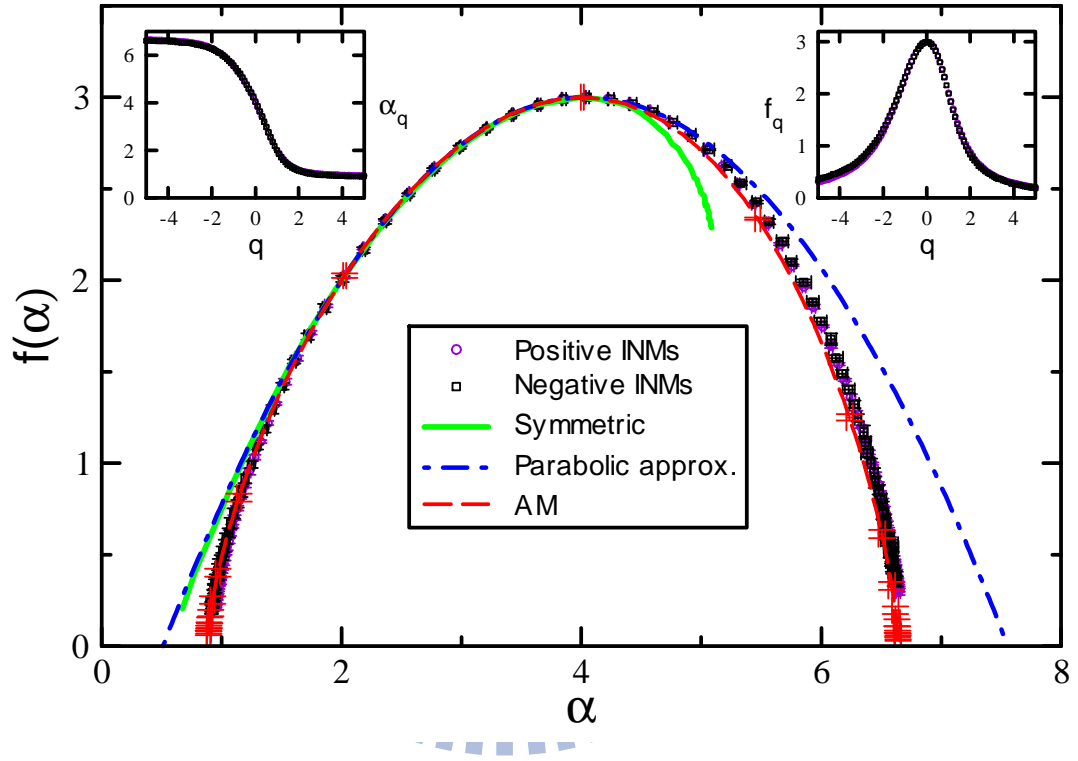
Figure 5.4: Singularity spectrum $f(\alpha)$ at the ME, with $\lambda = 1183.8 \pm 1.0$ (circle) and $\lambda = -86.6 \pm 0.5$ (squares), for $N = 96000$. $f(\alpha)$ is generated with the data of α_q and f_q shown in the insets for $-5 \leq q \leq 5$ in a step of $\Delta q = 0.1$. The solid line is the corresponding spectrum transformed with the symmetric relation in Eq.(5.18). The dat-dash line is the parabolic approximation with $\alpha_0 = 4.04$. The red dash line is the result of Anderson model at the critical disorder [86].
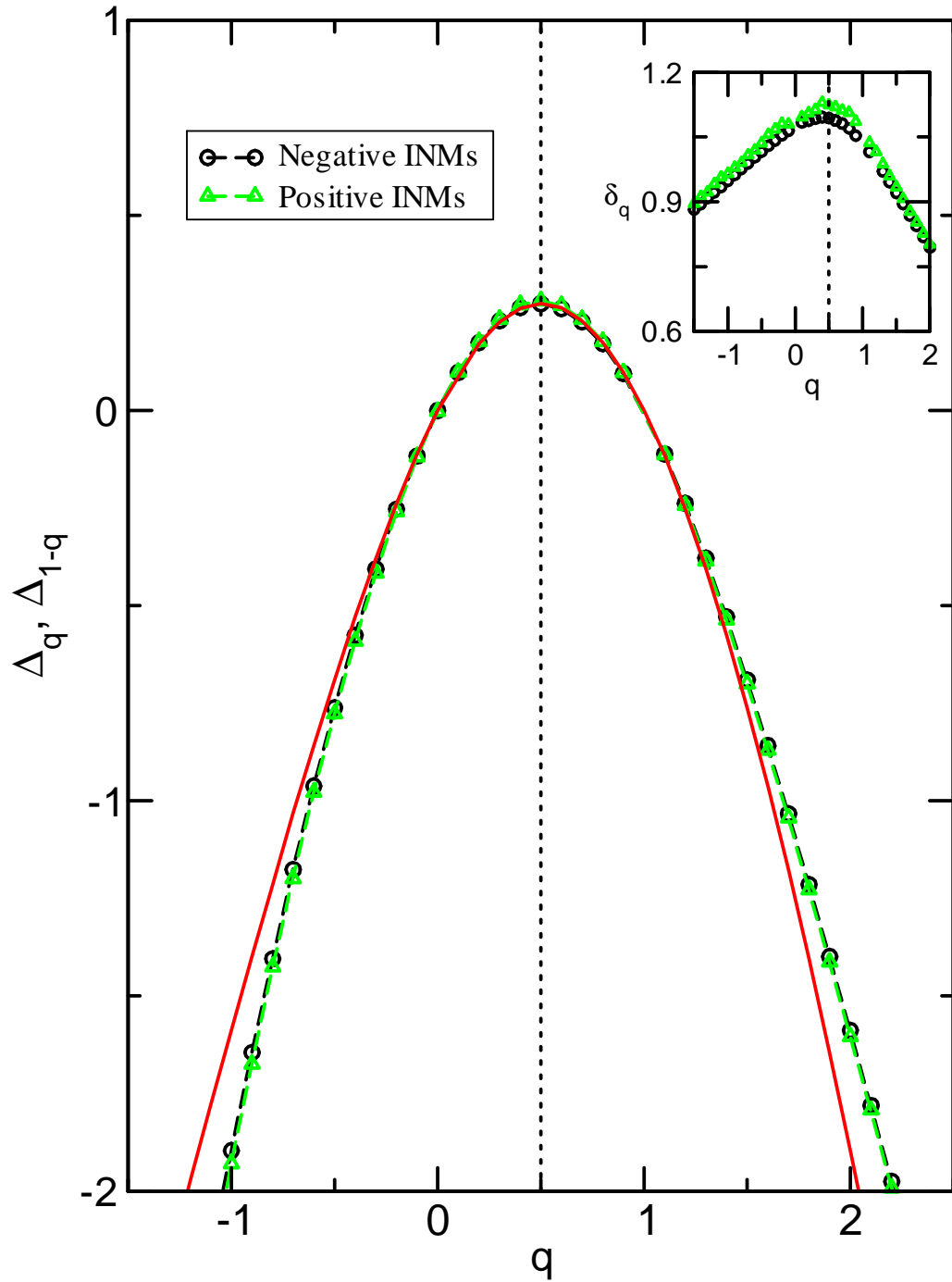
Figure 5.5: Anomalous dimension Δ_q and reduced anomalous dimension δ_q (inset) versus q at the ME. The circles and triangles, guiding the eye with the dashed line, are the Δ_q data of the INMs with $\lambda = -86.6 \pm 0.5$ and 1183.8 ± 1, respectively. The numerical errors are smaller than the symbol size. The solid line shows the mirror image of the numerical data with respect to the line $q = 1/2$.

with the symmetric relation for $2 \leq \alpha \leq 4$. To example the symmetric relation of Δ_q in Eq.(5.17), we plot in Fig.5.5 the anomalus dimension Δ_q at the ME of both branches and compare Δ_q with Δ_{1-q}, which is obtained by the mirror image of Δ_q with respective to $q = 1/2$. Our data of Δ_q at each ME are satisfied with the symmetric relation for q between -0.5 to 1.5. Shown in the inset in Fig.5.5 is the reduced anomalous dimension $\delta_q = \Delta_q/q(1-q)$. The overall shape of our numerical δ_q versus q is similar as that measured by the multifractal ultrasounds on the surface of an elastic network[98].

According to our numerical results, we conclude that the multifractals at the MEs in the INM spectrum behave in the same features as those obtained by the lattice AM at the critical disorder. The numerical agreement between our results and those of the AM indicates the universality of the multifractality at the LDT.

5.2   To determine mobility edge of negative branch by MFA

Based on the system size dependence of SSP, the strength of squared vibrational amplitudes α_q can serve as a quantity to locate the mobility edge. Recently, it is suggested that α_1 directly correlates with the von Neumann entroy of quantum entanglement[93], and the entanglement entropy also serves as a quantity to determine the localization-delocalization transition[94].

Serving as a alternative analysis to locate the ME, we calculate the α_0 and α_1 for the imaginary branch with seven different system sizes from $N = 3000$ to $N = 96000$ and different eigenvalue regimes. Fig. 5.6 shows α_0 and α_1, in which more than 1.5×10^3 states are averaged. Each line denotes α_0 of different frequency from $\lambda = -83.1$ at the bottom to $\lambda = -90.1$ at the top and α_1 in reverse term. Note that the dash and dot-dash lines, shown with approximately zero gradient, correspond to the regime at $\lambda = -87.1 \sim -86.1$. It could be seen that near the ME both α_0 and α_1 reveal the system-size invariance. Following reference [95], we define the slope $g = d\alpha_q/d(\ln L)^{-1}$. Fig. 5.7 shows g with respect to λ, because that α_0 and α_1 are almost independent of system size withinin the interval $-87.1 < \lambda < -86.1$, the zero-crossing g value locate the mobility edge. The results of our data, within numerical

errors, almost agrees with that obtained by the LS statistics[79][80]

In the following, we investigate the vibrational amplitudes in the multifractal INMs and only present the results at the ME in the negative branch.

5.3 Probability Density Function of Vibrational Amplitudes

Another approach to characterize the multifractal INMs is the statistics of the squared vibrational amplitudes in a INM eigenvector. By the box-counting method defined in previous section, the LPD, μ in $N_\eta = \left(\frac{L}{l}\right)^3$ boxes with size $L' = \frac{L}{l} = \eta^{-1}$ is defined as Eq.(5.5). For the non coarse-grain case, $l = 1$, the μ corresponds to squared vibrational amplitude $|\psi_i|^2$. Averaged for the multifractal INMs of LPD μ, the probability density function (PDF) $\widetilde{p}_L(\mu)$ of the LPD μ is defined such that $\widetilde{p}_L(\mu)d\mu$ is the ratio $\Delta N_\mu / N_\eta$, where ΔN_μ is the averaged number of particles with lying between μ and $\mu + d\mu$ in an INM. By changing variable to the singularity strength $\alpha \equiv \ln \mu / \ln \eta$, the corresponding PDF $P_L(\alpha)$ is given as $P_L(\alpha) = \widetilde{p}_L(\mu) d\mu / d\alpha$. The probability of finding a singular strength correspond to $[\alpha, \alpha + d\alpha]$ is $P_L(\alpha) d\alpha = \Delta N_\alpha / N_\eta$. Based on the definition $\Delta N_\alpha \sim L^{f(\alpha)}$, therefore

$$P_L(\alpha) \sim L^{f(\alpha) - d}.$$

Due to the recent numerical results of the AM in 3D [97], it is suggested that the proportionality of the scaling is the value of the PDF at α_0, where $f(\alpha_0) = d$. Therefore, $P_L(\alpha)$ can be expressed as

$$P_L(\alpha) = P_L(\alpha_0) L^{f(\alpha) - d},$$

and the PDF-based SSP read as

$$f(\alpha) = \frac{\ln\left(\frac{P_L(\alpha)}{P_L(\alpha_0)}\right)}{\ln L} + d. \tag{5.19}$$

Since the scale invariance of α_0 with system size, the position of the maximum PDF is expected to be independent of L.
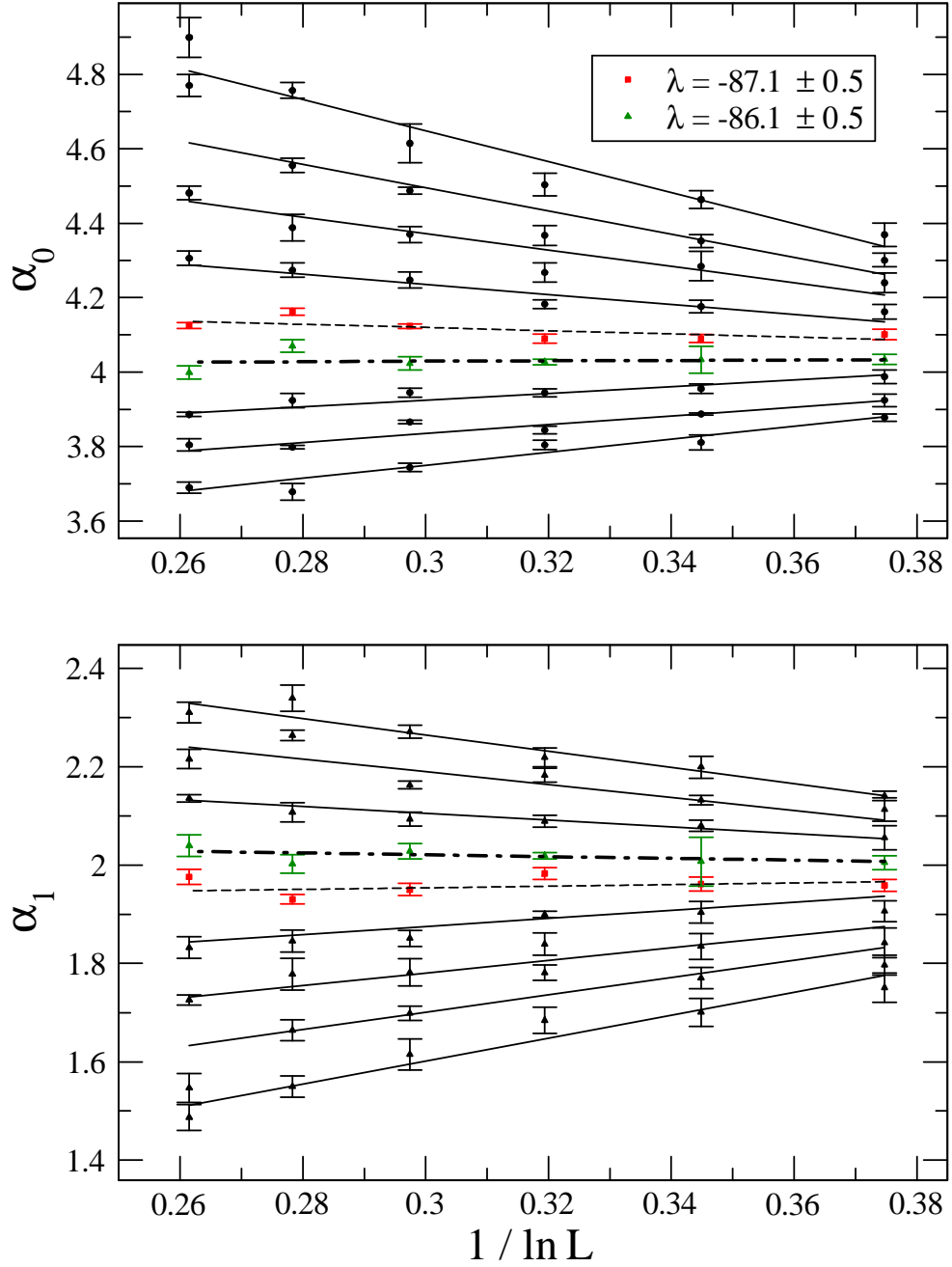
Figure 5.6: Estimation of the mobility edge for the negative branch. Each line is for a different frequency, α_0 from $\lambda = -83.1 \pm 0.5$ at the bottom to $\lambda = -90.1 \pm 0.5$ at the top in steps of $\Delta\lambda = 1.0$ and α_1 in reverse term. The lines show the linear-fitting resluts. Note that the dash and dot-dash lines, shown with approximately zero gradient, correspond to the regime $\lambda = -87.1 \sim -86.1$.

Figure 5.7: $g(\lambda) = d\alpha(q,\lambda)/d(\ln L)^{-1}$ for $q = 0$ and 1. The crossing point denotes the ME.

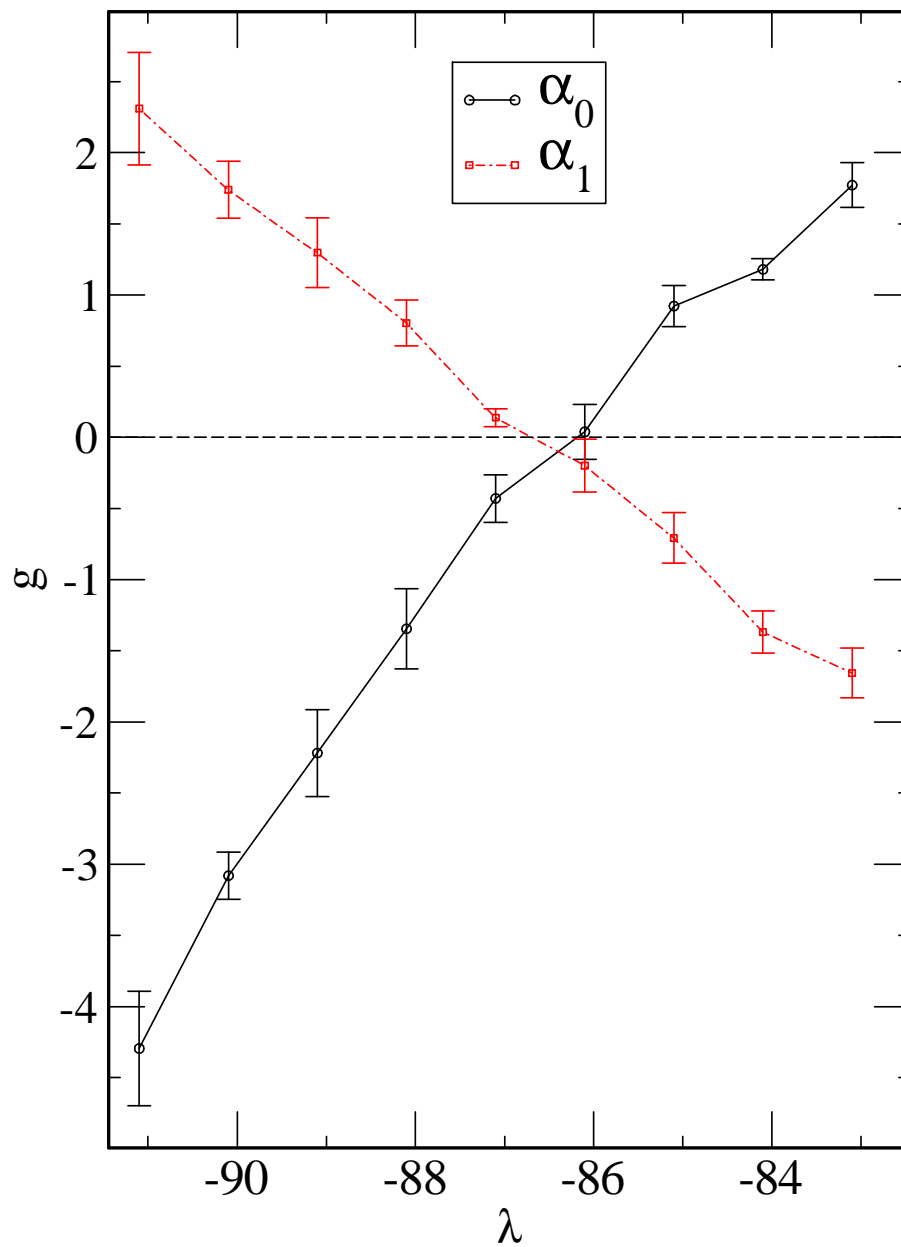By using the PA of $f(\alpha)$ in Eq.(5.14), we obtain a Gaussian approximation (GA) of $P_L(\alpha)$ as

$$P_L^{GA}(\alpha) = P_L(\alpha_0) \exp\left\{-\frac{(\alpha - \alpha_0)^2}{4(\alpha_0 - d)} \ln L\right\}. \tag{5.20}$$

Under the GA, the distribution width of $P_L(\alpha)$ decreases with $(\ln L)^{1/2}$, while, due to the normalization of the PDF, the maximum $P_L(\alpha_0)$ increases with $(\ln L)^{1/2}$. On the orther hand, in terms of the symmetric relation of $f(\alpha)$ in Eq.(5.18), $P_L(\alpha)$ for large enough L is expected to be equivalent with the one generated via the symmetric transformation (ST)

$$P_L^{ST}(\alpha) = L^{\alpha - d} P_L(\alpha), \tag{5.21}$$

where $0 \leq \alpha \leq 2d$. The equivalence of $P_L(\alpha)$ and $P_L^{ST}(\alpha)$ implies that the values of $P_L(\alpha \geq d)$ and $P_L(\alpha \leq d)$ are correlated with each other. Therefore, the investigation of $P_L(\alpha)$ alternatively provides an insight on the properties of $f(\alpha)$.

Calculated with more than 7000 INM eigenvectors for N from 3000 to 96000, the variation of the numerical $P_L(\alpha)$ distribution with system size is shown in Fig. (5.8). Located at $\alpha = 4.1 \pm 0.02$, the position of the $P_L(\alpha)$ maximum is almost invariant with the system size. Within our numerical resolution, this position is consistent with α_0 obtained from the maximum of $f(\alpha)$ at the negative-λ ME in Fig.(5.4). At $\alpha_0 = 4.1$, the scaling of $P_L(\alpha_0)$ with $\ln L$ generally follows the prediction of the GA.

Fig.(5.9) shows coarse-grain PDF of α, where $L' = \eta^{-1}$ is arranged from 5 to 25. Comparing with the coarse-grain procedure of the Anderson model in 3D simple cube, the simple fluid is characterized by the variation of number particle within a small box, which induces another kind of fluctuations except for the fluctuations of the squared vibrational amplitudes. In the inset(b) of Fig.(5.9) shows the distribution of number particles n within a small box diveded by average number particle $\langle n \rangle$. It can be seen that for large L' the fluctuation of n is larger while for small L' the fluctuation of n is smaller.

The comparision of $P_L(\alpha)$ with $P_L^{GA}(\alpha)$ and $P_L^{ST}(\alpha)$ is shown in Fig.(5.10a) for $N = 96000$. Our results indicate that $P_L(\alpha)$ obtained numerically is neither identical with the GA in Eq.(5.20) nor with the ST in Eq.(5.21), especially for large α, which corresponds to small vibrational amplitudes. To examine the deviation of $P_L(\alpha)$ under the GA and the ST, we define the deviation $\delta P_L^O(\alpha) = P_L(\alpha) - P_L^O(\alpha)$, where

O is either GA or ST, and the integrated deviation $\delta P_L^O = \int_0^{\alpha_c} \left| \delta P_L^O(\alpha) \right| d\alpha$, where $\alpha_c = 2d$ for $O =$ST and $\alpha_c = 7$ for $O =$GA. The numerical results of $\delta P_L^O(\alpha)$ are presented in Fig.(5.10b) for N varied from 3000 and 96000, and the system-size dependences of δP_L^{ST} and δP_L^{GA} are in the inset of the figure. For the system sizes we investigate, the GA generally has a smaller integrated deviation than the ST does. The integrated deviation under the ST is found to decrease with increasing system size; this is consistent with the result obtained by the AM [97]. However, the integrated deviation under the GA fluctuates with the system size and the fluctuation does not decay with increasing the system size, which implies the non-Gaussian nature of $P_L(\alpha)$ even for a large system size. Thus, our results indicate that by increasing the system size, the singularity spectrum $f(\alpha)$ gets satisfied with the symmetric relation in Eq.(5.18) but not with the GA in Eq.(5.14).

Fig.5.11 shows comparison of singularity spectrum at the MEs in negative branch by the box-counting method for INMs, AM, and the PDF-based SSP by Eq.(5.19). Generally, the PDF-base SSP agrees with the box-counting results. Furthermore, the PDF-base SSP is an ensemble average quantity intrinsiclly, which lead to the negative $f(\alpha)$ correspond to small and large α. The ΔN_α for a given L, gives the number of points in the wave function with amplitudes in the range $|\psi_i|^2 \in \left[L^{-\alpha - \Delta\alpha/2}, L^{-\alpha + \Delta\alpha/2} \right]$. It scales with the system size as $\Delta N_\alpha \sim L^{f(\alpha)}$. The negative values of $f(\alpha)$ correspond to those ΔN_α decreasing with L for large enough L. Physically, the negative fractal dimensions at small α are caused by the so-called rare events containing localizedlike regions of anomalously high $|\psi_i|^2$ at criticality. The probability of finding them likewise decreases with L. The estimated value for the threshold α_-, where $f(\alpha_-) = 0$, is $\alpha_- \in [0.641, 0.675]$.

5.4 Spatial Correlations

To characterize the spatial structures of the multifractal INMs, we define the spatial correlation function for the q-th moment of the squared vibrational amplitudes

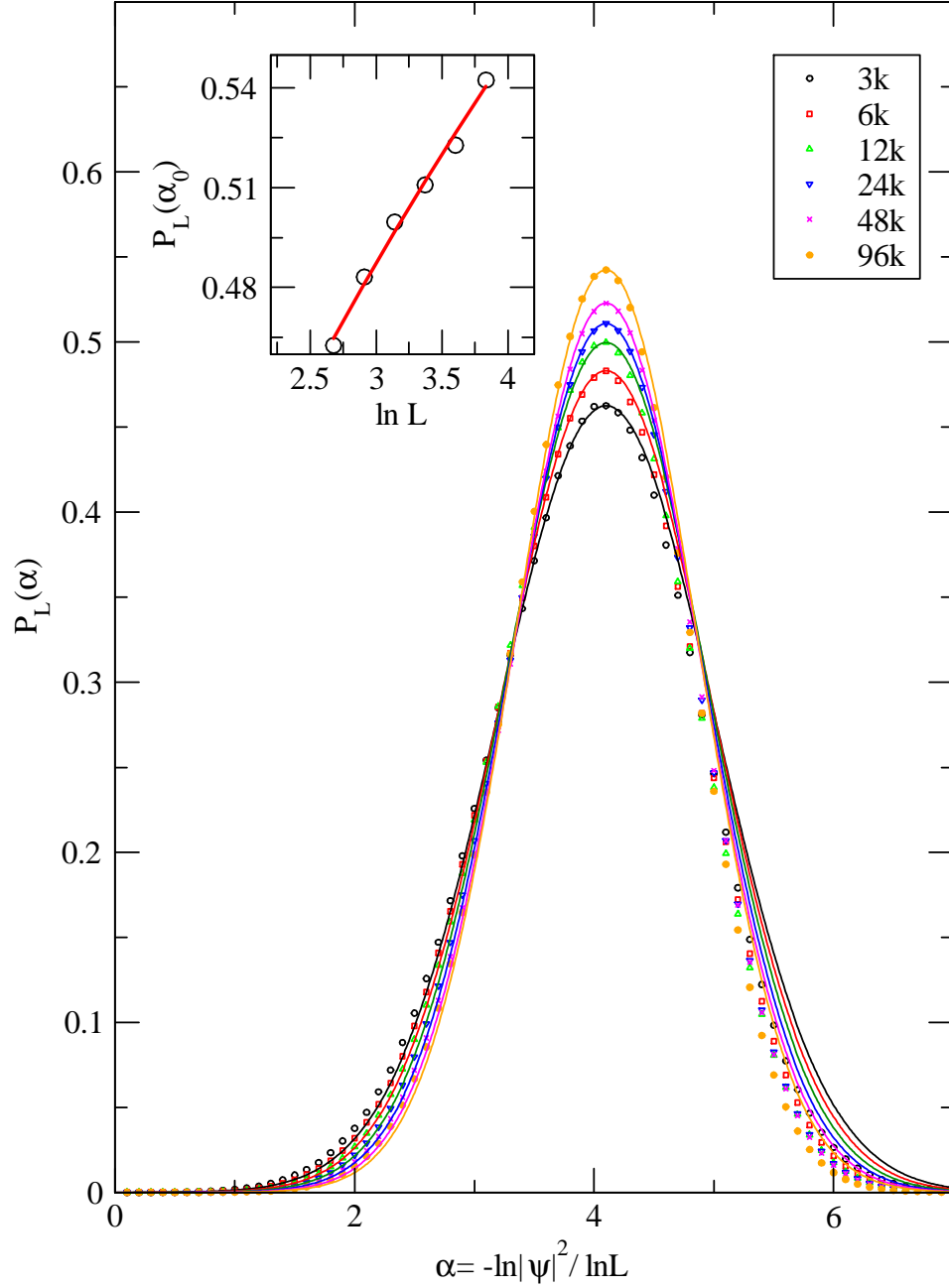Figure 5.8: System-size dependence of $P_L(\alpha)$ for INMs at the ME of $\lambda = -86.6 \pm 0.5$, with $\alpha = -\ln|\psi_i|^2 / \ln L$. The symbols denote numerical data with the resolution $\Delta\alpha = 0.04$. Solid lines denote the Gaussian as eq.(5.20). The inset shows $P_L(\alpha_0)$ with $\alpha_0 = 4.10$ versus $\ln L$ and the fit $A \cdot (\ln L)^B$ (Solid line) with $A = 0.30$ and $B = 0.458$.
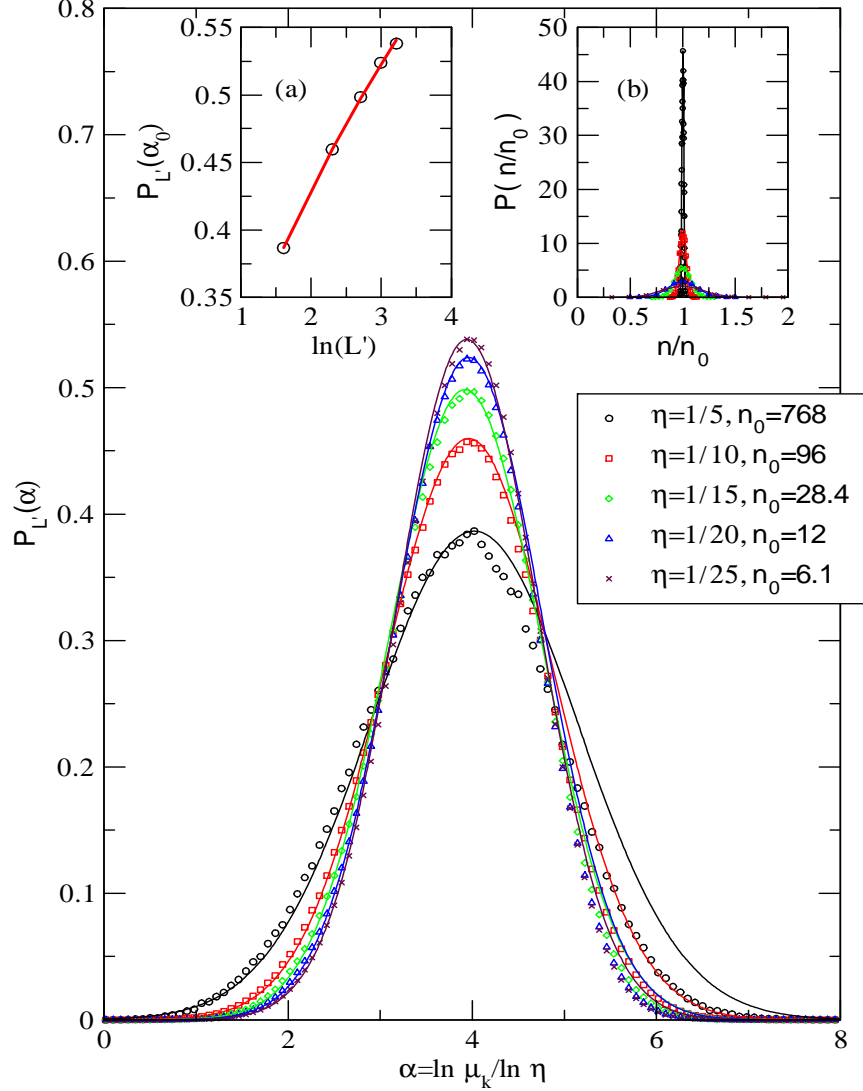
Figure 5.9: Box-size dependence of $P_{L'}(\alpha)$ for INMs at the ME of $\lambda = -86.6 \pm 0.5$, with $\alpha = -\ln \mu_k / \ln L'$. More than $7,000$ modes of $N = 96,000$ are averaged. Symbols denote numerical data of different coarse-grain ratio η with $\Delta \alpha = 0.02$. Solid lines denote the GA as Eq.(5.20). The inset (a) shows $P_{L'}(\alpha_0)$ with respect to $\ln L'$ and the power law fitting is $P_L(\alpha_0) = A \cdot (\ln L)^B$ with $A = 0.30745$ and $B = 0.48268$. The inset (b) shows probability distribution of the particle number n in a small box with size $L \cdot \eta$. $n_0 = N\eta^3$ is the average number of particles in a small box.
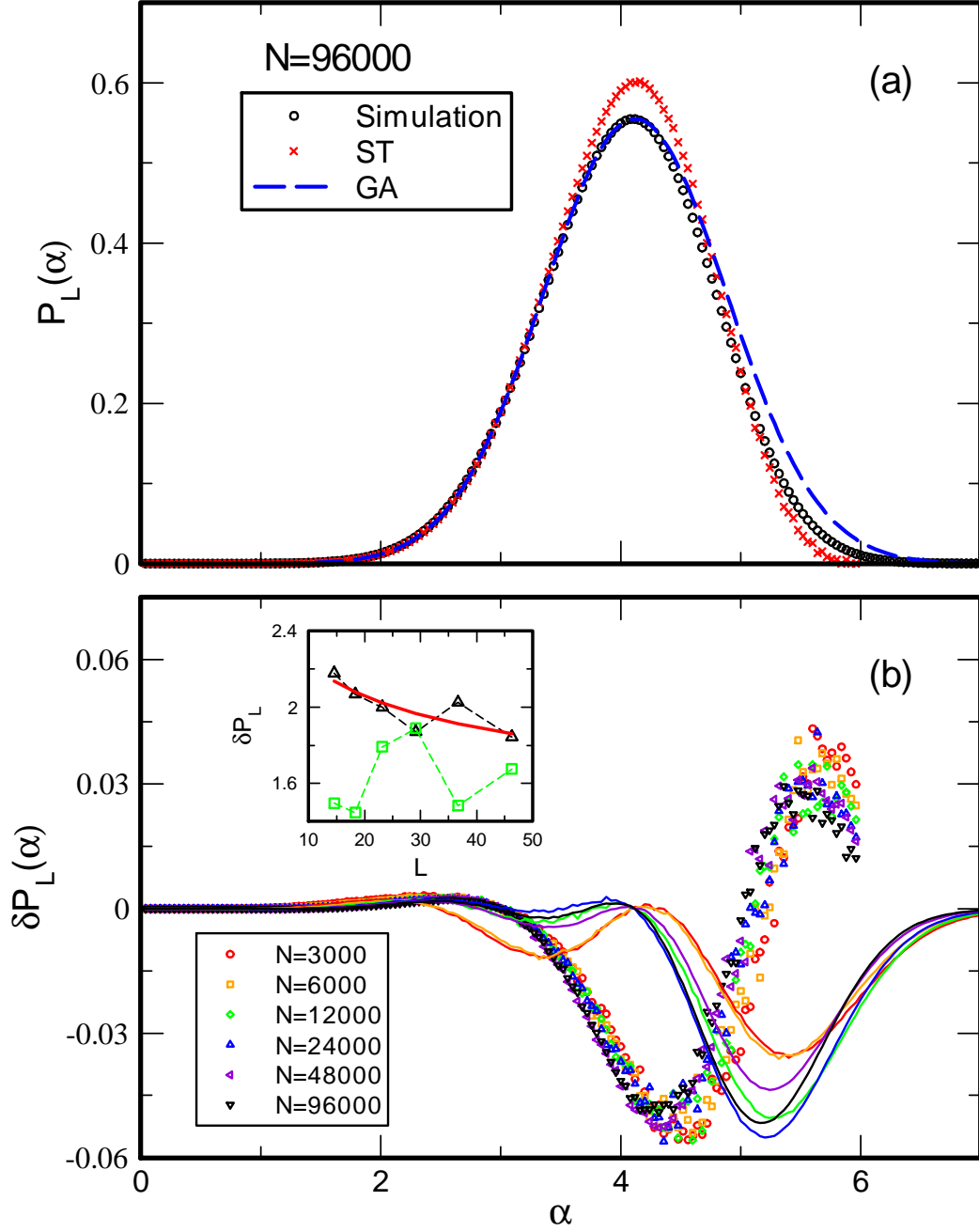
Figure 5.10: (a)$P_L(\alpha)$ (circles), $P_L^{GA}(\alpha)$ (dashed line) and $P_L^{ST}(\alpha)$ (crosses) for $N = 96000$. (b) $dP_L^{GA}(\alpha)$ (solid lines) and $dP_L^{ST}(\alpha)$ (symbols) of system size N, indicated by different colors. In the inset, the squares and triangles show the system-size dependences of $dP_L^{GA}(\alpha)$ and $dP_L^{ST}(\alpha)$, respectively, and the solid (red) line is the fit of aL^{-b} for $dP_L^{ST}(\alpha)$, with $b = 0.12$.
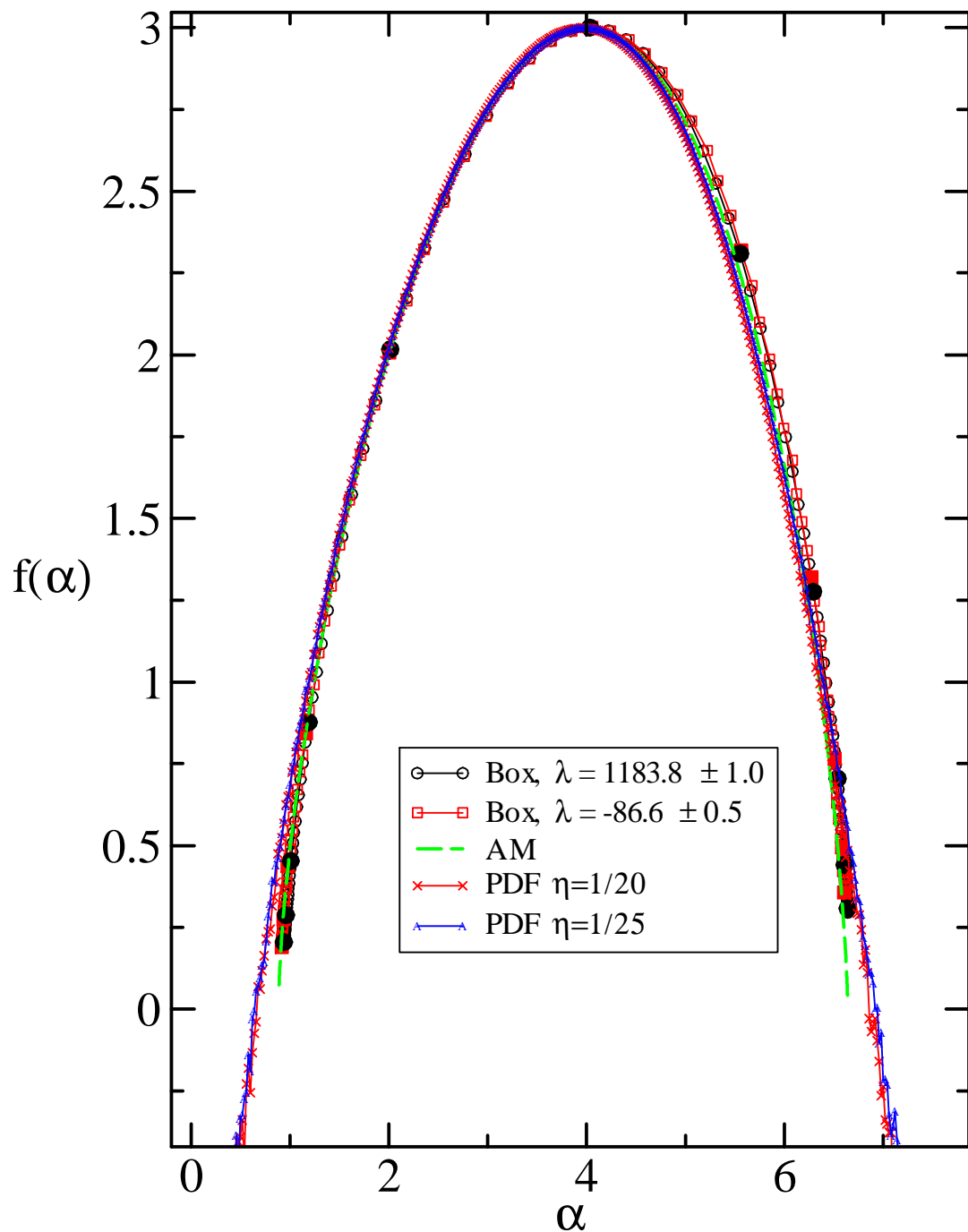
Figure 5.11: Comparison of singularity spectrum at the MEs by the box-counting method for INMs, AM, and the PDF-based for INMs in the negative branch. The open diamands and squares deonte the box-counting for the positive and the negative branches, respectively. The green dash line is the results of AM. The red cross and blue char correspond to the PDF-based SSP with the coarse-grain $\eta = \frac{1}{20}$ and $\frac{1}{25}$, respectively.

in the INMs in a system of size L as

$$C_q(r, L) = \left\langle \frac{1}{N} \sum_{i=1}^{N} \sum_{j \neq i}^{N} |\psi_i|^{2q} |\psi_j|^{2q} \, \delta(r - r_{ij}) \right\rangle_\lambda, \tag{5.22}$$

where r_{ij} is the distance between particle i and j and the brackets denote an ensemble average for the mutifractal INMs at a ME. In the definition of $C_q(r, L)$, r is the distance between two particles in the fluid and is assumed to be smaller than L. Since the distribution of squared vibrational amplitudes depends on L, $C_q(r, L)$ is not only a function of distance r between two particles but also dependent on L [31]. In terms of ΔN_r, which is the particle number within a spherical shell between r and $r + \delta r$ and centered at a chosen particle, due to the absence of characteristic lengths in the multifractal system, $C_q(r, L)$ is changed to

$$C_q(r, L) = \left\langle \frac{1}{N \Delta N_r} \sum_{i=1}^{N} \sum_{j=1}^{\Delta N_r} |\psi_i|^{2q} |\psi_j|^{2q} \right\rangle_\lambda, \tag{5.23}$$

where the second summation is subject to those particles within the shell.

Based on the multifractal nature at Anderson transition, a scaling argument for the spatial correlation function has been proposed and calculated for the critical states in quantum Hall systems [99] [100]. With a similar scaling argument for the squared vibrational amplitudes in a multifractal INM given in Appendix A.3, the behavior of $C_q(r, L)$ is predicted as

$$C_q(r, L) \propto L^{-y_q} \cdot r^{-z_q}, \tag{5.24}$$

where y_q and z_q are the correlation exponents with respect to the system size and the spatial distance, respectively, and they are given as

$$y_q = d + \tau_{2q}, \tag{5.25}$$

$$z_q = d + 2\tau_q - \tau_{2q}. \tag{5.26}$$

By using the PA of τ_q in Eq.(5.15), y_q and z_q in the PA are expressed as

$$y_q^{PA} = 2\alpha_0 q - 4(\alpha_0 - d)q^2, \tag{5.27}$$

$$z_q^{PA} = 2(\alpha_0 - d)q^2. \tag{5.28}$$

To examine whether the correlation exponents of the multifractal INMs follow the predictions of the scaling argument, we calculate $C_q(r, L)$ at a ME in the negative branch for different system sizes. Present in Fig.(5.12a) are the $C_q(r, L)$ of $N = 48,000$ with $0 < q < 2$ for the distances r less than the half of $L = 36.69$. To extract the data of z_q, we make a linear fit for the data of each q in Fig.(5.12a), characterizing the power law decay of $C_q(r, L)$ with respect to r. The slope of the linear fit gives the numerical result of z_q presented in Fig.(5.12b), with the error of z_q estimated within the 95% confident interval. For large q , the original data of $C_q(r, L)$ suffer from strong fluctuations, which cause larger errors in z_q. The predictions by the scaling theory and the PA for z_q are also shown in Fig.(5.12b) for comparison. Our results indicate that the numerical data of z_q are generally consistent with scaling theory for $q < 1$ and the PA in Eq.(5.28) is only good for $q < 0.7$, which is consistent with the result for the PA of τ_q shown in Fig.(5.3a).

The Eq.(5.25) is also verified in our numerical work. Fig.(5.13a) shows the correlation function $\ln C_q(L)$ with respect to system size $\ln L$ of different q , where the system size arrange from $N = 3,000$ to $48,000$. The results of four selected distances $r = 4.0, 4.5, 5.0$ and 5.5 are averaged, where the error bars denote the standard deviation of four corresponding $C_q(L, r)$. The slope indicates the numerical scaling result of y_q plotted in Fig.(5.13b), which characterizes the power law dependence of $C_q(L)$ with respect to L at specified r. The black line denotes the scaling theory from Eq.(5.25) and the blue dash line denote the scaling theory with the parabolic approximation, where τ_q is replaced by τ_q^{PA} in Eq.(5.25). The numerical results agree with analytic prediction from Eq.(5.25) for $q < 1.2$.

5.5   The distribution of inverse-participation ratio

The fluctuation of individual INM revels in the distribution of IPR. At $q = 2$, the distribution of $\ln P_2$ has extensively studied in the AM and the power-law random band model[75]. It has been verified that the value of maximum distribution of $\ln P_2$ at the ME of AM decreases with increasing system size and is saturated to a constant[73][74].

Fig. 5.14 shows the $\ln P_2$ distribution at the ME in the positive branch for different
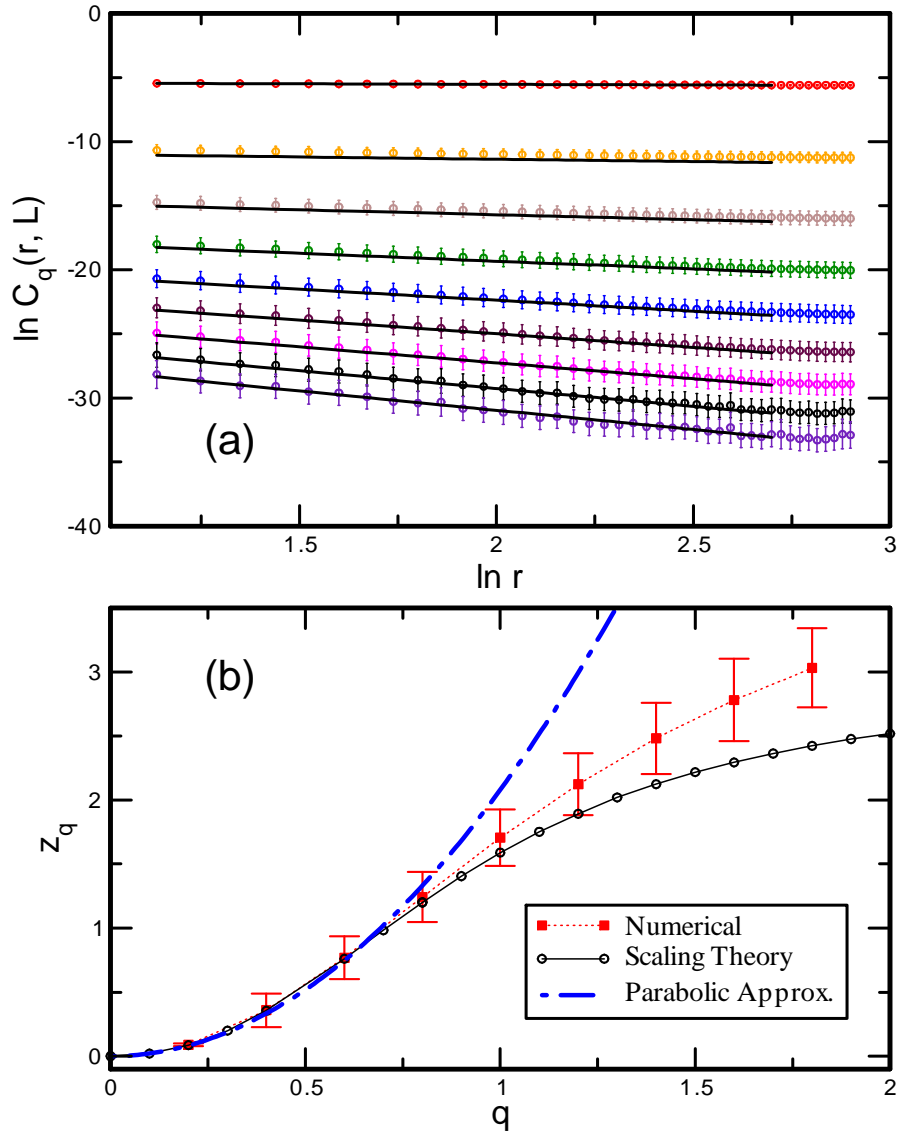
Figure 5.12: (a) Spatial dependence of $C_q(r, L)$ in a log-log plot. The symbols are the averaged results of INMs with $\lambda = -86.6 \pm 0.5$ in the system of $N = 48000$. The data from top to bottom are q from 0.2 to 1.8 with a step of $\Delta q = 0.2$. The solid lines are a linear fit for each q.(b) Correlation exponent z_q versus q. The red squares are obtained by the fit result of each q in (a). The open circles are the prediction of Eq.(5.26). The blue dot-dash line is the PA in eq.(5.28).

Figure 5.13: (a) System-size dependence of $C_q(r, L)$ in a log-log plot. The numerical data are calculated at $r = 5$ for INMs with $\lambda = -86.6 \pm 0.5$ in five system sizes. From left to right, the data are for N from 3000 to 48000; from top to bottem, the values of q are from 0.2 to 1.6 with a step of $\Delta q = 0.2$. The dashed line is a linear fit for each q. (b) Correlation exponent y_q versus q. The filled squared are th fit results of each q in (a). The open circles are the prediction of Eq. (5.25). The dot-dash line is the PA in Eq.(5.27).

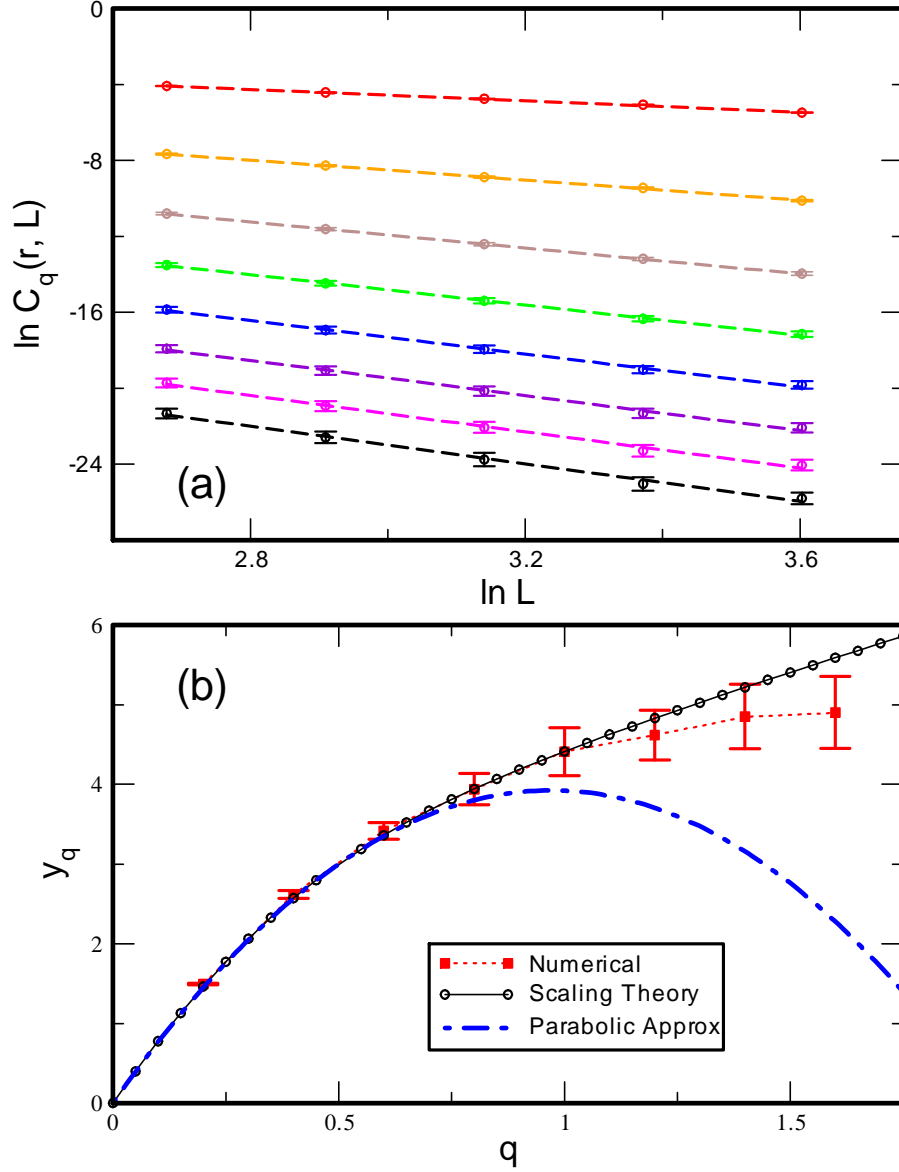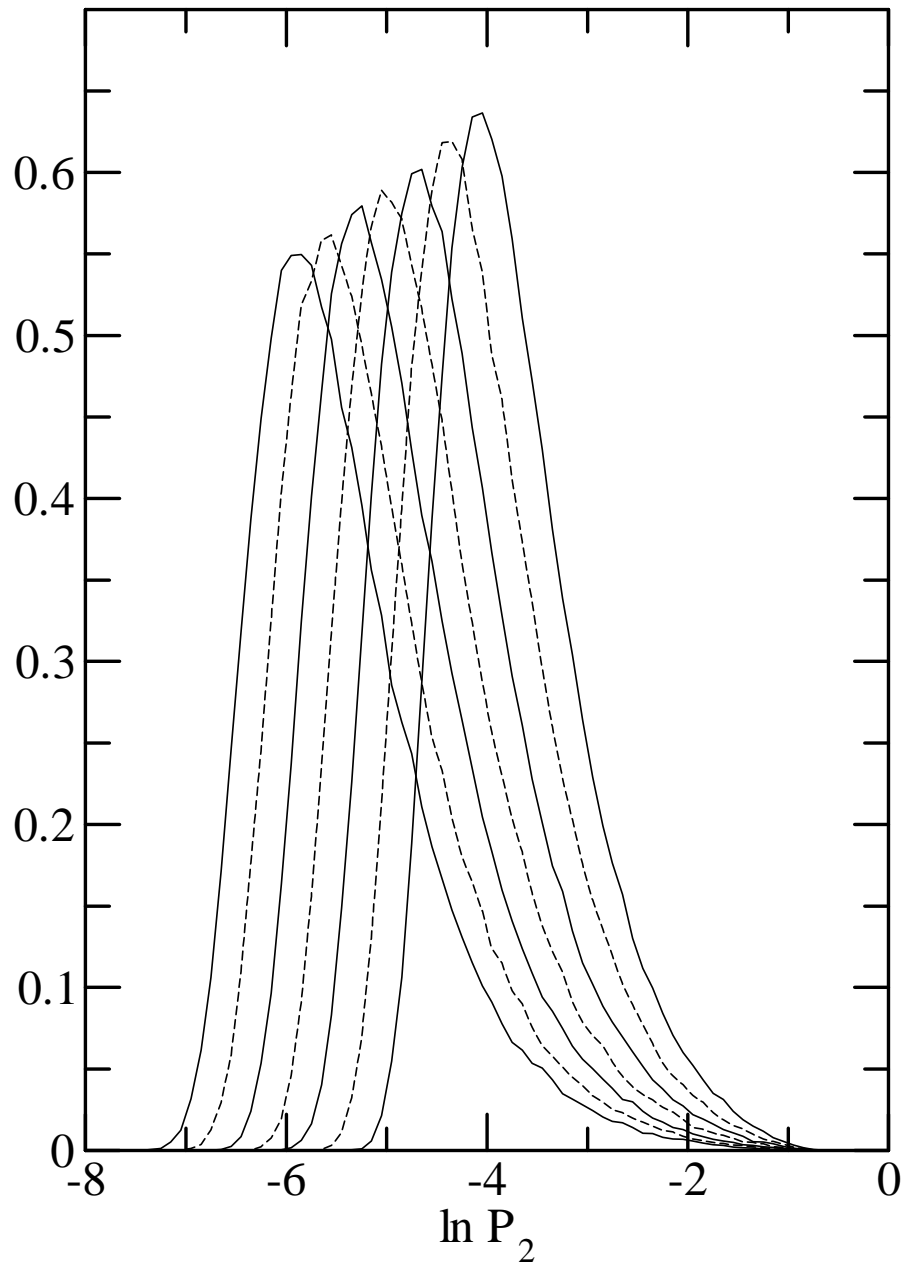Figure 5.14: The Figure shows the distribution of $\ln P_2$ of different system sizes. From right to left, $N = 1500, 3000, 6000, 12000, 24000, 48000$ and 96000.

system sizes, from right to left corresponding to small to large system sizes. For all system sizes, the number of states in average are more than 3×10^5, except that for $N = 96000$ the number is 2×10^5. Generally, the distributions are assymetry with a long tail in the side of large value $\ln P_2$. For small sizes the distributions are narrower and sharp due to the size effect. For larger sizes, it seems that the value of maximum distribution of $\ln P_2$ closes to some constant.

On the left hand side of the distributions corresponding to small $\ln P_2$, the behavior of the eigenvectors is more extended-like, and a sharp cutoff the $\ln P_2$ value presents, which is far away from the value $\ln P_2 = -\ln N$ corresponding to the completely extended eigenvector. For a completely extended eigenvector, the values $\ln P_2$ give -11.47 and -7.31 corresponding to $N = 96000$ and 1500, respectively. On the other hand, for large values of $\ln P_2$, the behavior of the eigenvectors is more like the localized wave, in which a few particles dominate the amplitutes of a wave. An INM at the ME with extremely large or small values of $\ln P_2$ still exist, yet the probability is extremely low. Such INMs often refer to the rare realizations, which correspond to the negative value of the ensemble average $f(\alpha)$ near the two edges α_+ and α_-. The negative value of $f(\alpha)$ means that the rare realizations vanish eventually when the system size increases. Generally, the results agree with the Anderson model[74][73].

5.6 Summary

We have performd the multifractal analysis at the ME in the both positve and negative branches of the INM spectrum. A set of general dimensions charaterize the strong fluctuations of the multifractal INMs and at the ME the general dimensions for both branches are consistent. By means of box-size scaling and based on the Legendre transform of the mass exponent, we have calculated the singularity spectrum (SSP), which shows excellent agreement with the AM. We confirm that the SSP is a universal quantity. According to the invariance of the SSP with respect to system size, the location of the ME with the value $\lambda = -86.6 \pm 0.5$ is determined in the negative branch, and the value generally agrees with the results of the LS analysis.

The symmetry relation of the multifractal INMs is verified. Our data of Δ_q at each ME are satisfied with the symmetric relation for q between -0.5 to 1.5. Similarly,

$f(\alpha)$ obtained by the INMs is generally satisfied with the symmetric relation for $2 \leq \alpha \leq 4$. Our results suggest that the symmetric relation is obeied only for our model in a very large system size; this conclusion is similar as the one obtained by the AM. In principle, the multifractals at the LDT exhibit the self-similarity for all length scales, indicating the absence of a length scale in the system. However, our model and the AM are numerically discrete models with a unit length, which is the lattice constant in the AM or the particle size in our model. In a length scale comparable with the unit length of a discrete model, the basic assumption of the multifractality breaks down for the discrete model. We think that this is the reason why the system sizes of our model and the AM should be extremely large in order to fulfill the proposed symmetric relation for the singularity spectrum.

For the multifractal INMs, the PDF of the logarithm of the squared vibrational amplitudes is calculated for several system sizeds. The PDF is related to the singularity spectrum. The calculated PDFs are examined for the singularity spectrum under the PA or subject to the symmetric relatoin. Under the PA, the PDF should be Gaussian, indicating that the the squared vibrational amplitudes follow a log-normal distribution. At small vibrational amplitudes, the calculated PDFs of all systems sizes are apparently deviated from the Gaussian and the one with the singularity spectrum subject to the symmetric relation. However, our results indicate that, as the system size of our model becomes larger and larger, the deviation in the latter case gets smaller and smaller but the deviation in the former case does not.

Moreover, the correlation function of the q-moments of components of INMs also be calculated. The power-law decay of the correlation function is verified to connect with the mass exponents. Finally, we present the distribution of $\ln P_2$, which has the same nature with the AM.

Chapter 6

Conclusions

The localization-delocalization transition has been a general concept in condensed matter physics and affects the the transport properties in materials fundamentally. The universal properties at the localization-delocalization transition among different physical systems have been widely studied since the three universal ensemble in the RMT was purposed : the unitary, orthogonal and symplectic. We have investigated the critical properties at the LDT in the INM spectrum of a TLJ fluid at a thermodynamic state; the TLJ fluid is a topologically disordered system, which has no reference frame of lattice.

In chapter three, we have performed LS analysis for Hessian marices of the TLJ fluid. The Hessian matrices evaluated at the fluid configiations are an ensemble of Euclidean random matrices with elements subject to several constrants, and the matrices are sparse due to the short-range nature of the TLJ potential. By referring the eigenmodes of the matrices as the INMs, the eigenvalue spectrum of the INMs is composed to two branches corresponding to the positive and negative eigenvalues. We have used the finite-size scaling to estimate the locations and the critical exponents of the two MEs. In the models to fit the data of the second moments, the nonlinear dependence of the scaling variable on the eigenvalue has been condisdered and an irrelevant scaling variable due to the finite-size effect is introduced in some models for the positive branch. In principle, the critical exponents of the two MEs should coincide in value; through the fitting, their values are found to be 1.55 ± 0.09 and 1.60 ± 0.03 for the positive and negative branches, respectively. Within numerical errors, the estimated values of the two critical exponents are almost coincident with

each other and compatible with that of the AM in three dimensions [17]. The nearest-neighbor LS distributions at the two MEs are examined to be almost the same as the critical LS distribution obtained from the AM. Thus, we conclude that the MEs in the eigenvalue spectra of Hessian matrices of topologically disordered systems follow the universality for the othogonal universality class and have nothing to do with the topological nature of the disorder in the systems and the constraints imposed on the Hessian matrices due to structural considerations.

In chapter four, we have calculate the LNV in eigenvalue regions near the ME for several system sizes. On the energy scales large compared to the mean level spacing, the level compressibility characterize the critical behavior at the LDT. Quantitatively, the LCP should be lower than $\chi \approx 0.35 \pm 0.08$ in our calculation. Suffering from not enough levels in selected regimes and mixing of eigenvalues range, it is difficult to determine the LCP and verify the scaling relation of Eq.(4.4) by our model. On the other hand, the FSS gives results with larger errors for the position of MEs and the correlation length exponents $\nu_p = 1.43 \pm 0.21$ and $\nu_n = 1.48 \pm 0.17$, which generally agree with the previous results.

In chapter five, we have performd the multifractal analysis at the ME in the both positve and negative branch of INM spectrum. A set of general dimensions charaterizes the strong fluctuations of the amplitude of the critical INMs, and at the ME the general dimensions for both branches are consisted. By means of box-size scaling and based on the Legendre transform of the mass exponent, we have calculated the singularity spectrum (SSP), which shows an excellent agreement with the most accuracy results of the AM so far. We confirm that the SSP is a universal quantity. According to the invariance of the SSP with respect to system size, the location of the ME with the value $\lambda = -86.6 \pm 0.5$ is determined in the negative branch, which agrees with the LS analysis. Furthermore, based on the probability-density-function analysis, the SSP at the ME is verified again. The symmetry relation of the multifractal INMs is verified, for the small q region, the symmetric relation is satisfied, however, deviates strongly for $|q - 0.5| > 1$. The larger the system size, the better the symmetric relation holds. Moreover, the correlation function of the q-moments of components of INMs is also calculated. The power-law decay of the correlation function is verified to connect with the mass exponents. Finally, we present

the distribution of the inverse participation ratio, which has the same nature with the AM.

Appendix A

Appendix

A.1 Renormalization Group and Finite-Size Scaling

To study the critical phenomena, one of the powerful tools is *the renormalization group(RG)* analysis. One can extract various exponents from RG analysis. With the information, it is relatively easy to pin down *the critical point* and thus *the type of phase transition*.

Instead of direct performing RG caluculation, we do *the finite-size scaling* which has been extensively used to solve the problem of critical phenomena [52][53]. Strictly speaking, there are no phase transitions in a finite system. How to exhibit a phase transition in a finite system? The answer forms the topic of finite-size scaling. Although the first hypothesis was proposed before the RG, finite size scaling is conceptually clearer within the framework of the RG. Summarizing from Nigel Goldenfeld's excellent introducton book[11], we brief illustrate three topics: first, *what is the RG transformation? second, how RG accounts for scaling behavior and the critical exponent*, finally, derive *the formula of the finite-size scaling from RG*.

First, consider a system with N particles, linear dimension L and volume $V = L^d$. The free energy density is a function of temperature t, external field h and interaction or coupling constant K. After the coarse-grain process that particles within a small box with length $l > 1$ coarse grain to one new particle, the arguments of the function

change and the free energy density scales with

$$Nf_s(t, h, K...) = Nl^{-d}f_s(t_l, h_l, K_l...). \tag{A.1}$$

The coarse-grain process also denotes as *the RG transformation R_l*, which describes how the coupling constants and external field change with the length scale, and over which the local operators of R_l are defined as

$$[t_l] = R_l[t], \quad [h_l] = R_l[h] \quad \text{and} \quad [K_l] = R_l[K].$$

The R_l is a very complicated, non-linear transformation, and at the fixed point K^* the RG transformation satisfies $[K^*] = R_l[K^*]$. Succesive transformations with $l = l_1$ and $l = l_2$ should be equivalent to a combined scale change of $l_1 l_2$:

$$\begin{aligned} [K'] &= R_{l_1}[K] \\ [K''] &= R_{l_2}[K'] \\ &= R_{l_2} \cdot R_{l_1}[K] \end{aligned}$$

and thus

$$R_{l_1 l_2}[K] = R_{l_2} \cdot R_{l_1}[K] \tag{A.2}$$

Second, we illustrate how RG quantitatively accounts for scaling behavior. Suppose only one coupling constant K in the vicinity of the fixed point K^*, we have

$$\begin{aligned} K' - K^* &= R_l(K) - R_l(K^*) \\ &\simeq \Lambda_l(K - K^*) + O((K - K^*)^2) \end{aligned}$$

where

$$\Lambda_l \equiv \left. \frac{\partial R_l}{\partial K} \right|_{K=K^*} \tag{A.3}$$

is **the linearised RG transformation** in the vicinity of the fixed point. Because the RG transformation satisfies Eq.(A.2),

$$\Lambda_l \Lambda_{l'} = \Lambda_{ll'}.$$

The only solution of Λ_l should be

$$\Lambda_l = l^{y_k}. \tag{A.4}$$

78

With the RG transform, we can make contact with the critical exponents quantitatively. Consider a simple system with only one coupling constant, the temperature T. Under an RG transformation, T is transformed to $T' = R_l(T)$. At a fixed point, $T^* = R_l(T^*)$. Linearising in the vicinity of the fixed point, we have

$$
\begin{aligned}
T' - T^* &= R_l(T) - R_l(T^*) \\
&\simeq \Lambda_l(T - T^*) + O((T - T^*)^2)
\end{aligned}
\tag{A.5}
$$

where

$$
\Lambda_l \equiv \left. \frac{\partial R_l}{\partial T} \right|_{T=T^*}.
\tag{A.6}
$$

As argued before, we have $\Lambda_l = l^{y_t}$. Consider the case where the system is originally at a temperature above the critical temperature. Defining $t = (T - T^*)/T^*$, the recursion relation Eq.(A.5) becomes

$$
t' = t l^{y_t}.
\tag{A.7}
$$

The correlation length under one RG transformation is $\xi' = \xi/l$, and thus, after n transformations

$$
\xi(t) = l^n \xi(t l^{n y_t}).
$$

We can arbitrary choose

$$
l^n = \left(\frac{b}{t} \right)^{1/y_t},
$$

with b being some arbitrary positive number much larger than unity. Thus

$$
\xi(t) = (b^{-1} t)^{-1/y_t} \xi(b) \quad \text{as } t \to 0.
\tag{A.8}
$$

Note that $\xi(b)$ is the correlation length for temperatures well above T_c, where fluctuations are small, and standard approximation methods, such as perturbation theory work well. Comparing Eq.(A.8) with the definition of the critical exponent $\nu : \xi \sim t^{-\nu}$, we read off

$$
\nu = \frac{1}{y_t}.
$$

The exponent y_t is simply given by Eq.(A.4) and Eq.(A.6)

$$
y_t = \frac{\ln \Lambda_l}{\ln l} = \frac{1}{\ln l} \ln \left[\frac{\partial R_l}{\partial T} |_{T=T^*} \right]
\tag{A.9}
$$

79

Thus, knowlege of R_l, or a good approximation to it, enables us to calculate Λ_l, y_t and hence ν. In the language of RG, the positive y value corresponds to the *relevant scaling variable*, while negative one corresponds to the *irrelevant scaling variable* which can be ignored for large enough L.

Finally, to derive the finite-size scaling formula, the free energy density close to a fixed point of RG is writen as

$$f_s(t, h, K, ..., L^{-1}) = l^{-d} f_s(tl^{y_t}, hl^{y_h}, Kl^{y_K}, ..., lL^{-1}). \tag{A.10}$$

Here comes a new argument the inverse size of the system, L^{-1}, and the lL^{-1} on the right hand side of Eq.(A.10) comes from the fact that lengths are reduced by a factor l during a RG transformation R_l. The RG transformation is a local transformation, and, therefore, it does not matter if it is performed on an infinite system or a finite system. We see that L^{-1} behaves like a relevant eigenvector with eigenvalue $\Lambda_L = l$, and thus $y_L = 1$. A corollary is that crossover effects become important for finite L. Suppose all parameters set to be zero except t, choose $l = |t|^{-1/y_t}$ the singular part of the free energy density is

$$
\begin{aligned}
f_s(t, L^{-1}) &= |t|^{d/y_t} f_s(1, |t|^{-1/y_t} L^{-1}) \\
&= |t|^{d\nu} F_f^{\pm}(|t|^{-\nu} L^{-1}).
\end{aligned}
$$

For the bulk correlation length of the infinite system with $L = \infty$, which we denote now by $\xi_\infty(t) = |t|^{-\nu}$, therefore

$$f_s(t, L^{-1}) = |t|^{d\nu} F_f^{\pm}(\xi_\infty(t)L^{-1}).$$

When $|t|^{-\nu} L^{-1} << 1$, or equivalently $L >> \xi_\infty(t)$, the correlation length is not affected by the boundaries of the sytem, and the thermodynamic properties are those of the infinite system. In the opposite limit, encountered sufficiently close to $t = 0$, $L << \xi_\infty(t)$, or equivalently $|t|^{-\nu} L^{-1} >> 1$, and the system is no longer governed by the critical fixed point. In this case, the actual correlation length can not grow beyond L as $t \rightarrow 0$, and the transition appears rounded. We can exploit these phenomena in practice to obtain estimates of the true critical behavior. As an example, consider

the scaling of the correlation length itself,

$$
\begin{aligned}
\xi(t, L^{-1}) &= l\xi(tl^{y_t}, lL^{-1}) \\
&= t^{-\nu} F_\xi(L^{-1}t^{-\nu}) \\
&= t^{-\nu}(Lt^\nu)\widetilde{F}(Lt^\nu) \\
&= L\widetilde{F}(Lt^\nu) \quad\quad\quad\quad\quad (A.11)
\end{aligned}
$$

In Eq.(A.11), we have defined a new scaling function $\widetilde{F}(x)$, which must have the following limiting behavior. For $L \to \infty$ at fixed $t << 1$, we expect $\xi(t, 0) \sim t^{-\nu}$. Thus $\widetilde{F}(x) \to x^{-1}$ as $x \to \infty$. For L finite and $t \to 0$, $\widetilde{F}(x)$ tends towars a constant. It is perfectly analytic in this limit and $\xi \sim L$. Thus, at finite L we can expand about $t = 0$:

$$
\frac{L}{\xi(t, L^{-1})} = A + BtL^{1/\nu} + O(t^2), \quad\quad\quad\quad\quad (A.12)
$$

where A and B are constants. The beauty of this form is that if we plot L/ξ versus the coupling constant, K or t, for different values of L, all curves will pass through the same point when $K = K^*$ or $t = 0$. Thus we can determine K^*.

A.2 Derivation for Legendre Transform of SSP from The Mass Exponents

Generally, *the general inverse participation ratio* scales with system size as

$$
P_q(\eta) \sim \eta^{\tau_q}, \quad\quad\quad\quad\quad (A.13)
$$

where τ_q is the mass exponent. Here, we derive the Legendre transform $\tau_q = \alpha q - f(\alpha)$.

Consider the LPD μ_k defined in Eq.(5.5), in the discrete system satisfies the normalized condition $\sum_{k=1}^{N_\eta} \mu_k = 1$, where $N_\eta = \left(\frac{L}{l}\right)^3 = \eta^{-3}$. The probability density function of the LPD $\widetilde{p}_L(\mu)$ is defined such that

$$
\widetilde{p}_L(\mu)d\mu = \frac{\Delta N_\mu}{N_\eta},
$$

where ΔN_μ is the number of boxes with μ_k within $[\mu, \mu + d\mu]$. The $\widetilde{p}_L(\mu)$ is normalized as,

$$\int \widetilde{p}_L(\mu) d\mu = 1.$$

By changing variable to the singularity strength

$$\alpha = \ln \mu / \ln \eta,$$

the corresponding PDF $P_L(\alpha)$ is given as $\widetilde{p}_L(\mu) d\mu / d\alpha$. The PDF of α should also satisfy the nomalization condition

$$\int P_L(\alpha) d\alpha = \int \widetilde{p}_L(\mu) d\mu = 1.$$

After changing variable to the singularity strength, the definition of the gIPR become

$$P_q(\eta) = \sum_{k=1}^{N_\eta} (\mu_k)^q = N_\eta \int \widetilde{p}_L(\mu) \cdot \mu^q \cdot d\mu$$
$$= N_\eta \int P_L(\alpha) \cdot \eta^{\alpha q} \cdot d\alpha$$

Based on the definition of fractal dimension $\Delta N_\alpha \sim \eta^{-f(\alpha)}$, where ΔN_α is the number of boxes belong to $[\alpha, \alpha + d\alpha]$, and the probability of α within $[\alpha, \alpha + d\alpha]$ is $P_L(\alpha) d\alpha = \Delta N_\alpha / N_\eta$. Therefore, we have

$$N_\eta \cdot P_L(\alpha) \cdot d\alpha \sim \eta^{-f(\alpha)}.$$

Consequently,

$$P_q(\eta) \sim \int \eta^{[\alpha q - f(\alpha)]} \cdot d\alpha \qquad (A.14)$$

Evaluation of the integral by the saddle-point method gives

$$P_q(\eta) \sim \eta^{\alpha q - f(\alpha)} \qquad (A.15)$$

which reproduce Eq.(A.13), with the mass exponent τ_q relate to the singularity spectrum via the Legendre transform

$$\tau_q = \alpha q - f(\alpha),$$
$$\alpha_q = \frac{d\tau_q}{dq}, \text{ and } q = \frac{df(\alpha)}{d\alpha}.$$

82

A.3 The Relation between The Correlation Exponents and The Mass Exponents

The spatial correlation function for the q-th moment of the squared vibrational amplitudes in the INMs in a system of size L as

$$C_q(r, L) = \left\langle \frac{1}{N\Delta N_r} \sum_{i=1}^{N} \sum_{j=1}^{\Delta N_r} |\psi_i|^{2q} |\psi_j|^{2q} \right\rangle_\lambda . \qquad (A.16)$$

In a general version, as a coarse-grain form $C_q'(l, r, L)$ is the spatial correlation function of boxes

$$C_q'(l, r, L) = \left\langle \frac{1}{N_\eta \Delta N_{\eta r}} \sum_{k=1}^{N_\eta} \sum_{kr=1}^{\Delta N_{\eta r}} \mu_k^q \mu_{kr}^q \right\rangle_\lambda ,$$

where μ_k is the LPD in the k-th box with length l, N_η and $\Delta N_{\eta r}$ are the number of boxes, k and kr are index of box and another box with a distance r away from k, respectively. As $l = 1$, $C_q'(l, r, L) \rightarrow C_q(r, L)$. Due to the absence of characteristic lengths in the multifractal system, $C_q'(l, r, L)$ should behave as

$$C_q'(l, r, L) \propto l^{x_q} \cdot L^{-y_q} \cdot r^{-z_q}. \qquad (A.17)$$

Our task is to relate the new exponent x_q, y_q and z_q to previously introduced exponents τ_q.

Suppose $r = l$ and l is small, because that the correlation is strong , we could assume $\mu_k^q \sim \mu_{kr}^q$. In this case, the Eq.(5.22) with $N_\eta = (\frac{L}{l})^d$ and $\Delta N_{\eta r} \sim 1$ and Eq.(5.7) give

$$C_q'(l, r = l, L) \sim \left\langle (\frac{l}{L})^d \sum_k \mu_k^{q+q} \right\rangle \sim (\frac{l}{L})^{d+\tau_{2q}},$$

where d is the spatial dimension. Since we have $C_q'(l, r = l, L) \propto l^{x_q - z_q} \cdot L^{-y_q}$ from Eq.(A.17), the exponents are related by

$$y_q = d + \tau_{2q},$$

and

$$x_q - z_q = d + \tau_{2q}. \qquad (A.18)$$

In order to determine the exponent x_q, we consider $r = L$, where $\Delta N_{\eta r} \sim \left(\frac{L}{l}\right)^d$. Since the measurements are almost uncorrelate in this region, we could assume

$$\left\langle \sum_k \sum_{kr} \mu_k^q \cdot \mu_{kr}^q \right\rangle \sim \left\langle \sum_k \mu_k^q \right\rangle \cdot \left\langle \sum_{kr} \mu_{kr}^q \right\rangle.$$

Therefore, in this case Eq.(5.22) becomes

$$C_q'(l, r = L, L) \sim (\frac{l}{L})^{2d} \left\langle \sum_k \mu_k^q \right\rangle \cdot \left\langle \sum_{kr} \mu_{kr}^q \right\rangle \sim (\frac{l}{L})^{2d + \tau_q + \tau_q}.$$

Since we have

$$C_q'(l, r = L, L) \propto l^{x_q} \cdot L^{-y_q - z_q}$$

from Eq.(A.17), the exponents are relate by

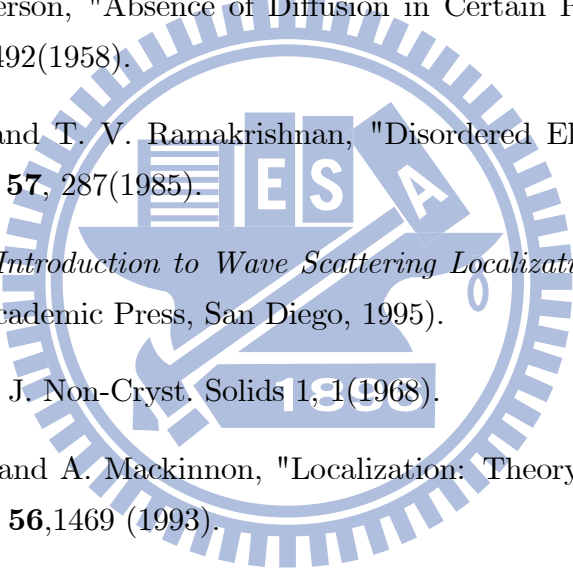$$\begin{aligned} x_q &= 2d + 2\tau_q, \\ y_q + z_q &= 2d + 2\tau_q. \end{aligned}$$

By Eq.(A.18),

$$z_q = d + 2\tau_q - \tau_{2q}. \tag{A.19}$$

Therefore, as $l = 1$

$$C_q'(l, r, L) \sim C_q(r, L) \sim L^{-y_q} \cdot r^{-z_q}.$$

with y_q and z_q given in (A.18) and (A.19). The three new exponents x_q, y_q and z_q characterize the scaling with box-size, system size and the correlation distance between measurements.

Bibliography

[1] S. R. Elliott, *Physics of Amorphous Materials.* (Longman, London, 1990).

[2] P. W. Anderson, "Absence of Diffusion in Certain Random Lattices", Phys. Rev. **109**,1492(1958).

[3] P. A. Lee and T. V. Ramakrishnan, "Disordered Electronic Systems", Rev. Mod. Phys. **57**, 287(1985).

[4] P. Sheng , *Introduction to Wave Scattering Localization and Mesoscopic Phenomena* (Academic Press, San Diego, 1995).

[5] N. F. Mott, J. Non-Cryst. Solids 1, 1(1968).

[6] B. Kramer and A. Mackinnon, "Localization: Theory and Experiment", Pep. Prog. Phys. **56**,1469 (1993).

[7] N. F. Mott, *Conduction in Non-Crystalline Materials.* (Clarendon press, Oxford, 1993).

[8] E. Abrahams, P.W. Anderson, D.C. Licciardello, T.V. Ramakrishnan, "Scaling Theory of Localization: Absence of Quantum Diffusion in Two Dimensions", Phys. Rev. Lett. **42**, 673(1979).

[9] H. E. Stanley, *Introduction to Phase Transitions and Critical Phenomena.* (Oxford University Press, New York, 1971).

[10] John Cardy, *Scaling and Renormalization in Statistical Physics.* (Cambridge University Press, Cambridge, 1996).

[11] N. Goldenfeld, *Lectures on Phase Transitions and The Renormalization Group.* (Addison-Wesley, Taipei, 1991).

[12] M. L. Mehta, *Random Matrices.* (Academic Press, San Diego, 1991).

[13] F. Evers and A. D. Mirlin, "Anderson Transitions", Rev. Mod. Phys. **80**,1355(2008).

[14] T. Guhr, A. Műller-Groeling, H. A. Weidenműller, "Random-Matrix Theories in Quantum Physics: Common Concepts", Phys. Rep. **299**, 189(1998).

[15] I. K. Zharekeshev and B. Kramer, "Asymptotics of Universal Probability of Neighboring Level Spacings at the Anderson Transition", Phys. Rev. Lett. **79**, 717 (1997).

[16] F. Milde, R. A. Römer, and M. Schreiber, "Energy-Level Statistics at the Metal-Insulator Transition in Anisotropic Systems", Phys. Rev. B. **61**, 6028 (2000).

[17] K. Slevin and T. Ohtsuki, "Corrections to Scaling at the Anderson Transition", Phys. Rev. Lett. **82**, 382 (1999).

[18] R. M. Stratt and B.C. Xu, "Band Structure in a Liquid", Phys. Rev. Lett. **62**.1675(1989).

[19] G. Seeley and T. Keyes, "Normal-Mode Analysis of Liquid-State Dynamics", J. Chem. Phys. **91**, 5581(1989).

[20] T. M. Wu and R. F. Loring, "Phonons in liquids: A random walk approach", J. Chem. Phys. **97**, 8568(1992).

[21] Yi Wan and R. M. Stratt, "Liquid Theory for the Instantaneous Normal Modes of a Liquid", J. Chem. Phys. **100**,5123(1994).

[22] T. Keyes, "Instantaneous Normal Mode theory of Quantum Time Correlation Functions: Raman Spectrum of Liquid CS_2", J. Chem. Phys. **106**, 46(1997).

[23] P. K .Mankoo and T. Keyes, "POLIR: Polarizable, Flexible, Transferable Water Potential Optimaized for IR Spectroscopy", J. Chem. Phys. **129**, 034504(2008).

[24] P. G. Debenedetti and F. H. Stillinger, "Supercooled Liquids and the Glass transition", Nature **410**, 259(2001).

[25] S. Ciliberti, P. Rios and F. Piazza, "Glasslike Structure of Globular Proteins and the Boson Peak", Phys. Rev. Lett **96**, 198103(2006).

[26] S. D. Bembenek and Brian B. Laird, "The Role of Localization in Glasses and Supercooled Liquids", J. Chem. Phys. **104**, 5199(1996).

[27] S. D. Bembenek and Brian B. Laird, "Instantaneous Normal Modes and the Glass transition", Phys. Rev. Lett **74**, 936(1995).

[28] R. C. Zeller and R. O. Pohl, "Thermal Conductivity and Specific Heat of Non-crystalline Solids", Phys. Rev. B **4**, 2029(1971).

[29] A. Jagannathan, R. Orbach and O. Entin-Wohlman, "Thermal Conductivity of Amorphous Materials above the Plateau", Phys. Rev. B. **39**, 13465(1989).

[30] B. B. Nandelbrot: J. Fluid Mech. **62**,331(1974).

[31] T. Nakayama and K. Yakubo, *Fractal Concepts in Condensed Matter Physics.* (Springer, Heidelberg, 2003).

[32] P. Grassberger, "On the Fractal Dimension of the Henon Attractor", Phys. Lett. **97A**, 224(1983).

[33] P. Grassberger and I. Procaccia, "Measuring the Strangeness of Strange Attractors", Physica **9D**, 189(1983).

[34] R. Benzi, G. Paladin, G. Parisi and A. Vulpiani, "On the Multifractal Nature of Fully Developed Turbulence and Chaotic Systems", J. Phys. A **17**, 3521(1984).

[35] J. F. Muzy, E. Bacry and A. Arneodo, "Wavelets and Multifractal Formalism for Singular Signals: Application to Turbulence Data", Phys. Rev. Lett. **67**, 3515(1991).

[36] T.C. Halsey, P. Meakin and I. Procaccia, "Scaling Structure of the Surface Layer of Diffusion-Limited Aggregates", Phys. Rev. Lett. **56**, 854(1986).

[37] C. Amitrano, A. Coniglio and F. di Liberto, "Growth Probability Distribution in Kinetic Aggregation Processes", Phys. Rev. Lett. **57**, 1016(1986).

[38] T. C. Halsey, M. H. Jensen, L. P. Kadanoff, I. Procaccia, and B. I. Shraiman, "Fractal Measures and Their Singularities: The Characterization of Strange Sets", Phys. Rev. A **33**, 1141(1986).

[39] P. Meakin, A. Coniglio, and H. E. Stanley, "Scaling Properties for the Surfaces of Fractal and Nonfractal Objects: An Infinite Hierarchy of Critical Exponents", Phys. Rev. A **34**, 3325(1986).

[40] H. E. Stanley and P. Meakin, "Multifractal Phenomena in Physics and Chemistry", Nature **335**, 405(1988).

[41] P. Ch. Ivanov et. al. , "Multifractality in Human Heartbeat Dynamics", Nature **399**, 461(1999).

[42] H. Grussbach and M. Schreiber, "Determination of the Mobility Edge in the Anderson Model of Localization in Three Dimensions by Multifractal Analysis", Phys. Rev. B **51**, 663(1995).

[43] N. G. Van Kampen, *Stochastic Processes in Physics and Chemistry*, chapter 2, Elsevier. (978-0-444-52965-7).(2007).

[44] O. C. lbe, *Markov Processes for Stochastic Modeling*, chapter 1, Elsevier Academic Press (978-0-12-374451-7).

[45] W. J. Ma, T. M. Wu, and J. Hsieh, "Conservation Constraints on Random Matrices", J. Phys. A **36**, 1451(2003).

[46] D. A. Parshin and H. R. Schober, "Multifractal Structure of Eigenstates in the Anderson Model with Long-Range Off-Diagonal Disorder", Phys. Rev. B **57**, 10232(1998).

[47] W. H. Press, B. P. Flannery, S. A. Teukolsky, and W. T. Vetterling, *Numerical Recipes in C++* (Cambridge University Press, Cambridge, 2002).

[48] M. Mězard, G. Parisi, and A. Zee, "Spectra of Euclidean Random Matrices", Nucl. Phys. B **559**, 689(1999).

[49] S. N. Taraskin, Y. L. Loh, G. Natarajan, and S. R. Elliot, "Origin of the Boson Peak in Systems with Lattice Disorder", Phys. Rev. Lett. **86**, 1255(2001).

[50] J. J. Ludlam, S. N. Taraskin, and S. R. Elliot, "Disorder-Induced Vibrational Localization", Phys. Rev. B **67**, 132203(2003).

[51] W. Schirmacher, G. Diezemann and C. Ganter, "Harmonic Vibrational Excitations in Disordered Solids and the Boson Peak", Phys. Rev. Lett. **81**, 136(1998).

[52] J. L. Cardy ed, *Reprint volume: Finite-Size Scaling* (Elsevier Science Publishers, Amsterdam, 1988).

[53] V. Privman ed, *Finite Size Scaling and Numerical Simulation of Statistical Systems* (World Scientific Press, Singapore, 1990).

[54] E. La Nave, A. Scala, F. W. Starr, H. E. Stanley, and F. Sciortino, "Dynamics of Supercooled Water in Configuration Space", Phys.Rev. E **64**, 036102(2001).

[55] T. M. Wu, S. L. Chang, and K. H. Tsai, "Mechanism for Singular Behavior in Vibrational Spectra of Topologically Disordered Systems: Short-Range Attractions", J. Chem. Phys. **122**, 204501(2005).

[56] S. N. Taraskin and S. R. Elliott, "Vector vibrations and the Ioffe-Regel Crossover in Disordered Lattices", J. Phys. : Condens. Matter **14**, 3143(2002).

[57] B. Kramer, T. Ohtsuki, and S. Kettemann, "Random Network Models and Quantum Phase Transitions in Two Dimensions", Phys. Rep. **417**, 211 (2005) and reference therein.

[58] F. J. Dyson, J. Math. Phys. **3**, 140 (1962).

[59] B. L. Altshuler, I. Kh. Zharekeshev, S. A. Kotochigova, and B. I. Shklovskii, "Repulsion Between Energy Levels and the Metal-Insulator Transition", Sov. Phys. JETP **67**, 625(1988).

[60] I. Kh. Zharekeshev and B. Kramer, "Universal Fluctuations in Spectra of Disordered Systems at the Anderson Transition", Jpn. J. Appl. Phys. **34**, 4361(1995).

[61] D. Braun, G. Montambaux, and M. Pascaud, "Boundary Conditions at the Mobility Edge", Phys. Rev. Lett. **81**,1062(1998).

[62] B. I. Sklovskii, B. Shapiro, B. R. Sears, P. Lambrianides, and H. B. Shore, "Statistics of Spectra of Disordered Systems Near the Metal-Insulator Transition", Phys. Rev. B **47**, 11487(1993).

[63] A. G. Aronov, V. E. Kravtsov, and I. V. Lerner, "Level Spacing Distribution near the Anderson Transition", JETP Lett. **59**, 39(1994).

[64] Antonio M. Garcia-Garcia and Emilio Cuevas, "Dimensional Dependence of the Metal-Insulator Transition", Phys. Rev. B **75**, 174203(2007).

[65] J. Chalker, V. Kravtsov, I. Lerner, "Spectral Rigidity and Eigenfunction Correlations at the Anderson Transition", Sov. Phys. JETP Lett. **64**, 386(1996).

[66] R. M. Stratt, "The Instantaneous Normal Modes of Liquids", Acc. Chem. Res. **28**, 201 (1995).

[67] M.L. Ndawana, R.A. Römer, and M. Schreiber, "Finite-Size Scaling of the Level Compressibility at the Anderson transition", Eur. Phys. J. B **27**, 399(2002).

[68] C. M. Soukoulis and E. N. Economou, "Fractal Character of Eigenstates in Disordered Systems", Phys. Rev. Lett. **52**, 565 (1984).

[69] M. Schreiber and H. Grussbach, "Multifractal Wave Functions at the Anderson Transition", Phys. Rev. Lett. **67**,607 (1991).

[70] Takamichi Terao, "Multifractal Wave Functions in Three-Dimensional Systems withou Time-Reversal Symmetry", Phys. Rev. B **56**, 975(1997).

[71] D. A. Parshin and H. R. Schober, "Distribution of Fractal Dimensions at the Anderson Transition", Phys. Rev. Lett. **83**, 4590(1999).

[72] P. Grassberger and I. Procaccia, "Characterizeation of Strange Attractors", Phys. Rev. Lett. **50**, 346(1983).

[73] A. Mildenberger, F. Evers, and A. D. Mirlin, "Dimensionality Dependence of the Wave-Functions Statistics at the Anderson Transition", Phys. Rev. B **66**, 033109(2002).

[74] E. Cuevas, M. Ortuno, V. Gasparian, and A. Perez-Garrido, "Fluctuations of the Correlation Dimension at Metal-Insulator Transitions", Phys. Rev. Lett. **88**, 016401(2002).

[75] F. Evers and A. D. Mirlin, "Fluctuations of the Inverse Participation Ratio at the Anderson Transition", Phys. Rev. Lett **84**, 3690(2000).

[76] A. D. Mirlin, Y. V. Fyodorov, A. Mildenberger, and F. Evers, "Exact Relations between Multifractal Exponents at the Anderson Transition", Phys. Rev. Lett. **97**, 046803(2006).

[77] A. Mildenberger and F. Evers, "Wave Function Statistics at the Symplectic Two-Dimensional Anderson Transition: Bulk Properties", Phys. Rev. B **75**, 041303 (2007).

[78] Alexander D. Mirlin, "Statistics of Energy Levels and Eigenfunctions in Disordered Systems", Phys. Rep. **326**, 259(2000).

[79] B. J. Huang and T. M. Wu, "Localization-Delocalization Transition in Hessian Matrices of Topologically Disordered Systems", Phys. Rev. E **79**, 041105(2009).

[80] B. J. Huang and T. M. Wu, "Numerical Studies for the Localization-Delocalization Transition in Vibrational Spectra: Level-Spacing Statistics and Multifractal Analysis", submitted to Comput. Phys. Commun. (Accepted).

[81] M. Bollhöfer and Y. Notay, "JADAMILU: A Software Code for Computing Selected Eigenvalues of Large Sparse Symmetric Matrices", Comput. Phys. Commun. **177**, 951(2007).

[82] J. K. Cullum and R. A Willoughby, *Lanczos Algorithms for Large Symmetric Eigenvalue Computations* (Birkhauser, Boston,1985).

[83] M. Bollhöfer and Y. Notay, JADAMILU. http://homepages.ulb.ac.be/~jadamilu/

[84] M. P. Allen and D. J. Tildesley, *Computer Simulation of Liquids* (Clarendon Press, Oxford, 1987).

[85] O. Schenk, M. Bollhöfer, and R. Römer, SIAM J. Sci. Comput. USA **28**, 963 (2006) .

[86] L. J. Vasquez, A. Rodriquez, and R. Römer, "Multifractal Analysis of the Metal-Insulator Transition in the Three-Dimensional Anderson model. I. Symmetry Relation under Typical Averaging.", Phys. Rev. B **78**,195106(2008).

[87] L. J. Vasquez, A. Rodriquez, and R. Römer, "Multifractal Analysis of the Metal-Insulator Transition in the Three-Dimensional Anderson Model. II. Symmetry Relation under Ensemble Averaging."Phys. Rev. B **78**,195107(2008).

[88] I. V. Plyushchay, R. A. Römer, and M. Schreiber, "Three-Dimensional Anderson Model of Localization with Binary Random Potential", Phys. Rev. B **68**, 064201(2003).

[89] A. Eilmes, A. M. Fischer, and R. A. Römer, "Critical Parameters for the Disorder-Induced Metal-Insulator Transition in FCC and BCC Lattices", Phys. Rev. B **77**, 245117(2008).

[90] V. Dobrosavljević, A. A. Pastor and B. K. Nikolić, "Typical Medium Theory of Anderson Localization: A Local Order Parameter Approach to Strong-Disorder Effects", Europhys. Lett, **62**(1), 76(2003).

[91] J. J. Ludlam, *Localisatin of the Vibraions of Amorphous Materials*, P.h. D thesis, Trinity College, Cambridge, UK.

[92] F. J. Wegner, Nucl. Phys. B **316**, 663(1989).

[93] X. Jia, A. R. Subramaniam, I. A. Gruzberg, and S. Chakravarty, "Entanglement Entropy and Multifractality at Localization Transitions", Phys. Rev. B **77**, 014208(2008).

[94] L. Gong and P. Tong, "Localization-Delocalization Transitions in a Two-Dimensional Quantum Percolation Model: Von Neumann Entropy Studies", Phys. Rev. B **80**, 174205(2009).

[95] J. J. Ludlam, S. N. Taraskin, and S. R. Elliott, "Disorder-Induced Vibrational Localization", Phys. Rev. B **67**,132203(2003).

[96] F. Milde, R. A. Römer, and M. Schreiber, "Multifractal Analysis of the Metal-Insulator Transition in Anisotropic Systems", Phys. Rev. B **55**, 9463 (1997).

[97] A. Rodriguez, L. J. Vasquez, and R. A. Römer, "Multifractal Analysis with the Probability Density Function at the Three-Dimensional Anderson Transition", Phys. Rev. Lett. **102**, 106406(2009).

[98] S. Faez, A. Strybulevych, J. H. Page, A. Lagendijk, and B. van Tiggelen, "Observation of Multifractality in Anderson Localization of Ultrasound", Phys. Rev. Lett. **103**, 155703 (2009).

[99] K. Pracz, M. Janssen, and P. Freche, "Correlation of Eigenstates in the Critical Regime of Quantum Hall Systems", J. Phys. : Condens. Matter 8, 7147 (1996).

[100] H. Obuse and K. Yakubo, "Correlation Exponent and Anomalously Localized States at the Critical Point of the Anderson Transition", J. Phys. Soc. Jpn. 73, 2164 (2004).